REPORT DOCUMENTATION PAGE

Form Approved
OMB No. 0704-0188

1. REPORT DATE (DD-MM-YYYY)	2. REPORT TYPE	3. DATES COVERED (From - To)
12-26-2004	Final Technical Report	November 2001 - May 2004

4. TITLE AND SUBTITLE

Multifunctional Carbon Nanotube Fiber Composites

5a. CONTRACT NUMBER

MDA972-02-C-0005

5b. GRANT NUMBER

N/A

5c. PROGRAM ELEMENT NUMBER

N/A

6. AUTHOR(S)

Baughman, Ray, H.; Collins, Steve; Wallace, Gordon G.; Barisci, Joseph, N.; Kozlov, Mikhail; Gartstein, Yuri; Rinzler, Alan, G; Zakhidov, Anvar, A.; Raj, Rishi; Kertesz, Miklos; Dalton, Alan, B.; Too, Chee; Munoz, Edgar; Spinks, Geoffrey, M.; Roth, Siegmar; Vardeny, Zeev., V.; DeRossi, Danillo; Mazzoldi, Alberto; Morris, Robert C.

5d. PROJECT NUMBER

N/A

5e. TASK NUMBER

N/A

5f. WORK UNIT NUMBER

N/A

7. PERFORMING ORGANIZATION NAME(S) AND ADDRESS(ES)

University of Texas at Dallas, Richardson, TX 75080
University of Utah, Salt Lake City, UT 84112
University of Colorado, Boulder, CO 80309
University of Florida, Gainesville, FL 32611

8. PERFORMING ORGANIZATION REPORT NUMBER

9. SPONSORING/MONITORING AGENCY NAME(S) AND ADDRESS(ES)

Defense Advanced Research Projects Agency/Defense Science Office
3701 North Fairfax Dr.
Arlington, VA 22203-1714

10. SPONSOR/MONITOR'S ACRONYM(S)

DARPA/DSO

11. SPONSOR/MONITOR'S REPORT NUMBER(S)

N/A

12. DISTRIBUTION/AVAILABILITY STATEMENT

DISTRIBUTION STATEMENT A
Approved for Public Release
Distribution Unlimited

13. SUPPLEMENTARY NOTES

Any opinions, findings and conclusions or recommendations expressed in this material are those of the author(s) and sho interpreted as representing the official policies, either expressly or implied, of the Defense Advanced Research Projects /

14. ABSTRACT

The project provides a spinning process that results in continuous nanotube composite fibers that are about an order of magnitude tougher than any fibers made by mankind or nature. We make two hundred-meter long reels of continuous nanotube-polymer composite fiber at 70X the prior-art rate and achieve fiber strengths higher than 1.8 GPa. Our drawn nanotube fibers match the energy absorption capability of spider silk up to the breaking strain of this silk (30%), and continue absorbing energy until they reach an energy-to-break of 570 J/g, as compared with 160 J/g for the spider silk and 50 J/g for Spectra fiber, 33 J/g for Kevlar fiber. The density-normalized fiber tensile strength is presently 2.2X that of high performance steel wire and the density-normalized Young's modulus of the nanotube fiber and steel wire are identical. We have fabricated these fibers into 100 micron diameter, high performance supercapacitors that are woven into textiles. Other major advances in nanotube spinning, actuation, energy storage, and thermal energy harvesting are described which are potentially important for synthetic multifunctional materials applications.

15. SUBJECT TERMS

multifunctional materials, carbon nanotube fibers, nanotube fiber spinning, energy harvesting, energy storage, electronic textiles, ionic liquids, artificial muscles, electromechanical actuation, charge injection, supercapacitors, toughness

16. SECURITY CLASSIFICATION OF:

a. REPORT	b. ABSTRACT	c. THIS PAGE

17. LIMITATION OF ABSTRACT

18. NUMBER OF PAGES

19a. NAME OF RESPONSIBLE PERSON

19b. TELEPHONE NUMBER (Include area code)

Standard Form 298 (Rev. 8/98)
Prescribed by ANSI Std. Z39.18

Final Technical Report

for the DARPA Program

on

MULTIFUNCTIONAL CARBON NANOTUBE FIBER COMPOSITES

Executive Summary

The major program success is one that we did not anticipate at program start – the development of a spinning process that results in continuous nanotube composite fibers that are about an order of magnitude tougher than any fibers made by mankind or nature. As a result of program funding, we can make two hundred-meter long reels of continuous nanotube-polymer composite fiber at 70X the prior-art rate and achieve fiber strengths higher than 1.8 GPa. Our drawn nanotube fibers match the energy absorption capability of the highest performance spider silk up to the breaking strain of this silk (30%), and continue absorbing energy until they reach an energy-to-break of 570 J/g, as compared with 160 J/g for the spider silk, 50 J/g for Spectra fiber, 33 J/g for Kevlar fiber, and 1.5 J/g for prior-art solution-spun nanotube fibers. The density-normalized tensile strength of our nanotube composite fiber is presently 2.2X that of high performance steel wire and the density-normalized Young's modulus of the nanotube fiber and steel wire are identical.

In addition to spinning super-tough nanotube fibers, we developed two other nanotube spinning processes. One process, which uses polyethylenimine as the coagulation polymer, provides nanotube fibers that are much 70X more highly electronically conductive (100 S/cm) than those spun using the polyvinyl alcohol coagulant. The second process (patent pending) is novel in that it directly results polymer-free nanotube fibers without using a super acid spinning solution. Using both of these new spinning technologies (for the polyethylenimine coagulant and the polymer-free coagulants) we have been able to spin hollow nanotube fibers. Our polymer-free spinning process works for single walled nanotubes, double walled nanotubes, one-to-three mixtures by weight of single and multiwalled nanotubes, and one-to-one mixtures by weight of single walled nanotubes and imogolite (a naturally occurring silicate nanofiber). It produces hollow fibers, folded ribbon fibers and solid fibers, meaning those without aggregated void space. After annealing, the fibers spun from SWNT exhibit relatively high electrical conductivities (~140 S/cm at room temperature) and high electrochemical capacitances (~100 F/g). To improve intra-fiber mechanical coupling, we infiltrated poly(vinyl alcohol) in the as-spun gel fibers. The density-normalized mechanical properties dramatically increased to a maximum achieved true tensile strength of 770 MPa/(g/cm^3), a Young's modulus of 8.9 GPa/(g/cm^3), a strain-to-failure of 30 %, and a fiber toughness of 137 J/g. While lower in strength and toughness than the record values achieved for nanotube fibers that we spun by the polyvinyl alcohol coagulant process, this toughness exceeds that of commercial fibers used for antiballistic protection and is close to the maximum toughness observed for spider silk.

Using a variety of different types of spun nanotube fibers, we have made 100 micron or smaller diameter nanotube fiber capacitors and have extensively characterized their performance for multifunctional applications. Our packaged solid-state fiber supercapacitor devices display specific capacitance values ranging from 6 F/g to 12 F/g and energy and power densities reaching 1.34 Wh/kg and 1.0 kW/kg, respectively. Though, the discharge rate needs improvement, the energy density of our 100 micron diameter supercapacitors based on water-containing electrolytes is within a factor of 2-3 of that for large aqueous electrolyte commercial supercapacitors. In order to illustrate a

multifunctional application (energy storing textile), we have woven our nanotube fiber supercapacitors into a conventional textile.

Our efforts to improving actuation for coagulation-spun fibers and to use this improved actuation for multifunctional structures have been frustrated by the high modulus-to-strength ratio of polymer-free yarns, which results in fiber brittleness. While we have been able to solve this problem, this was done after program end by using our new draw-twist spinning technology, which is applicable for both single walled and multi-walled nanotubes. Successes in the present program were to demonstrate an actuator strain rate of 20%/s, which exceeds our program end milestone of 5%/s.

Using Pt-containing nanotube sheets, we have demonstrated thermoelectrochemical energy harvesting cells providing a Short Circuit Current Density of 3800 A/kg and a Maximum Power Density of 83 W/kg for a temperature difference of 65 °C. This result, based on nanotube electrode content, far exceeds the program end milestone of 700 A/kg. Results exceeding this milestone were also obtained for Pt-free multi-walled carbon electrodes, where the maximum short circuit current (normalized to the weight of electrode) reached 1446 A/kg and power was 28 W/kg. These results are for the ferri-ferro cyanide redox couple, which does not have long term stability at high electrode temperatures. We have found redox mediators and associated electrolyte systems that have much higher stability than the ferri-ferro cyanide system, but none provide comparable power densities.

Our efforts for the DARPA Synthetic Multifunctional Materials program has resulted in one patent application and 37 publications (including three in *Science*, one in *Nature*, and one in *Nature Materials*).

3

REFEREED PUBLICATIONS AND PATENTS FOR THE *MULTIFUNCTIONAL CARBON NANOTUBE CHARGE-TRANSFER COMPLEXES* PROGRAM AND THE *MULTIFUNCTIONAL CARBON NANOTUBE FIBER COMPOSITES* PROGRAM

1. "Electrochemical Properties of Aligned Nanotube Arrays: Basis of New Electromechanical Actuators", M. Gao, L. Dai, R.H. Baughman, G.M. Spinks, G.G. Wallace, Proc. SPIE-Int. Soc. Opt. Eng., Issue 3987 (Electroactive Polymer Actuators and Devices), 18-24 (2000).

2. "Electrochemical Studies of Single-Wall Carbon Nanotubes in Aqueous Solutions", J.N. Barisi, G.G. Wallace, and R.H. Baughman, *J. Electroanalytical Chem.* **488**, 92-98 (2000).

3. "Electrochemical Quartz Crystal Microbalance Studies of Single-Wall Nanotubes in Aqueous and Non-Aqueous Solutions", J.N. Barisi, G.G. Wallace, and R.H. Baughman, *Electrochim. Acta* **46**, 509-517 (2000).

4. "Electrochemical Characterization of Single-Walled Carbon Nanotube Electrodes", J.N. Barisi, G.G. Wallace, and R.H. Baughman, *J. Electrochem. Soc.* **147**, 4580-4583 (2000).

5. "Putting a New Spin on Carbon Nanotubes", R.H. Baughman, *Science* **290**, 1310-1311 (2000).

6. " Raman Scattering Study of Electrochemically Doped Single Wall Nanotubes", C.P. An, Z.V. Vardeny, Z. Iqbal, G. Spinks, R.H. Baughman, A.A. Zakhidov, *Synthetic Metals* **116**, 411-414 (2001).

7. "Carbon Nanotube Actuators", G.M. Spinks, G.G. Wallace, R.H. Baughman, L. Dai, Chapter 8 in *Electroactive Polymer (EAP) Actuators as Artificial Muscles - Reality, Potential and Challenges*, edited by Joseph Bar-Cohen, SPIE Press (2001).

8. "Electrochemically Driven Actuators from Conducting Polymers, Hydrogels, and Carbon Nanotubes", G.M. Spinks, G.G. Wallace, T.W. Lewis, L.S. Fifield, L. Dai, R.H. Baughman, Proc. SPIE-Int. Soc. Opt. Eng. 4234 (Smart Materials), 223-231, (2001).

9. "Microfabricated Electroactive Carbon Nanotube Actuators", A. Ahluwalia, R.H. Baughman, D. De Rossi, A. Mazzoldi, M. Tesconi, A. Tognetti, G. Vozzi, Proc. SPIE-Int. Soc. Opt. Eng. 4329 (Electroactive Polymer Actuators and Devices), 209-215 (2001).

10. "Conducting Polymer, Carbon Nanotube, and Hybrid Actuator Materials",
G.M. Spinks, G.G. Wallace, C.D. Carter, D. Zhou, L.S. Fifield, C.R. Kincaid,
R.H. Baughman, Proceedings of SPIE-The International Society for Optical Engineering
4329 (Electroactive Polymer Actuators and Devices), 199-208 (2001).

11. "Towards the Demonstration of Actuator Properties of a Single Carbon Nanotube",
J. Fraysse, A.I. Minett, G. Gu, S. Roth, A.G. Rinzler, R.H. Baughman,
Current Applied Physics **1**, 407-411 (2001).

12. "Synthesis of SiC Nanowires from Sheets of Single Wall Carbon Nanotubes",
E. Muñoz, A.B. Dalton, S. Collins, A.A. Zakhidov, R.H. Baughman, W.L. Zhou, J. He,
C.J. O'Connor, B. McCarthy, W.J. Blau, *Chem. Phys. Lett.* **359**, 397-402 (2002).

13. "Charge-Induced Anisotropic Distortions of Semiconducting and Metallic
 Carbon Nanotubes", Yu.N. Gartstein, A.A. Zakhidov, R.H. Baughman,
Phys. Rev. Lett. **89**, 45503 (2002).

14. "Carbon Nanotubes – The Route Towards Applications", R.H. Baughman,
A.A. Zakhidov, and W.A. de Heer, *Science* **297**, 787-792 (2002).

15. ""Dimensional Changes as a Function of Charge Injection for *trans*-Polyacetylene: a
Density Functional Study", G. Sun, J. Kürti, M. Kertesz, R.H. Baughman,
J. Chem. Phys. **117**, 7691-7697 (2002).

16. "Dimensional Changes as a Function of Charge Injection in Single Walled Carbon
 Nanotubes, G. Sun, J. Kürti, M. Kertesz, R.H. Baughman,
J. Am. Chem. Soc. **124**, 15076-15080 (2002).

17. "Improving the Mechanical Properties of Single-Walled Carbon Nanotube Sheets
by Intercalation of Polymeric Adhesives", J. N. Coleman, W. J. Blau, A. B. Dalton,
E. Muñoz, S. Collins, B. G. Kim, J. Razal, M. Selvidge, G. Vieiro, R. H. Baughman,
Applied Physics Letters **82,** 1682-1684 (2003).

18. "Super Tough Carbon-Nanotube Fibres", A.B. Dalton, S. Collins, E. Muñoz,
J. M. Razal, V.H. Ebron, J.P. Ferraris, J.N. Coleman, B.G. Kim, and R.H. Baughman,
Nature **423**, 703 (2003).

19. "Muscles Made from Metals", R.H. Baughman, *Science* **300**, 268-269 (2003).

20. "V₂O₅ Nanotube Actuators", G. Gu, M. Schmid, P.-W. Chiu, A. Minett, J. Fraysse,
G.-T. Kim, S. Roth, M. Kozlov, E. Muñoz, and R. H. Baughman,
Nature Materials **2**, 316-319 (2003).

21. "Variations of the Geometries and Band Gaps of Single Walled Carbon Nanotubes
and the Effect of Charge Injection", G. Sun, J. Kurti, M. Kertesz, R.H. Baughman,
J. of Physical Chemistry B **107**, 6924-6931 (2003).

22. "Mechanical Properties of Hybrid Polymer Nanotube Systems", J.N. Coleman, M. Cadek, A.B. Dalton, E. Muñoz, J. Razal, R.H. Baughman, W.J. Blau, *Proceedings of SPIE-The International Society for Optical Engineering* **5118** (Nanotechnology), 271-279 (2003).

23. "Increased Actuation Rate of Electromechanical Carbon Nanotube Actuators Using Potential Pulses with Resistance Compensation", J. N. Barisci, G. M. Spinks, G. G. Wallace, J. D. Madden, R. H. Baughman, *Journal of Smart Materials and Structures*, **12**, 549-555 (2003).

24. "Electrochemical Properties of Single-Wall Carbon Nanotube Electrodes", J.N. Barisci, G.G. Wallace, D. Chattopadhyay, F. Papadimitrakopoulos, R.H. Baughman, *J. Electrochem.Soc.* **150**, E409-E415 (2003).

25. "Mechanical and Electromechanical Coupling in Carbon Nanotube Distortions", Yu.N. Gartstein, A.A. Zakhidov, and R.H. Baughman, *Phys. Rev.* B **68**, 115415-115425 (2003).

26. "Dimensional Change as a Function of Charge Injection in Graphite Intercalation Compounds: A Density Functional Theory Study", G. Sun, M. Kertesz, J. Kürti, R.H. Baughman, *Phys. Rev. B* **68**, 125411-125417 (2003).

27. "Super-Tough Composite Carbon Nanotube Fibers for Electronic Textiles", R.H. Baughman, Association of Asia Pacific Physical Societies Bulletin **13**, No. 4, 13-15 (2003).

28. "Optical Fiber Switch Based on Carbon Nanotube Actuation", L.S. Fifield, A.M. Zipperer, R.H. Baughman, L.R. Dalton, *Materials Research Society Symposium Proceedings* **772** (Nanotube-based Devices), 17-22 (2003).

29. "Investigation of Ionic Liquids as Electrolytes for Carbon Nanotube Electrodes", J.N. Barisci, G.G. Wallace, D.R. MacFarlane, and R.H. Baughman, *Electrochemistry Communications* **6**, 22-27 (2003).

30. "Ultrafast Spectroscopy of Excitons in Single-Walled Carbon Nanotubes", O.J. Korovyanko, C-X. Sheng, Z.V. Vardeny, A.B. Dalton and R.H. Baughman, *Phys. Rev. Lett.* **94**, 017403-1 to 017403-4 (2004).

31. "Continuous Carbon Nanotube Composite Fibers: Properties, Potential Applications, and Problems", A.B. Dalton, S. Collins, E. Muñoz, J. M. Razal, V.H. Ebron, J.P. Ferraris, J.N. Coleman, B.G. Kim, and R.H. Baughman,*J. Materials Chemistry* **14**, 1-3 (2004).

32. "Mechanical Properties of Nanotube Sheets: Alterations in Joint Morphology and Achievable Moduli in Manufacturable Materials", L. Berhan, Y. B. Yi, A.M. Sastrya, E. Munoz, M. Selvidge, and R.H. Baughman, *J. Applied Physics* **95,** 4335-4345 (2004).

33. "Structure and Dynamics of Carbon Nanoscrolls", S.F. Braga, V.R. Coluci, S.B. Legoas, R. Giro, D.S. Galvão, and Ray H. Baughman, *Nano Letters* **42**, 881-884 (2004).

34. "Individualities and Average Behavior in the Physical Properties of Small Diameter Single-walled Carbon Nanotubes", J. Kurti, V. Zolyomi, M. Kertesz, G. Sun, R.H. Baughman, H. Kuzmany, *Carbon* **42**, 971-978 (2004).

35. "Multifunctional Carbon Nanotube Composite Fibers", E. Muñoz, A.B. Dalton, S. Collins, M. Kozlov, J. Razal, J.N. Coleman, B.G. Kim, V.H. Ebron, M. Selvidge, J.P. Ferraris and R.H. Baughman, *Advanced Engineering Materials* **10,** 801-804 (2004).

36. "Spinning Solid and Hollow Polymer-Free Carbon Nanotube Fibers", M. E. Kozlov, R. C. Capps, W. M. Sampson, V. H. Ebron, J. P. Ferraris, R. H. Baughman, *Advanced Materials*, in press.

37. "Highly Conducting Carbon Nanotube/Polyethylenimine Composite Fibers", E. Muñoz, D.-S. Suh, S. Collins, M. Selvidge, A. B. Dalton, B. G. Kim, J. M. Razal, G. Ussery, A. G. Rinzler, M. T. Martínez, and R. H. Baughman, *Advanced Materials*, in press.

38. "Ultrafast Spectroscopy of Excitons in Semiconducting Carbon Nanotubes", C. X. Sheng, Z. V. Vardeny, A.B. Dalton, and R.H. Baughman, *Synthetic Metals*, submitted.

FILED PATENT APPLICATION

"Polymer-Free Carbon Nanotube Assemblies", Mikhail E. Kozlov, Ryan C. Capps, Von Howard Ebron, John P. Ferraris, Ray H. Baughman, Patent Application 13991-P002US

3.1 MODELING AND DESIGN RULES (task leader: Anvar Zakhidov)

Work on Task 3.1 was not funded in the second program year. Thus the work summarized here was performed in the first four quarters of the program. An article on the variations of CC bonds in neutral and charged SWNTs was published in J. Chem. Phys. These variations display interesting regularities that gradually change with doping levels. A periodicity of three in the difference in nanotube indices was found and interpreted by Brillouin zone mapping of nanotube states to graphite states. Another significant finding is that the bandgaps of the semiconducting nanotubes go through a maximum (1 eV) as a function of tube radius. The average bond strain as a function of charge transfer, if averaged over various types of nanotubes, is close to the values characteristic for large diameter tubes and to graphene.

Work was performed to systematically evaluate quantum mechanical approaches for determining intertube charge transfer hopping. This is essential to evaluate the intertube charge distribution, which in turn is needed for calculating the maximum charging limit of nanotubes in bundles. We found that the semi-empirical calculations, which are widely used widely for calculating intermolecular hopping, are unreliable and provide qualitatively incorrect inter-tube interactions. We also showed that other commonly used approaches, such as INDO, give transfer integrals that are completely unreliable. The *ab initio* approach proves superior results in terms of convergency, consistency, and agreement with available experimental results. Our results indicate that basis set convergence can be achieved, and that the plane wave basis set calculations agree well with the converged atomic basis set results for intermolecular hopping values. Thus, we turned to intertube interaction calculations as the next step, using *ab initio* molecular and plane wave calculations. The primary result is that the 6-31G* level calculations agree within a few percent with the "medium" plane wave calculations of the VASP methodology at the PW91 (GGA) level of density functional theory. Calculations beyond these basis sets do not change more than a few percent, so they can be considered as converged. We settled on this level of basis set. This benchmarking was necessary

preparation for moving to the next level of aggregation, which includes inter-tube interactions for multiwalled tubes and tube bundles.

The two curves below illustrate the sensitive dependency of the intermolecular, and by extension, intertube interactions to the relative position of the molecules. Here the estimated bandwidth parameter is plotted as a function of parallel slip for a dimer of two ethylene molecules put in a parallel position at 3.345 Angstroms. One of four possible combinations is given below.
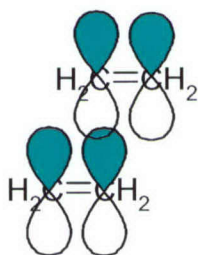
The two bandwidth parameters refer to the HOMO and the LUMO bands. Their very different behavior is a consequence of the nodes present in the LUMO but not in the HOMO. The large variations and the sensitivity to the specific contact of the two molecules, and by implication the relative orientation of the neighboring nanotubes, will have a large effect on the resulting intertube hopping, and therefore on the intertube charge transfer.
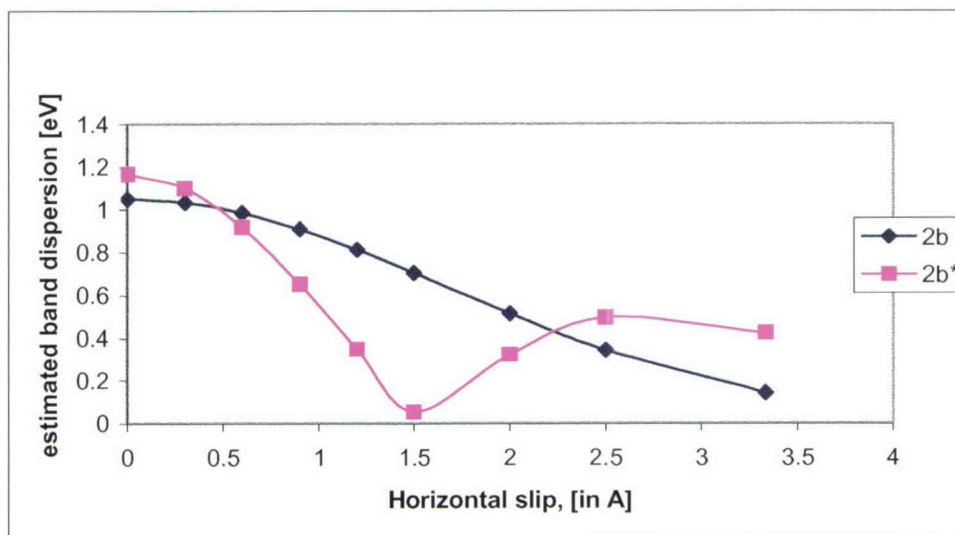
3.2 MATERIALS DEVELOPMENT AND CHARACTERIZATION
(task leader: Norman Barisci)

Electrolytes for Nanotube Composites

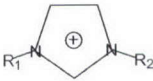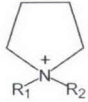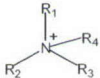*Characterization of Ionic Liquid Electrolytes*

A comprehensive survey and evaluation of solvent-free electrolytes (referred to, when in liquid state, as ionic liquids or molten salts) was conducted. Attention was focused mainly on electrolytes that are liquid at room temperature (RT). The electrochemical tests, employing voltammetry, chronoamperometry and electrochemical impedance spectroscopy (EIS), were conducted using carbon nanotube (CNT) electrodes as well as conventional electrodes (platinum, glassy carbon).

In general terms, the most important criteria used to evaluate ionic liquids (ILs) were: conductivity, electrochemical window, other electrochemical properties (*e.g.*, voltammetry, capacitance), chemical and electrochemical stability, hydrophobicity and viscosity. The generic structure, chemical name and abbreviations for the most common ions producing ionic liquids are given in Table 3.2.1.

Room Temperature Ionic Liquids

When only the cation is considered, the trend in electrolyte conductivity is $I_{xx}>P_{xx}>N_{xxxx}$, suggesting that the best candidates should come from IL containing the I_{xx} or P_{xx} cations. The trend in anion conductivity is **DCA>TFSA>TF>TFB>HFP**. As a general rule, the ionic conductivities of ILs are somewhat lower than that of TBAHFP (tetrabutyl ammonium hexafluorophosphate)/ACN (acetonitrile) and similar electrolytes, but are still sufficiently high for most of the envisaged applications. Despite the lower conductivity of IL, the capacitance values for a CNT electrode obtained in different IL are in the same range as those measured in TBAHFP/ACN.

Table 3.2.1. Cations and anions of ionic liquids.

Chemical name	Structure	Abbreviation[a]
R_1,R_2-Imidazolium		$\mathbf{I_{xx}}$
R_1,R_2-Pyrrolidinium		$\mathbf{P_{xx}}$
R_1,R_2,R_3,R_4-Ammonium		$\mathbf{N_{xxxx}}$
Bis(trifluoromethanesulfonyl) amide	$(CF_3SO_2)_2N^-$	**TFSA**
Triflate	$CF_3SO_3^-$	**TF**
Dicyanimide	$N(CN)_2^-$	**DCA**
Hexafluorophosphate	PF_6^-	**HFP**
Tetrafluoroborate	BF_4^-	**TFB**

[a] Subscripts (x) indicate length of alkyl chains (R_i) attached to N-atoms

Typical cyclic voltammograms for a CNT sheet in IL are shown in Fig. 3.2.1. In all cases the curves are basically featureless, with no signs of redox processes. $\mathbf{I_{41}HFP}$ is a less effective electrolyte with respect to the others as is apparent from the lower currents generated and the slower response at the ends of the potential scan. Clearly, $\mathbf{I_{21}TFSA}$ and $\mathbf{I_{21}DCA}$ provide sufficient ionic mobility to prevent degradation of the CNT electrode performance and compare very well with 1 M TBAHFP/ACN.
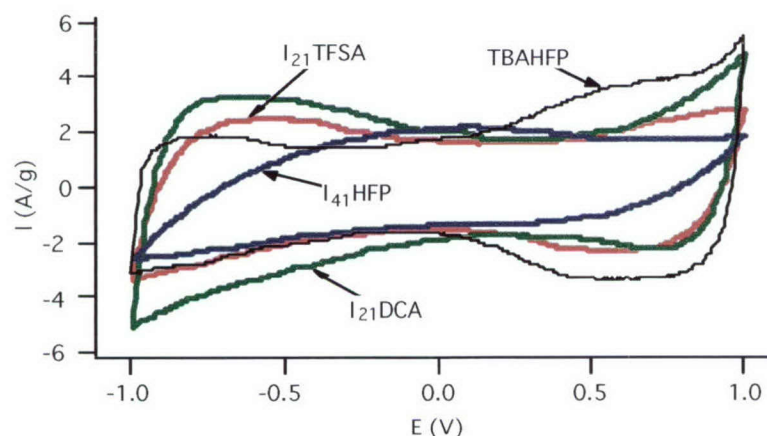
Fig. 3.2.1. Cyclic voltammograms for a CNT sheet electrode in ionic liquids and in 1 M TBAHFP/ACN, scan rate 50 mV/s.

The ability to remain stable upon the application of relatively large potentials is a key requirement for electrolytes to be used in our CNT devices. The stable potential window for selected IL is presented in Table 3.2.2. These data suggest that the **TFSA** anion is particularly useful in imparting resistance to decomposition of the electrolyte. In particular, the wide potential window of $\mathbf{P_{13}TFSA}$ points at an IL that could provide outstanding capabilities for actuators and capacitors, both of which rely on large potential differences to enhance their performance.

High Temperature Ionic Liquids

The focus here was to evaluate salts that are solid at room temperature and become liquid above room temperature. They are referred to as high temperature (HT) ionic liquids. Based on this criterion, these HT-IL have two possible applications: as liquid electrolytes above RT and, in some cases (plastic crystals), as solid electrolytes at temperatures below their melting point. A wide survey of these materials was conducted. The overall electrochemical properties of HT-IL, including voltammetric or redox behavior, capacitance and electrochemical window, are expected to be similar to those described for RT-IL.

Table 3.2.2. Potential window of selected ionic liquids.

Ionic liquid	Potential window (V)
I_{21}TFSA	4.4
I_{21}DCA	3.0
I_{31}TFSA	4.0
I_{41}HFP	3.4
P_{13}TFSA	5.5
P_{13}TFB	4.0

Solid Electrolytes Based on Ionic Liquids

The favored approach to produce solid electrolytes with the desired properties involves an IL dispersed in a polymer (polymer-in-ionic liquid, PIL) that provides the solid matrix for the composite system. In general, these electrolytes are more conductive than other solid electrolyte systems. For this project the PIL electrolytes considered were based on poly(methyl methacrylate) (PMMA) and I_{21}TFSA, I_{41}HFP or P_{13}TFSA. Of particular interest were systems in which the polymer is polymerized *in-situ* from a solution of the monomer in the IL.

The general electrochemical behavior of the PIL electrolyte is very similar to that of the corresponding IL. Fig. 3.2.2 shows cyclic voltammograms for both material types and indicates that the addition of PMMA does not introduce any spurious redox process nor does it reduce the charging current significantly when moderate scan rates (50-100 mV/s) are used.
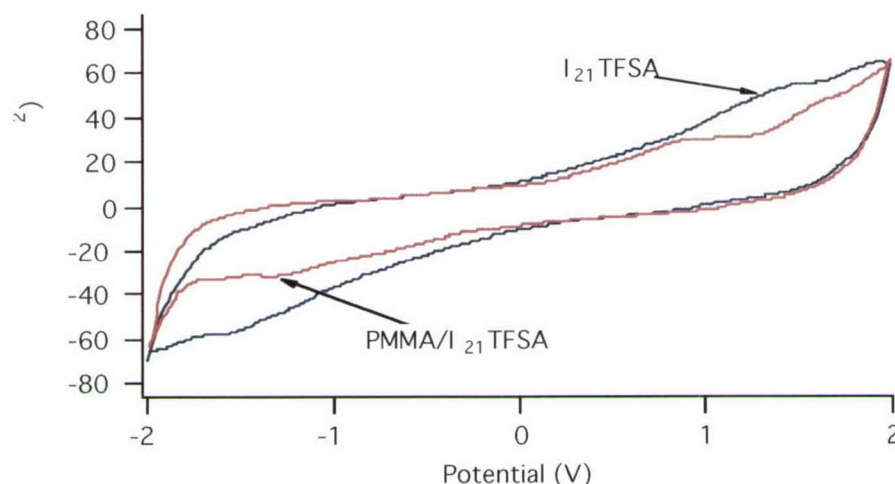
Figure 3.2.2. Cyclic voltammograms for a PIL electrolyte (30/70 PMMA/I_{21}TFSA) and the corresponding IL (I_{21}TFSA), platinum electrodes, 2-electrode system, scan rate 50 mV/s.

The capacitive behavior of the PIL electrolyte is also very adequate and follows well the expected variation with scan rate. Table 3.2.3 compares the performance of PIL electrolytes and IL for two cases. First, as expected, I_{21}TFSA provides larger charging currents and capacitance than I_{41}HFP on account of its higher conductivity. Second, the data show that these features are transferred to the PIL electrolytes based on the same IL, highlighting the importance of using highly conducting IL in the preparation of NT/electrolyte composite materials.

A feature of great interest in the results of Table 3.2.3 is the small charging time constant (*RC*) observed for the PIL electrolytes when compared to those for the pure IL. This remarkable feature suggests that solid-state devices based on these electrolytes may be able to operate at rates greater than initially expected, based on previous experience with traditional solid-state electrolytes.

Table 3.2.3 Electrochemical properties of electrolytes

Electrolyte	Max current (mA/cm^2)	Time constant[a] (msec)	Capacitance[b] (μF/cm^2)
I$_{41}$HFP	29.4	<1.5	22.3
I$_{21}$TFSA	50.8	<1.5	89.2
PMMA/I$_{41}$HFP	1.1	2.5	24.3
PMMA/I$_{21}$TFSA	4.0	<1.5	54.6

[a] Time constant (RC) measured for application of a 0.2 V pulse at 0.0 V, platinum electrode, 3-electrode system.
[b] Capacitance measured at 0.0 V, platinum electrode, 3-electrode system.

Composite Formation and Device Fabrication

Using the selected PIL electrolyte, the preparation of CNT/electrolyte composites was undertaken. This involved the *in-situ* polymerization of the MMA monomer in the presence of IL and CNT electrodes. Two identical CNT sheet electrodes (10 mm x 2 mm) were placed facing each other in parallel separated by a 2 mm gap. A cyclic voltammogram showed good capacitive behavior without high electrical resistance.

The aim of the next stage was to fabricate a preliminary, simple, small device to demonstrate the possibility of building more sophisticated assemblies using the same materials and principles. A compact, flexible, thin-layer device was constructed using a porous membrane (PVDF, 0.22 μm pore size) as the basic component (Fig. 3.2.3). First, both sides of the membrane were sputter-coated with a thin layer of platinum. On one side, a thin film of CNT was next deposited by filtration through the membrane. The underlying platinum layer was necessary to provide adhesion for the CNT film which would otherwise peel off spontaneously (this may not be the case with other membrane materials). The total thickness of the device was 121 μm with the CNT layer accounting for 5 μm.
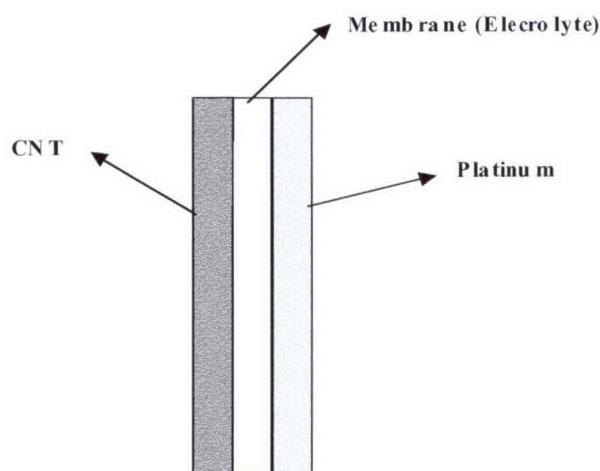
Figure 3.2.3. Schematic edge view of CNT/membrane (electrolyte)/Pt assembly.

Device with Liquid Electrolyte

A strip of the CNT/membrane/Pt "sandwich" (7 mm x 2.2 mm) was immersed in IL which percolated through the outer layers and into the separating membrane. The device, consisting effectively of two electrodes separated by an electrolyte layer, and better described as CNT/membrane (IL)/Pt, could then be tested as a unimorph actuator or as a capacitor. Measurements to assess both types of applications were carried out to establish the potential usefulness of this approach, keeping in mind the limitations of this initial attempt.

A comparison of cyclic voltammograms of the device within and outside the liquid electrolyte is presented in Fig. 3.2.4. It can be seen that, remarkably, no difference is observed between the curves, suggesting that no degradation of performance occurs in the absence of electrolyte outside the multilayer assembly.
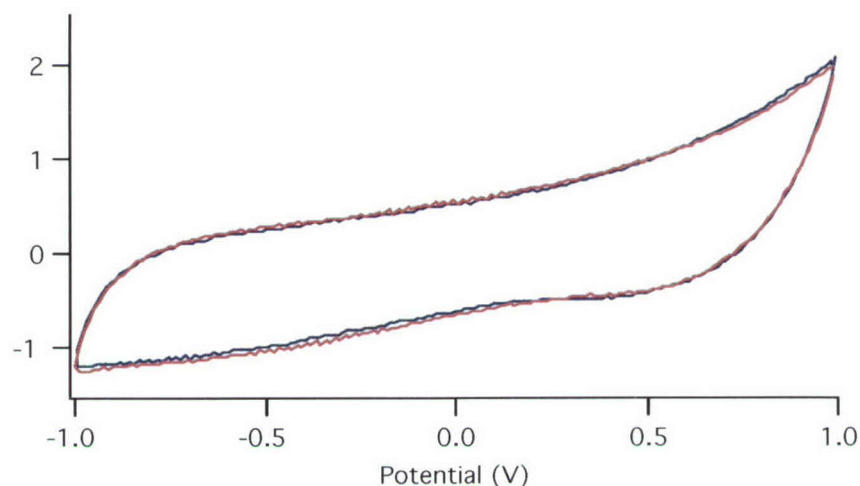
Figure 3.2.4. Cyclic voltammograms for a CNT/membrane/Pt assembly obtained first immersed in electrolyte (I_{21}TFSA) and next in air, 2-electrode system, scan rate 50 mV/sec.

Further studies revealed that the multilayer device could be charged very rapidly as shown in Fig. 3.2.5. The charging time constant (*RC*) was 3 msec. This is the smallest time constant ever measured in the program for CNT films. The previous lowest value (~15 msec) was achieved in high concentration aqueous electrolytes (1 M NaCl). This result highlights the efficiency of the thin-layer approach as well as the advantage of using highly conducting, solvent-free liquid electrolytes.
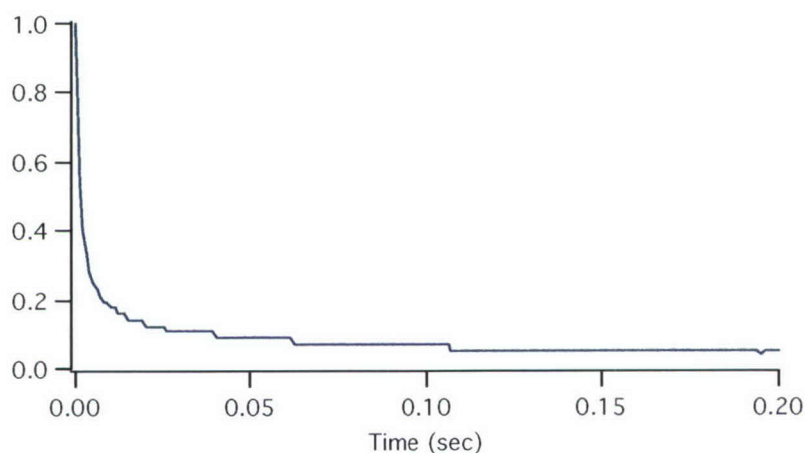

Figure 3.2.5. Charging current (arbitrary scale) as a function of time for a CNT/membrane (I_{21}TFSA)/Pt assembly in air, for application of a 0.2 V potential pulse at 0.0 V in a two-electrode system.

17

Device with Solid Electrolyte

In the final stage an all-solid-state-device was prepared using a PIL electrolyte instead of an IL. For this purpose a strip of the multilayered assembly was soaked in a monomer/IL/crosslinker/initiator reacting mixture to allow percolation of the liquid into the porous structure. The strip was then removed from the reacting solution and subjected to the polymerization temperature. As a result a multilayer assembly, containing a PIL electrolyte (30:70 PMMA:I_{21}TFSA) was obtained which could be described as CNT/membrane (PIL)/Pt.

The produced solid-state device was put through the same series of tests performed on the IL analogue. The cyclic voltammogram (Fig. 3.2.6) did not show any spurious responses and was almost identical to that for the "IL device" indicating that the solid electrolyte did not affect the basic electrochemical behavior of the device.
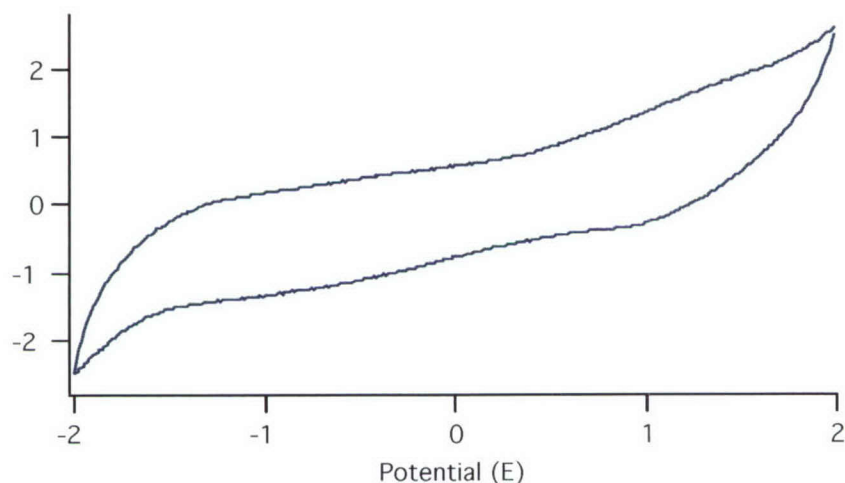

Figure 3.2.6. Cyclic voltammogram (arbitrary current scale) for a CNT/membrane (30:70 PMMA:I_{21}TFSA)/Pt assembly obtained in air, two-electrode system, scan rate 50 mV/sec.

The charging rate of the PIL device was also remarkably fast with a measured time constant (*RC*) similar to that for the "IL device". The close proximity of the electrodes probably minimizes the resistance to ion conduction across the solid matrix.

Conclusions

Based on an evaluation of key properties two ionic liquids were identified as the best options: I_{21}TFSA (methyl, ethyl-imidazolium bis(trifluoromethanesulfonyl) amide) and P_{13}TFSA (methyl, propyl-pyrrolidinium bis(trifluoromethanesulfonyl) amide). These electrolytes offer relatively high conductivity, wide electrochemical window and good hydrophobicity.

A polymer-in-ionic liquid electrolyte (PIL) was selected for use in solid-state composites and devices. The electrolyte (PMMA/I_{21}TFSA) can be formed *in-situ* using a selected range of component concentrations. The PIL electrolyte exhibits high conductivity, good electrochemical behavior, and fast charging rates, all of which compare very well with the corresponding properties of ionic liquids.

CNT/electrolyte composites were prepared *in-situ* using either the selected IL or PIL electrolyte and CNT sheet electrodes. The composites exhibited satisfactory electrochemical and mechanical properties.

Using a newly developed approach, simple, compact, flexible devices capable of operating as primitive actuators or as capacitors were constructed using an IL electrolyte. These devices exhibited excellent electrochemical properties and the fastest charging rate thus far for CNT films (3 msec). Devices similar to those described above were constructed using a PIL electrolyte. These solid-state assemblies performed similarly to those based on ionic liquid electrolytes.

Modification and Characterization of Fibers

The approach used for modification of the standard coagulation-spun, single walled nanotube fibers comprised two steps, annealing the fiber in air to remove PVA and chemical modification of the annealed fiber to increase mechanical strength. The fibers produced were characterized for their electrochemical, mechanical, and where possible, actuation properties. In all cases several replicates were tested.

Fibers were annealed at 200 °C and 210 °C with the aim of increasing the fiber conductivity without introducing too much brittleness. The post-annealing modification procedure involved the electrochemical infiltration of small amounts of the polypyrrole/p-toluene sulphonate (PPy/PTS) conducting polymer. The main variable controlling the amount of deposited polymer was the number of potential cycles (3-50) applied during polymerization. For the sample annealed at 210°C it was possible to observe more polymer deposition as indicated by the larger current increase after the same number of polymerization cycles.

The effect of the polymer on the electrochemistry (mainly capacitive) of the fiber can be seen in Fig. 3.2.7 where the shape and current levels of the voltammogram change after polymer deposition.

The capacitance of the modified fibers in either aqueous (1 M NaCl) or ionic liquid (EMITFSA) electrolyte was always greater than that for the annealed-only (bare) fiber, as expected from the increased conducting surface area. Typical capacitance values are given in Table 3.2.4. In general the increase in capacitance for fibers annealed at 200 or 210 °C followed the increase in the number of polymerization cycles. The highest values observed for the modified fibers were around 1-2 F/g, which represents an increase of up to 3 orders of magnitude with respect to the values for the bare fibers.
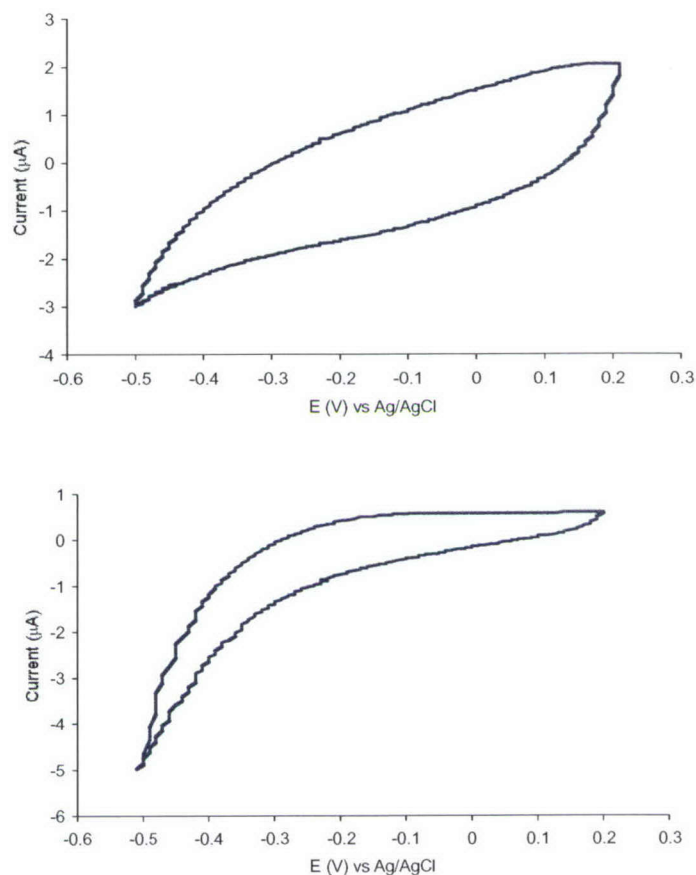
Figure 3.2.7. Cyclic voltammogram (scan rate 50 mV/s) for an annealed fiber (210 °C) in 0.1 M pyrrole and 0.1 M PTS before (top) and after (bottom) polymer deposition for 50 cycles.

Table 3.2.4. Gravimetric capacitance (0.0 V) for CNT fibers annealed (200 °C) and modified.

Fiber	Cap 1M NaCl (F/g)	Cap EMITFSA (F/g)
Bare	0.001	0.001
20 cycles	0.43	0.28
50 cycles	0.84	0.01

Estimates of mechanical properties were made from force/extension data obtained from constant displacement rate tests on the various fibers. One main observation in relation to mechanical properties is that the thicker conducting polymer coatings (more cycles) appear to increase the fiber modulus (Table 3.2.5). This may be due to increased adhesion/bonding between the fibers promoted by the polymer. Interestingly, the strain at break also increases as more polymer is added (up to a point), resulting in fibers significantly tougher compared with the bare annealed fibers. Finally, there is also a ~3 fold increase in strength observed for the thicker polymer-coated fibers. Again this is probably caused by better bonding between the fibers at the junctions.

The fibers annealed at 210 °C followed the general trends described above, but were much more brittle, so some fibers broke during mounting for mechanical testing. Notwithstanding this limitation, the fibers annealed at 210 °C still exhibited improvements compared with the bare fibers, as seen in Table 3.2.5.

Table 3.2.5. Mechanical data for CNT fibers annealed (200 °C) and modified by addition of polypyrrole (various cycles).

Fiber Treatment	Modulus (GPa)	Strain at Break (%)	Breaking Strength (MPa)
Unannealed	0.72	30	40
Annealed (200 °C) / Bare	1.1	9	70
Annealed (200 °C) / 3 cycles	2.6	17	62
Annealed (200 °C) / 6 cycles	2.4	18	55
Annealed (200 °C) / 10 cycles	6.1	4.1	147
Annealed (200 °C) / 20 cycles	4.9	20.8	150
Annealed (200 °C) / 50 cycles	6.8	37	225
Annealed (210 °C) / 50 cycles	1.3	22.5	162

The actuation characteristics of annealed/bare and annealed/polymer modified fibers were evaluated in ionic liquid electrolyte (EMITFSA). The behavior observed was rather poor. The main limitation on the actuation performance was the irreversible "creep" that was noted upon potential cycling.

Conclusions

We have investigated the means for converting largely insulating PVA/CNT fibers into conductive fibers that show appreciable capacitance. With the fibers available to date we have been able to produce improvements in conductivity and capacitance by air-annealing the fibers at temperatures from 200-220 °C. One consequence of the air-annealing is deterioration in mechanical strength. To counter this decrease in strength, we have subsequently modified the annealed CNT fibers by applying a thin coating of polypyrrole within the porous CNT network. The polymer modification has significantly improved the mechanical properties (elongation at break, modulus and strength) compared with the annealed fibers. The polymer-modified fibers retain the conductivity and capacitance of the annealed fibers. Actuation testing of the polymer modified fibers produced some small reversible displacements, but problems remain with irreversible deformation and rupture after only a short time.

Characterization of Welded CNT Sheets

CNT sheets, unwelded (U) and welded (W), were received from the University of Colorado group for electrochemical and actuation characterization. The electrochemical properties were evaluated in aqueous electrolyte (1 M NaCl) and ionic liquid (EMITFSA) electrolyte. The cyclic voltammograms for all sheets exhibited similar and good capacitive behavior and absence of spurious redox responses (Figs. 3.2.8 and 3.2.9). The capacitance values (0.0 V) for samples U and W in both electrolytes were on average around 30 F/g.
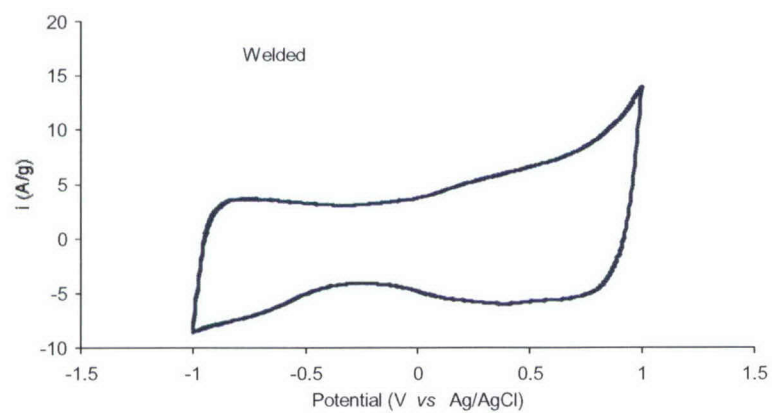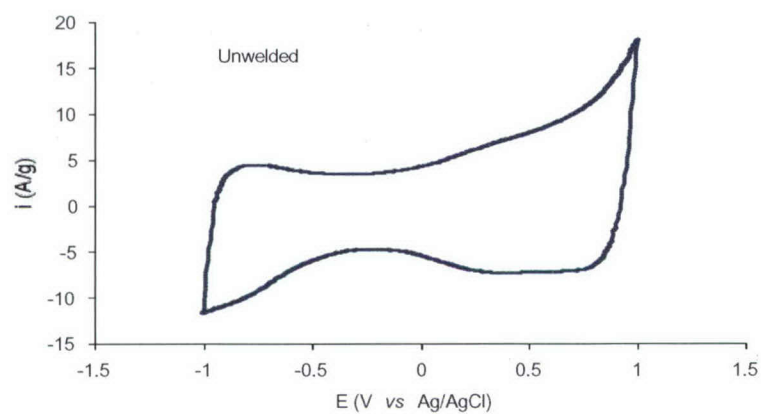
Figure 3.2.8. Cyclic voltammograms for unwelded (top) and welded (bottom) CNT sheets in 1 M NaCl, scan rate 50 mV/s.
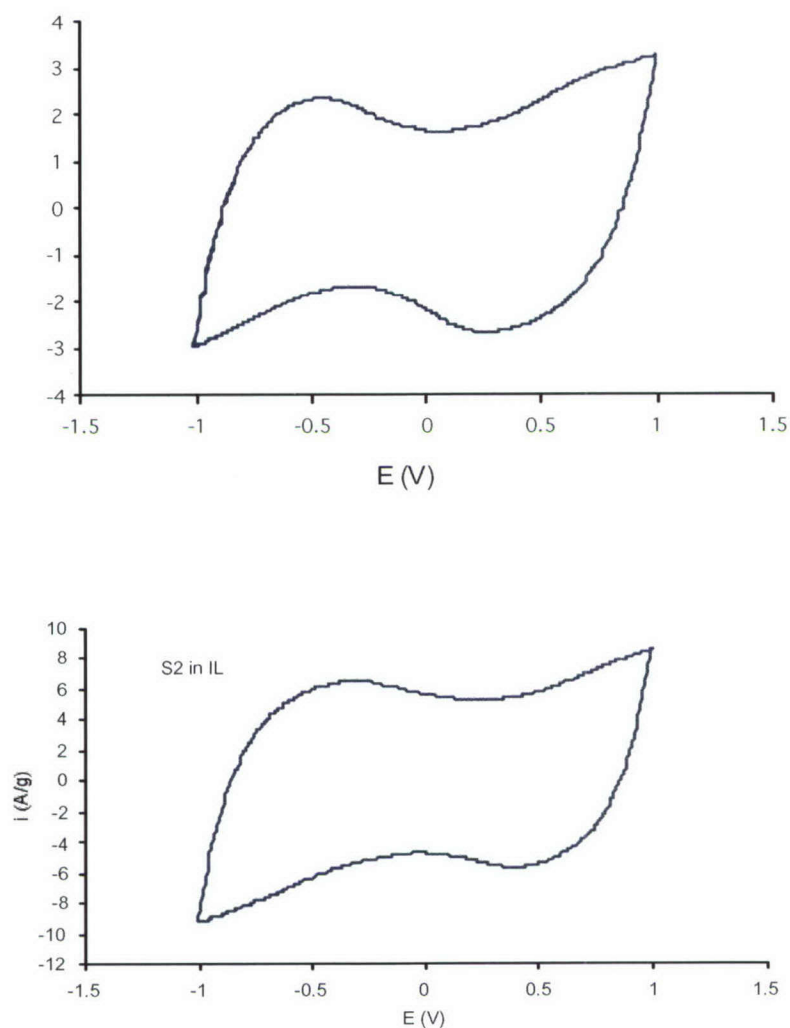
Figure 3.2.9. Cyclic voltammograms for unwelded (top) and welded (bottom) CNT sheets in EMITFSA, scan rate 50 mV/s.

The actuation tests (results reported elsewhere in this report) were conducted isotonically (20 mN load) in organic (0.1 M TBATFB/acetonitrile) and ionic liquid (EMITFSA) electrolyte. Displacement curves for the unwelded (U) and welded (W) samples under cyclic voltammetric conditions are shown in Figs. 3.2.10 and 3.2.11. All these curves exhibit the typical shape already observed previously for CNT sheets. Also as previously, significant hysteresis exists as shown by the wide separation between the forward and reverse scans. No visible differences in behavior were recorded between the organic and IL electrolytes, suggesting a similar strain generating mechanism.
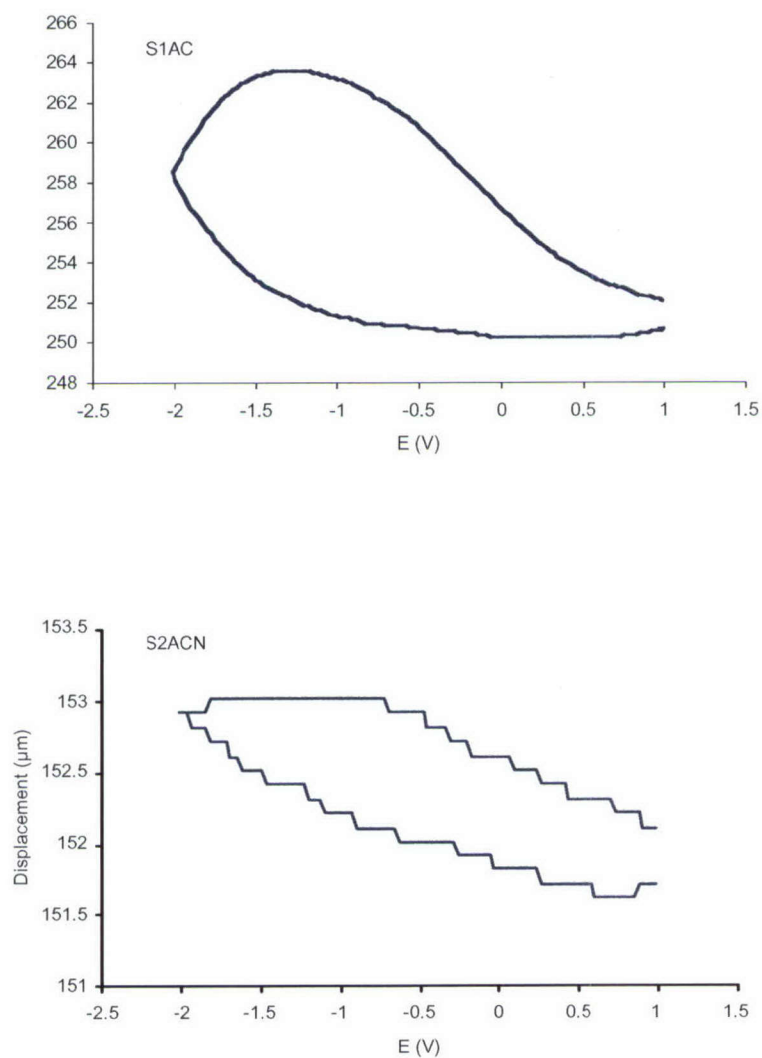
Figure 3.2.10. Displacement curves (microns) for unwelded (top) and welded (bottom) CNT sheets upon application of cyclic voltammetric potential ramp between 1.0 and -2.0 V in 0.1 M TBATFB/acetonitrile, scan rate 50 mV/s.
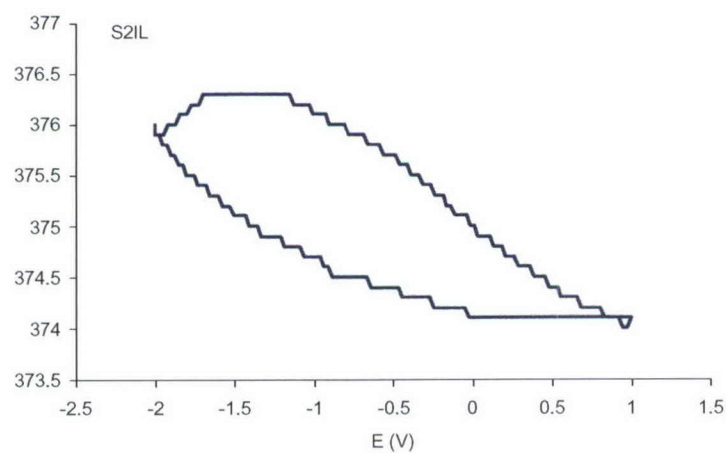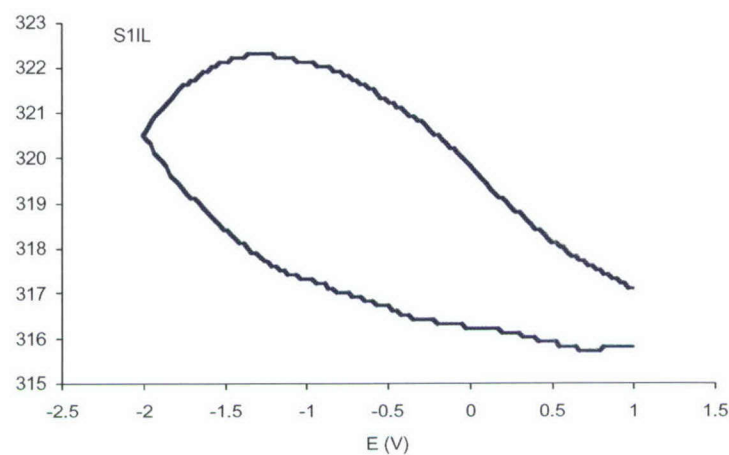
Figure 3.2.11. Displacement curves (microns) for unwelded (top) and welded (bottom) CNT sheets upon application of cyclic voltammetric potential ramp between 1.0 and -2.0 V in EMITFSA, scan rate 50 mV/s.

The actuation strain for samples U and W is similar in both electrolytes (0.1-0.2 %) although the welded sample shows slightly smaller actuation strains than the unwelded one.

Conclusions

The electrochemical and actuation properties of unwelded and welded CNT sheets were compared in different electrolytes. Considering the best of welded sample evaluated no degradation in electrochemical behavior, capacitance level or strain generating capability was observed for the welded sample with respect to the untreated CNT sheet.

Special Actuation Studies on CNT Sheets

A special study using unwelded CNT sheets in organic electrolyte has shown that all CNT sheets appear to exhibit the expected actuation behavior, with a minimum in the strain-potential curve. However, in laser-produced and HiPco CNT sheets this feature is rapidly obscured by irreversible changes (creep) produced when potentials greater than +/- 0.8 V approximately are applied. This effect is markedly enhanced when the potential is applied in the form of relatively long pulses.

In contrast, investigated Carbolex sheets (comprising SWNTs made by the carbon arc method) show much less creep and generate higher strain. As a result of these properties, the Carbolex material exhibits the expected strain-potential change over a relatively wide potential range. The strain-charge data shows that slightly greater strain and higher charge are associated with negative-going pulses in relation to similar pulses going in the positive direction.

3.3 CARBON NANOTUBE DEBUNDLING, SPINNING and WELDING (task leader, Alan Dalton)

Dispersion and De-bundling

The main thrust of this task area was to develop methods to produce spinning solutions of isolated single wall nanotubes in solution to be used as "spinning ink" to make fibers. As-produced carbon nanotubes pack into crystalline ropes due to strong inter-tube van der Waals interactions, and the ropes further aggregate into tangled networks. Because carbon nanotubes are extremely hydrophobic and form large aggregates, they have low solubility (i.e., dispersibility) in most organic solvents and are insoluble in water. We have analyzed several different dispersion systems from organic solvent/conjugated

28

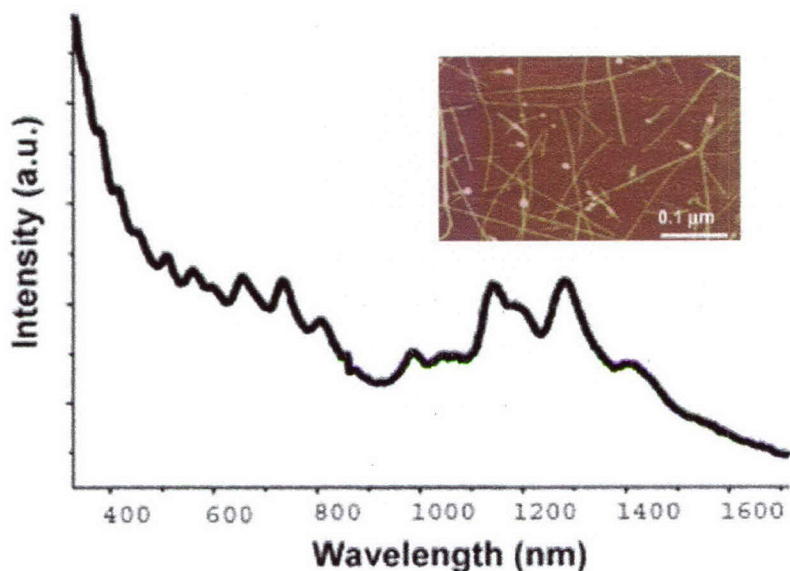polymer solutions, to aqueous/biological polymer systems to commercially available surfactants.

Figure 3.3.1 Absorption spectrum of peptide/SWNT dispersion. The well resolved features demonstrate the ability of peptide to debundle SWNTs in aqueous solution. The sharp feature at _860 nm is due to a grating and detector change associated with the spectrophotometer. Dispersions of individual peptide-wrapped SWNTs were prepared in deionized water using a combination of ultrasonication and high speed centrifugation. Solutions of 50 and 100 μM nano-1 were prepared using deionized water. Then, 0.75 mg of raw SWNTs was added to a 1 mL volume of peptide solution in an eppendorf tube, and the mixture was vortexed for approximately 1 minute. Samples were sonicated for 4 minutes at a power level of 10 W using a tip sonicator, yielding a dense black dispersion. The sonicated samples were first centrifuged for 10 minutes at 700 x g to remove any large particulates that did not go into solution. The upper 75% of the supernatant was recovered and further centrifuged for 30 minutes at 50,000 x g and 4 °C. The upper 50% of the supernatant containing individual peptide-wrapped SWNTs] was recovered and transferred to a clean tube for further study. Inset - AFM images of a deposited peptide assisted dispersion on mica. Height analysis indicates that the majority of structures are individual carbon nanotubes.

The highlights of this task area are:

- Peptide assisted and anionic surfactant assisted aqueous dispersions of isolated carbon nanotubes.

During the program, we have demonstrated that nanotubes can be wrapped with a wide variety of molecules, including surfactants, conjugated polymers, oligosaccharides and biological molecules such as peptides. Amphiphilic helical polypeptides efficiently

disperse carbon nanotubes. Moreover, using a combination of controlled sonication and centrifugation, we were able to use these amphiphilic helical polypeptides to obtain debundled nanotubes in stable dispersions. A significant advantage of coating nanotubes with peptides is that the amino acid sequence of the peptides can be controlled to promote the interaction of coated nanotubes with each other in the resulting fibers. The electronic absorption spectra of thin films or solutions containing predominantly aggregated SWNTs are dominated by inhomogeneously broadened optical transitions superimposed in the absorption tail of the π-plasmon resonance (that peaks at about 5 eV). In contrast the absorption spectrum of the peptide-assisted aqueous dispersion of SWNTs contains a number of isolated subbands. This shows that the inhomogeneity of the SWNTs in solution is smaller than for the films containing mainly isolated peptide wrapped SWNTs. Figure 3.3.1 shows the resulting absorption spectrum. The inset is an atomic force microscope image of a deposit dropped on to mica from this dispersion. Height analysis indicates that over 90% of the structures are isolated individual nanotubes wrapped in peptide.

- Development of new spinning solutions using Lithium Dodecyl sulfate as a surfactant

A particularly facile method to achieve dispersions of SWNTs involves the use of ionic surfactants. In our studies we use lithium dodecyl sulfate (LDS). Although many other detergents were evaluated, LDS was found to be superior in producing homogeneous optically pure dispersions free of large aggregates. Using a similar phase behavior analysis outlined by Vigolo et al. for sodium dodecyl sulfate dispersions, the optimum spinning solution contains 0.4 % (wt) SWNTs in a 2% (wt) LDS/water solution. The coagulation solution was prepared by dissolving PVA (77,000 Mw) in de-ionized water to make a 5% (wt) coagulating solution. The resulting fibers spun from these solutions have properties far superior to those spun from sodium dodecyl sulfate. Continuation of this work will involve studies to ascertain the exact reasons for these differences.

Nanotube Spinning

Continuous Flow Coagulation Spinning of Composite Fibers

During the course of the program, the UTD team developed a new method to spin nanotube dispersions into super-tough and strong composite fibers. The main advances relating to these findings are described below. A schematic of the spinning apparatus is shown in Fig. 3.3.2. The basis of this system is a peristaltic pumped circulating flow of PVA operating in an open loop consisting of a 1.5 m long, 0.40 cm diameter glass pipe, flex-tubing, and a polymer reserve. The spinning solution is syringe injected into the center of the polymer flow. The spinning solution coagulates upon contact with the polymer forming a gel-like ribbon that flows down the length of the pipe before being released into a rotating water bath where it is collected on a mandrel. Our procedure produces elastomers that surpass 100 meters in length, and the volume of spinning solution used is the limiting factor on the length. The resulting gel fiber is structurally stable and can be drawn from the bath at a rate of ~1 meter per minute, passed over a number of godets, dried and collated into a dense fiber on a reel. The diameter of the resulting fibers (10-60 μm) is controlled through variation of the ratio of coagulation solution flow rate to spinning solution flow rate.

One of the most important parameters contributing to the quality of the fibers is the nature of the flow in the pipe. It is expected that the best quality fibers will be formed when the flow is laminar. For turbulent flow, local variations in the flow velocity would be expected to cause localized stretching or compressions in the precursor fiber leading to the formation of weak points. Laminar flow in a closed pipe occurs when the Reynolds number is less than ~2000. The Reynolds number, R is given by Equation 1 where r is the pipe radius, v_a is the average flow velocity, ρ is the fluid density and η is the fluid velocity. In our apparatus the pipe was made of glass with a radius of 3mm, the average velocity was always less than 15 cm/s and the density was approximately 1010 kg/m^3.
In all cases the viscosity was close to 60 cP. This gives a Reynolds number of less than 15, indicating laminar flow in all cases.

$$R= 2rv_a\rho/\eta \qquad\qquad \text{Equation 1}$$

The resulting fiber cross section is ribbon like, and has this non-circular structure as a result of the gel formation process. The jet of the spinning solution (with an initially cylindrical shape) first forms and thickens on the external surface in closest proximity to
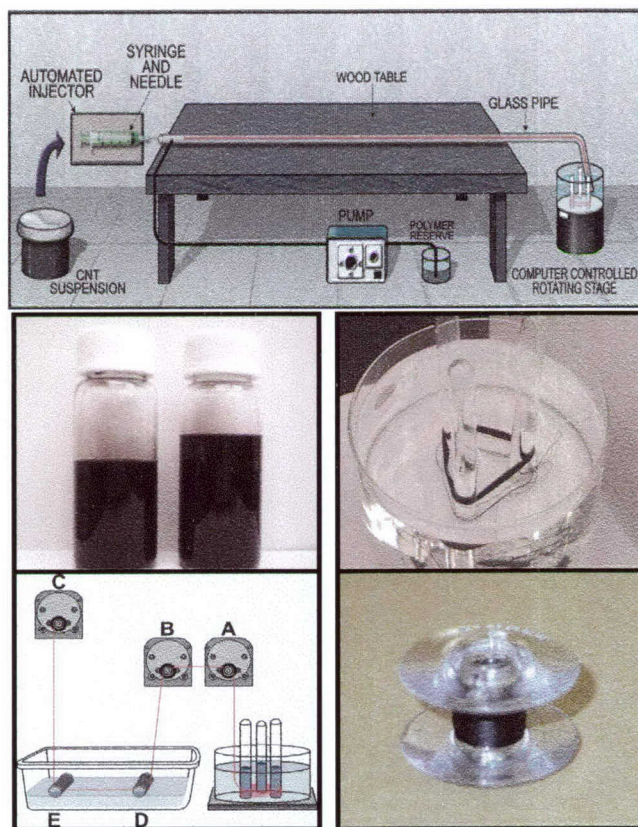

Figure 3.3.2. (A) Schematic of spinning apparatus (B) Stable SWNT suspension in a lithium dodecyl sulfate/dionized water solution. These suspensions are used as the "ink" for spinning nanotube gel fibers. (C) The ink in (B) is injected into the glass pipe (where the coagulation solution is coaxially flowing) to form the gel fiber, which travels along the glass pipe and is eventually collected on a rotating mandrel in a water bath. These pictured gel fibers act like a rubber, reversibly elongating up to 400% before breaking. (D) The gel is subsequently drawn out of the bath, passed over a series of godets and through an acetone washing bath during a drying process, and finally wound onto a spool (pictured, with a wound nanotube fiber).

the coagulation solution. As the polymer diffuses inwards and the layer thickens, pressure drives the water from the inside of this partially coagulated fiber, causing it to collapse into a thin ribbon (just like the collapse of a fire hose when the water is drained out).

During the spinning process, SWNTs are subjected to a minimal shear flow alignment in the injecting needle. Upon contact with the polymer solution, the outer surface of the spinning solution under goes further alignment by the uniaxial extensional flow generated by the shear stress produced by the difference in velocity of the polymer solution and spinning solution. The aligned outer region has a thickness of approximately 2 μm, while the inner region appears to be an isotropic mesh of polymer and nanotubes. Thus, it appears that nanotube alignment in the radial direction is determined by the diffusion rate of polymer into the core. Gel formation on the surface of the forming gel fiber is very fast, so the induced microstructural alignment is not lost due to thermal motion - thus preventing the nanotubes from relaxing into an isotropic randomized conformation.

The rotational relaxation time, t_r of the SWNTs can be estimated by considering the situation analogous to rigid rod polymers of length L and diameter d in a dilute solution of viscosity η_s at a temperature T. Correspondingly:

$$t_r = ((\pi \eta_s L^3)/(6 k_b T (\ln((L/d)) - \gamma)))$$ Equation 2

In Equation 2, k_b is Boltzmann's constant and γ is a universal constant (0.8). Thus the approximate relaxation time is well below 10 ms at room temperature. This is too fast to allow considerable gel formation before orientation is lost in the core of the fiber.

We can routinely make two hundred-meter long reels of continuous nanotube-polymer composite fiber at 70X the prior-art rate and achieve fiber strengths higher than 1.8 GPa. Our drawn nanotube fibers match the energy absorption capability of the highest performance spider silk up to the breaking strain of this silk (30%), and continue absorbing energy until they reach an energy-to-break of 570 J/g, as compared with 160 J/g for the spider silk, 50 J/g for Spectra fiber, 33 J/g for Kevlar fiber, and 1.5 J/g for prior-art solution-spun nanotube fibers. The density-normalized tensile strength of our nanotube composite fiber is presently 2.2X that of high performance steel wire and the density-normalized Young's modulus of the nanotube fiber and steel wire are identical.
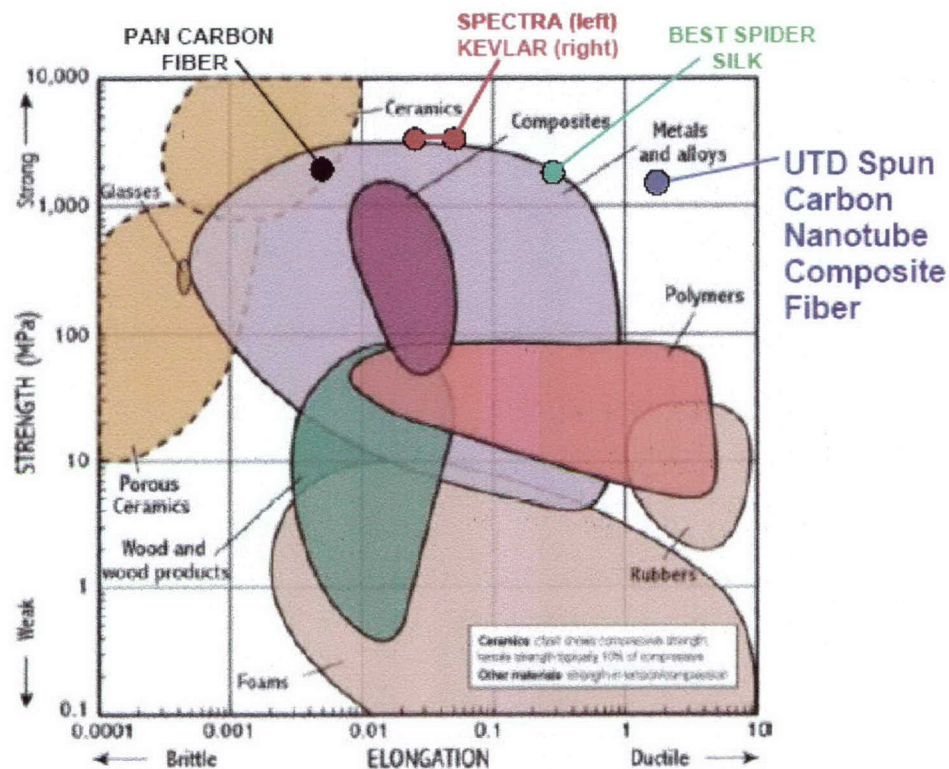
Figure 3.3.3. Comparison of the tensile strength and ultimate elongation for one of our carbon nanotube composite fibers with that of other materials. The combination of high draw and high tensile strength explains the very high toughness of the carbon nanotube composite fibers.

While we have extended the polymer solution to polymers other than polyvinyl alcohol, polyvinyl alcohol so far provides the highest strength, modulus, and toughness. Interestingly, however, the use of polyethylenimine in the aqueous coagulation solution provides spun polymer composite fibers that are hollow, and have an electrical conductivity (100 S/cm) that is about 50 X higher that for the polymer coagulation spun carbon nanotube/polyvinyl alcohol fibers.

Polymer-free Carbon Nanotube Fibers

We have also developed a technology which enables preparation of carbon nanotube assemblies (fibers, ribbons, ropes, films) free of any polymer binder. The prepared fibers exhibit record capacitance, good transport properties, and useful mechanical strength. The process is further referred to as a flocculation spinning process.

In our polymer free fiber spinning process, a narrow jet of nanotube dispersion is injected into flow of 37% hydrochloric acid, which at the point of injection causes aggregation and partial alignment of nanotubes. The acid acting as a flocculant aid efficiently suppresses the dispersing action of the surfactant promotes aggregation and provides support for a gel fiber forming in the liquid flow. Obtained gel fibers are then washed in aqueous solution of methanol in order to remove the flocculant aid. Finally fibers are pulled out of the wash bath, stretched over a sturdy frame and dried under tension so that low-density gel collates into a compact thin fibers formed by a dense nanotube network. Drying under tension provides additional alignment of nanotubes in the material.

Scanning electron microscopy (SEM) images of prepared fibers taken at low and high magnification are shown in Figure 3.3.4. Fibers typically have diameter of 10-50 µm; their surface reveals some degree of macroscopic alignment and fracture exhibits fine well resolved SWNT network.
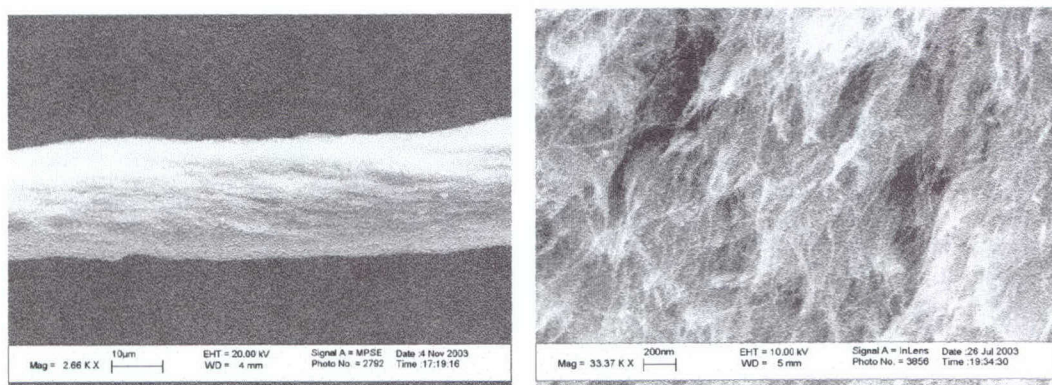

Figure 3.3.4. SEM images of fibers taken at low (left) and high (right) magnifications. Some degree of macroscopic alignment and fine well resolved CNT network can be seen.

The flocculation process normally results in gel fibers having ribbon-like texture. Probably van der Waals interaction between nanotubes promoted by the surfactant neutralization and accompanied by rapid nanotube aggregation creates an external pressure that collapses injected dispersion into a dense SWNT layer. The structure upon removing the solvent, drawing and drying develop shape resembling hollow macrotube (O ring-like cross-section), folded ribbon (S- and Z-like shape) or a rod with rectangular

or approximately round cross-section (Figure 3.3.5). The latter originates from a narrow ribbon gel precursor. Hollow fibers can be filled with different constituents such as ionic liquids that can be thermally or electrochemically polymerized forming a structure needed for supercapacitor applications.
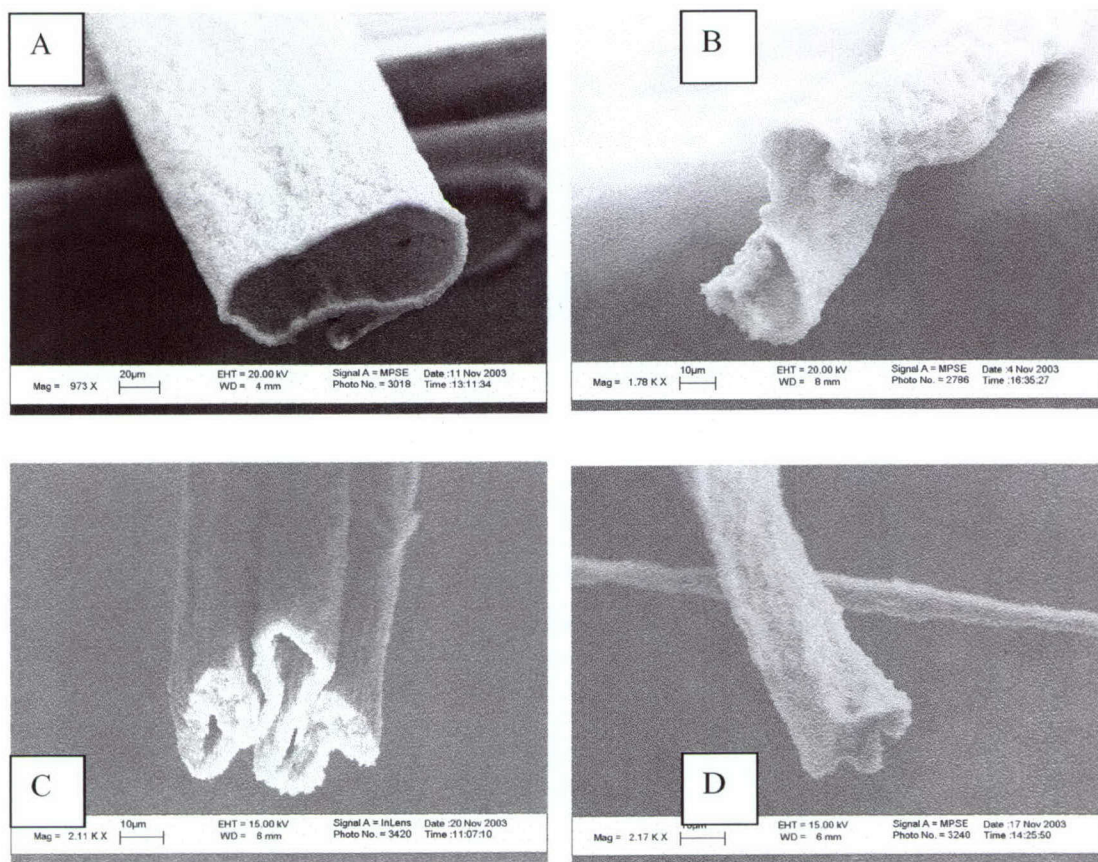

Figure 3.3.5. Cross-sections of as-spun fibers: hollow O-ring (A), S-like (B), folded ribbon(C), rectangular (D).

Raman measurements of as-spun fibers show that the spectra depend little on the type of flocculant aid used for fiber spinning; they closely resemble the spectrum of pristine nanotubes. Significant orientational dependence of Raman peak intensity was observed in polarized measurements. It is known for orientated nanotube fibers that the Raman intensity in VV configuration (excitation and detection in the same polarization plane) for the tangential mode (G-line at ~1580 cm-1 for HiPco nanotubes) decreases continuously when the angle between nanotube axis and light polarization increases. The intensity ratio

for polarizations of light parallel and perpendicular to the fiber axis, which would show substantial value if nanotubes in fiber are aligned, was obtained by sampling multiple locations on fiber and calculating the average. In the vicinity of G line the ratio is equal to 5.2, which corresponds to a high degree of nanotube alignment and is consistent with our SEM observations.

Sections of fiber were tested with an Instron 5848 Micro Tester in tensile geometry, their weight was determined with a microbalance. For fibers having shape of hollow macrotube and folded ribbon precise determination of cross-sectional area meets significant difficulties. For this reason the measurements of tensile strength and Young's modules were performed on weight per length basis. Recorded force was normalized by weight per fiber length so that specific values for stress and Young's modulus are reported in units MPa/(g/cm3) and GPa/(g/cm3), respectively. The data obtained are collected in Table.3.3.1. These values are consistent with early measurements of PVA-based CNT fibers and exceed those for buckypaper. Although much smaller than for individual nanotubes, the values correspond to unbound CNT assemblies and can be significantly improved by crosslinking.

Table 3.3.1. Properties of as prepared polymer-free SWNT fibers.

Young Modulus (GPa/g/cm3)	12
Tensile Strength (MPa/g/cm3)	65
Elongation to Break (%)	1-4
Electrical Conductivity (S/cm)	140
Specific Capacitance (F/g)	100

The temperature dependencies of electrical conductivity were obtained by the four-probe method in the range 80-300 K. These fibers exhibit semiconducting type behavior, typically providing a conductivity decrease by about 35% with decreasing temperature in this temperature range. The room temperature electrical conductivities are approximately 15 and 140 S/cm for as-spun and annealed fibers, respectively.

The specific capacitance of polymer free fibers was measured using a three-electrode cell with carbon felt as a counter electrode and Ag/Ag+ as reference electrode. The fiber was cycled in ethylmethylimidazolium imide ionic liquid using different scan rates and potential ranges. It was found that the capacitance, normalized by the weight of the sample, was approximately 48 and 100 F/g for as-spun and annealed fibers, respectively. These very large values of capacitance can be explained by the high surface area of the SWNT network and by the accessibility of the electrolyte to this network. These capacitances are substantially higher than the capacitance of buckypaper and exceed those recoded by us for CNT fibers of other types that are underivatized and not intercalated.

The electro-mechanical response of polymer free fibers was measured using custom made force transducer operating in an isometric mode. The measurements were carried out at room temperature in aqueous and organic electrolytes; square-wave potential of variable amplitude was applied with a potentiostat. We found that the maximum isometric stress generated by fiber actuators can be as large as 7 MPa at 1 V. This value approaches the best result recorded by us on CNT fibers of other types (26 MPa).

By adjusting the injection rate of the nanotube dispersion in flocculating liquid, the diameter of spinneret opening and the velocity of coagulating liquid, the shear force imposed on the nanotubes can be adjusted. It is preferred that the inner diameter of spinneret tube is less than 0.23" (21G), most preferably less than 0.0095" (25G). This small diameter and shear flow of nanotube dispersion in coagulating solution aid in aligning the carbon nanotubes in the direction of the flow. The implementation of extra thin spinneret tubes in our apparatus enables spinning of CNT fibers of about 10 µm in diameter.

As a final step, after the gel fiber is dried, we typically anneal the spun fiber at elevated temperature in inert atmosphere or vacuum. The post treatment aims at graphitization of any organic constituents that may be present in the fiber and development of carbon-

carbon contacts in nanotube junctions. This annealing was typically accomplished at about 1000 °C. However, the following experiment shows that the nanotube fibers can survive to above 2000 °C, albeit likely with a degree of coalescence of single walled nanotubes into multiwalled nanotubes.

In our experiments the fiber was attached to a special holder and heated with electric current in oxygen-free environment. The application of voltage caused intense thermal emission (bright glow) from the fiber (Figure 3.3.5).
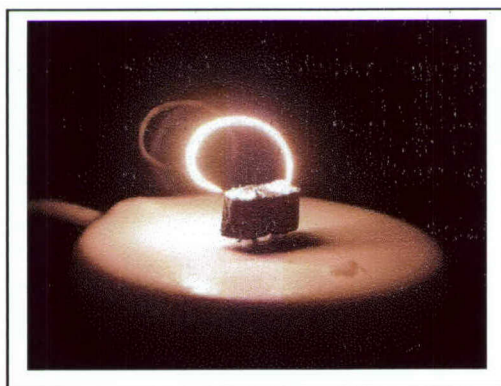
Figure 3.3.5. A polymer-free coagulation-spun SWNT fiber heated to incandescence.

Significant improvement of mechanical properties of the material at the post spinning step has also been obtained by using various polymer binders. Prepared fibers were soaked in 5% aqueous solution of poly(vinyl alcohol) (PVA), and some other polymers such as polystyrene and ceraset. The ceraset-treated fiber was annealed at 200 C for 3 hours. Sections of fibers were then tested with a Instron 5848 Micro Tester in tensile geometry; their weight was determined with a microbalance. The largest improvement in mechanical properties was observed for PVA-infiltrated material. Typical numbers for PVA treated fibers are presented in Table 3.3.2. The study shows that post spinning treatment can improve mechanical properties of fibers by factor 5-7 and possibly more upon optimization of treatment conditions.

Table 3.3.2. Mechanical Properties of Fibers Soaked in Poly(vinyl alcohol)

Run Number	First	Second	Third
Young Modulus (GPa/g/cm3)	5.5	10.3	13.2
Tensile Strength (MPa/g/cm3)	74	261	368
Elongation to Break (%)	185	43	9

In our most recent work, we have significantly improved the density-normalized mechanical properties of these polyvinyl alcohol infiltrated fibers, thereby achieving a true tensile strength of 770 MPa/(g/cm^3), a Young's modulus of 8.9 GPa/(g/cm^3), a strain-to-failure of 30 % and a fiber toughness of 137 J/g. While lower in strength and toughness than the record values achieved for nanotube fibers that are spun by the polyvinyl alcohol coagulant process, this toughness exceeds that of commercial fibers used for antiballistic protection and is close to the maximum toughness observed for spider silk.

Welding of Carbon Nanotube Assemblies

The objective of the present task was to weld the carbon nanotube structures to create mechanically stable and stronger structures for electrochemical actuation. This objective was attained by welding carbon nanotube structures with polymer derived ceramic (PDC), silicon carbonitride (SiCN). Liquid polymeric precursor of PDC-SiCN wets the nanotube structure very nicely because the interfacial energies and the curvatures are favorable. The precursor infiltrated nanotube structure is then pyrolyzed to convert the polymer into high temperature ceramic. High resolution TEM indicates the pervasive presence of the SiCN ceramic covering, as far as we can tell, the entire CNT structure. However, this uniform ceramic coating does not deteriorate the capacitance and actuation of the nanotubes. The welded structure practically eliminates the creep of the nanotube structures and makes them mechanically stiffer. However, the thermally annealed nanotubes fibers are quite brittle, and this brittleness is retained and likely enhanced by using this welding method.

Carbon nanotube structures such as papers and fibers are held together either by Van der Waal's forces or polymeric binders. These structures exhibit extensive creep during electrochemical actuation due to mechanical sliding between adjacent nanotubes. Furthermore, the structures exhibit low modulus, which adversely affects their stress generating capability. If by some means these nanotubes can be welded rigidly, it can solve both these problems. Nanotube papers are found to be easily wetted by liquids, possibly as a result of the small diameters of the nanotubes. Good welding of the nanotubes can be achieved therefore by using ceramic-precursor liquid as a starting material and later converting it into solid in situ. These ceramics are known as polymer-derived ceramics.

Polymer derived ceramics are a new class of materials developed from organo-elemental precursors. The most commonly studied materials among this class are silicon-based systems such as Si-C-N and Si-C-O. Both systems have liquid precursors that can be cross-linked and shaped as polymers, which can then be converted into ceramics by controlled pyrolysis. In the present investigation the SiCN based system was used to weld the nanotube papers. The influence of welding on the electrochemical properties was studied.

The nanotube structures were made at the University of Colorado using purified HiPco tubes from Carbon Nanotechnologies Inc. (Houston, TX). The tubes were dispersed in water using Triton-X100 non-ionic surfactant from Alfa Aesar (Chicago, IL) and ultrasonication. The dispersion with concentration of (50 mg CNT / L of DI water) was then filtered through 5 micron Teflon filter paper from Millipore Corp. (Bedford, MA). The nanotubes were deposited on the filter paper. The tubes were washed with methanol and water to remove as much surfactant as possible. The tubes deposited on the filter were then pulled off as a "paper". This nanotube paper was first annealed at 1100°C in flowing ultra high purity argon in an alumina muffle-tube furnace to burn off any remaining surfactant. Further experiments were carried out in two parts. First, the annealed paper obtained after this process was used to study the properties of pure nanotube paper. Second, the paper was welded using PDC route, as described below.

Commercially available silazane based precursor polyureamethylvinylsilazane – CerasetTM-SN (Kion Corporation, Columbus, OH) was used as the welding agent for fabricating welded nanotube structures. Varied concentrations of the Ceraset (2-10% by volume) in acetone were used to infiltrate the nanotube papers to obtain different amount of welding after pyrolysis. About 0.2 ml of solution was used to infiltrate 40 μm thick nanotube paper. For thinner nanotube paper, a proportionately lower amount of liquid was used. The paper was kept in air for about 15 minutes to let all the acetone evaporate and was then placed in the an alumina muffle-tube furnace with flowing argon for pyrolysis at 1100 °C.

The properties of welded and unwelded samples were studied in various ways. (a) They were burned in a thermo gravimetric analyzer (TGA – STA 409 from Netzsch Instruments, Paoli, PA) in flowing air to determine the amount of welding agent (by comparing the residue of the welded and unwelded paper). (b) Specific surface area measurements were made using a BET analyzer ASAP 2010 from Micromeritics Inc. (Norcross, GA). (c) The electrochemical capacitance was measured for each batch of welded and unwelded paper using a Potentiostat/Galvanostat model 173 and programmer model 175, both from EG&G PARC (Oak Ridge, TN). The potentiostat and programmer were used together to obtain cyclic voltammetry data at various scan rates, recorded using a PC equipped with A/D converter and Labview Software from National Instruments (Austin, TX). Ag/AgCl reference electrodes were used for electrochemical measurements.

The mechanical properties were characterized using a miniature home-built tensile tester, in constant load and constant strain rate modes, and from room temperature to up to 320 °C in air. Nanotube paper was cut in strips and mounted on alumina pull rods with help of alumina cement cured at 320°C. The load was measured using an inline load cell and the displacement was measured using an LVDT. The creep experiments were done in a constant load creep-testing machine. The sample is mounted between a stationary outer

tube and movable inside rod. The displacement was measured using LVDT mounted on the inside rod.

Electrochemical-actuation was characterized using a specially designed setup, where actuation strain was measured directly under constant stress. It consists of the assembly of graphite pull rods with specimen, LVDT core and constant weight submerged in the electrolyte. The displacement of the specimen is measured using the LVDT. Computerized data acquisition system is used to collect the data for voltage and current supplied and resulting actuation strain.

Microstructural characterization was done in collaboration with Max Planck Institute, Stuttgart, Germany. High resolution TEM, with chemical mapping was performed by them to characterize the structure and geometry of the weldments. Scanning electron Microscopy was performed periodically at the University of Colorado to investigate the structure of the papers made.

The processing of the nanotube paper required careful dispersion and filtration of the tubes obtained from Carbon Nanotechnologies Inc. The tubes were supplied in form of dry material, called Bucky Pearls, to facilitate ease in handling and prevent the nanotubes from flying everywhere. The amount of surfactant and ultrasonication time to disperse the pearls varied from batch to batch of the nanotube supplies. Depending on the size of the tubes in the batch it is necessary to change the filter paper since with very fine tubes, the filter paper gets clogged easily and then filtration takes very long time. The amount of weldment in the paper was analyzed by burning the nanotube in air in TGA. The residual weight of the paper after burning the nanotube was used to calculate the amount of welding agent. This welding agent varied from 10 – 50%, depending on the concentration of the precursor solution used to infiltrate the paper.

Figure **3.3.6** shows the TGA curves for the unwelded and welded nanotube papers with different amount of weldments.
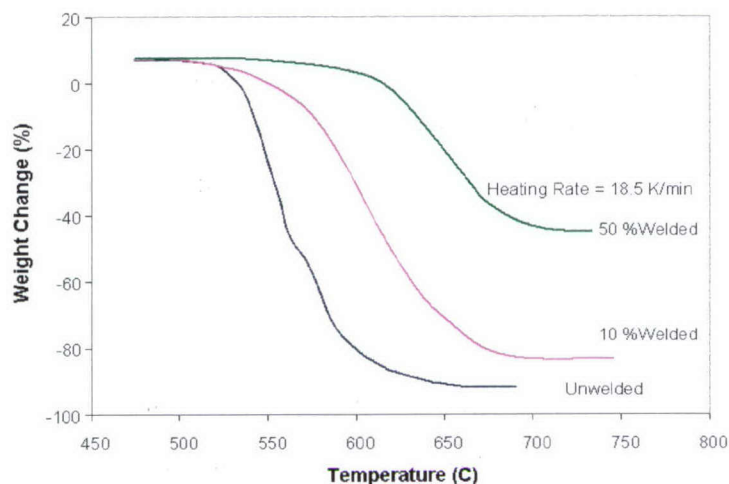
Figure 3.3.6. TGA of unwelded and welded nanotube papers in 0.3 atm oxygen to determine the amount of welding agent in the welded nanotube papers.

Figure 3.3.7 shows the HRTEM micrograph photos of the carbon nanotubes welded with polymer precursor derived silicon carbonitride. Detailed TEM investigation of welded nanotube papers has shown pervasive welding of the nanotubes with silicon carbonitride, in the nanotube papers. Energy filtered imaging of the welded nanotube specimens show the presence of silicon throughout the surface of the nanotube bundle. The pervasive coating confirms the uniform wetting of the nanotubes by the precursor. The welding is also evident from the fact that the BET surface area of the welded nanotube papers is lowered by 10% from 544 m^2/gm for unwelded paper to 490 m^2/gm.
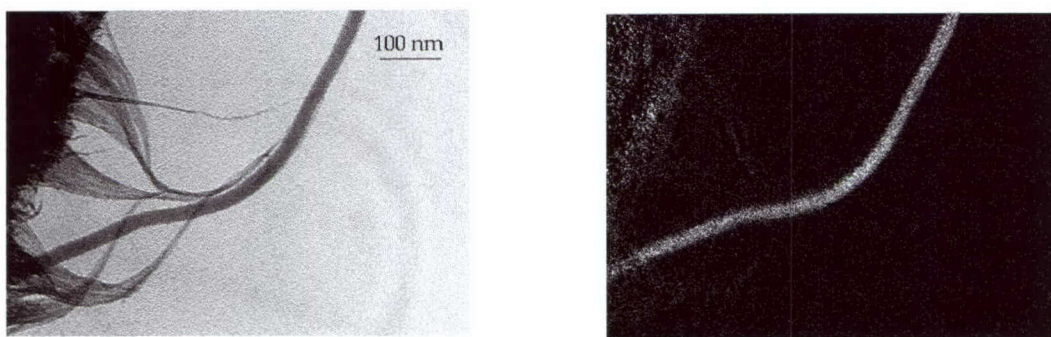
Figure 3.3.7. The TEM micrograph on the left is a bright field image of a CNT bundle. The micrograph on the right is a dark field "chemical image" centered on the silicon filter, showing a uniform coverage with silicon, or SiCN

The effect of welding on the creep of unwelded and welded nanotube papers was studied using a constant load creep testing and constant strain rate creep testing. Figure 3.3.8

shows the creep of the unwelded and welded nanotube paper under constant stress at 320 °C in air. As can be seen the unwelded nanotube paper exhibits extensive creep, whereas the creep is almost completely suppressed in case of the welded nanotube paper.

Creep in CNTs at 320°C in Air
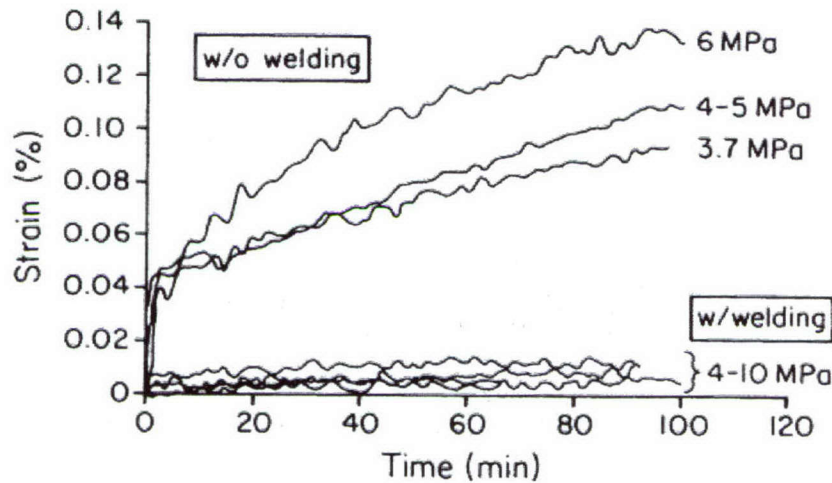
Figure 3.3.8. Constant Stress creep curves for the welded and unwelded nanotube papers.

It is also worthy to note that the modulus for the SiCN welded paper is insensitive to the applied strain rate whereas the unwelded paper is strongly influenced by the strain rate. Note that the ceramic introduces stronger bonds between the tubes and eliminates the inter-tube sliding, resulting in time and temperature independent modulus.

The effect of strain rate and temperature on the modulus was studied for three types of specimens: (a) CNT paper containing surfactant, (b) annealed paper where the surfactant was removed by annealing but which was not welded, and (c) annealed paper after welding. These results are given in Figure 3.3.9 below. The paper containing surfactants show a low modulus, which is strain rate dependent.
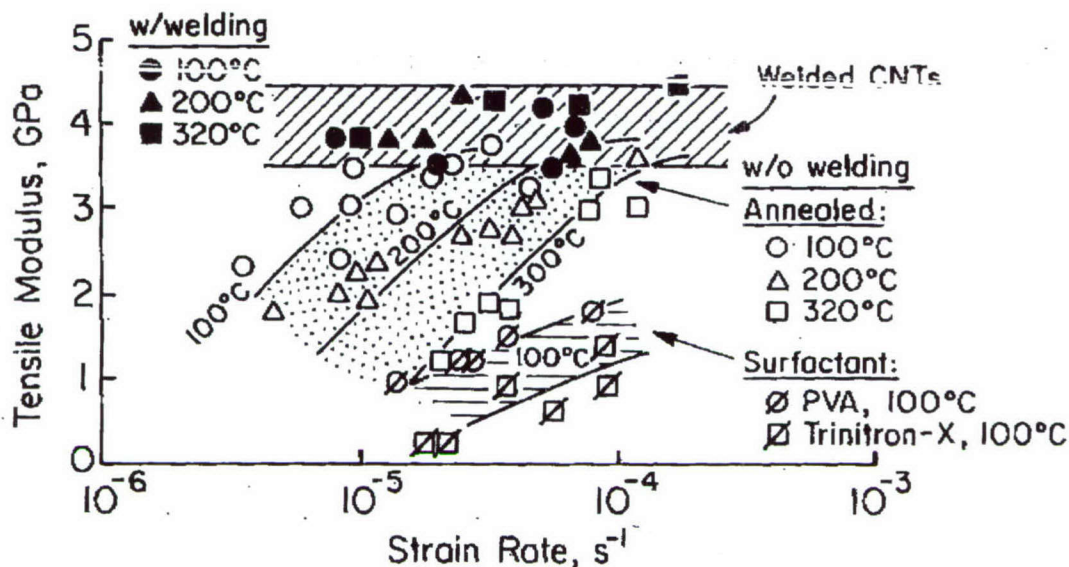
Figure 3.3.9. The strain rate and temperature dependence of the modulus for welded (solid points) and unwelded (open points) carbon nanotube structures.

The annealed, unwelded samples show a higher modulus than for unannealed samples, although in both cases this modulus is strain-rate dependent. However, the welded samples show the highest modulus, and this modulus is strain-rate independent. It is interesting to note that these strain-rate results for the unwelded paper have similar appearance to those for polymers having a glass-transition temperature.

The elastic modulus of welded carbon nanotube paper is far less that would have been expected simply from a volume fraction argument, that is, the modulus being expected to be equal to the volume fraction of the nanotubes times the in-plane modulus of graphene sheets. For example if the graphene modulus is 1000 GPa then the "ideal" modulus of the paper is expected to be about 100 GPa since the volume fraction is approximately 10%. Instead the measured value of the modulus is nearly an order of magnitude lower. This difference is explained by theorizing that the modulus of the paper is determined not by the longitudinal stretching of the carbon nanotubes, but rather by the flexing or bending of the nanotubes between the adjacent junctions. This flexing action is modeled in terms of a cellular structure sketched on the left in Figure 3.3.10 below.
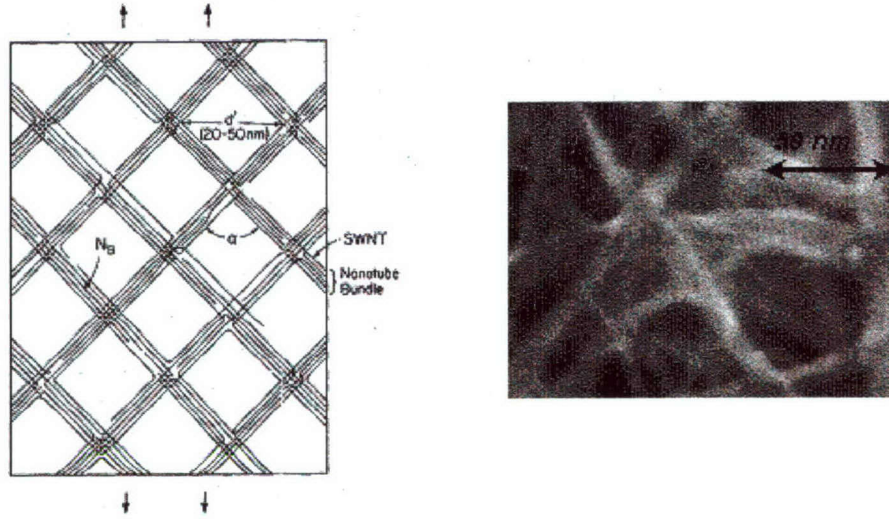
Figure 3.3.10. The simplified cellular structure for the nanotube paper and typical SEM for welded nanotube paper to approximate the cell size and the nanotube bundle size.

During tensile testing this cellular structure supports the applied load by flexural deformation of the nanotube bundles. The model considers two extreme possibilities: 1) there is no welding or interaction between the tubes in the bundle, that is, there is no inter-tube load transfer and 2) there is ideal welding between the tubes. The first possibility gives the lower bound of the modulus and the second limit gives the upper bound. The ideal nanotube modulus is assumed to be 1000 GPa and the density of the nanotube is taken as 2 gm/cm^3 for the present calculations. These bounds are given by the following equations.

The upper bound of the paper modulus is given by

$$E_{PAPER} = \frac{\pi^2}{2.5} E_{SWNT} N_B^2 \left(\frac{a_{SWNT}}{d'} \right)^2$$

and the lower bound of the paper modulus is given by

$$E_{PAPER} = \frac{\pi^2}{10} E_{SWNT} N_B \left(\frac{a_{SWNT}}{d'} \right)^2$$

where N_B is the number of tubes in bundle, a SWNT is the diameter of single nanotube and d' is the cell size. Taking the proper numbers from the micrograph we estimate the lower bound for the modulus as 0.25 GPa, and the upper bound to be 125 GPa. The experimental values of the modulus for the welded nanotubes is in the 4-5 GPa range which is about 20 times greater than the lower bound but, at the same time about 20 times smaller than the upper bound. The difference with respect to the upper bound suggests that the welding between the nanotubes is not ideally rigid but it is controlled by the modulus of the ceramic (SiCN), and that the thickness of the ceramic bond is comparable to the wall-thickness of the single wall carbon nanotubes. Note that the modulus of SiCN is approximately 150 MPa, while the modulus of carbon nanotubes may be as high as 1000 GPa; therefore even a small layer of SiCN between the nanotubes can significantly lower the bending stiffness of the bundles.

The effect of welding on the electrochemical capacitance and actuation were evaluated. The capacitance was measured using the cyclic voltammetry in 1M NaCl solution in water. The welding reduces the capacitance, since it also reduces the specific surface area of the paper from 544 m^2/gm for unwelded paper to 490 m^2/gm for lightly welded paper to 300 m^2/gm for heavily welded nanotube paper.

The capacitance is related to the electromechanical actuation that can be obtained because the extent of actuation depends on how much charge can be injected into the nanotube structure via the electrolytic capacitance. Figure 3.3.11 shows the comparison between the actuation strain of the welded and unwelded papers measured using the actuation setup fabricated at the University of Colorado. The actuation strain for the welded structure is at least as large as for the unwelded structure. Furthermore the increase in the amount of welding does not deteriorate the actuation response of the nanotube papers. A number of batches of welded and unwelded papers were characterized. The welded papers show strain between 0.07-0.1% for an applied voltage cycle of 0-(-2) V at 0.125 Hz., whereas unwelded papers show strain between 0.04-0.1% at same voltage cycle. It appears that the welding reduces variability in the actuation strain without reducing the magnitude of the strain.
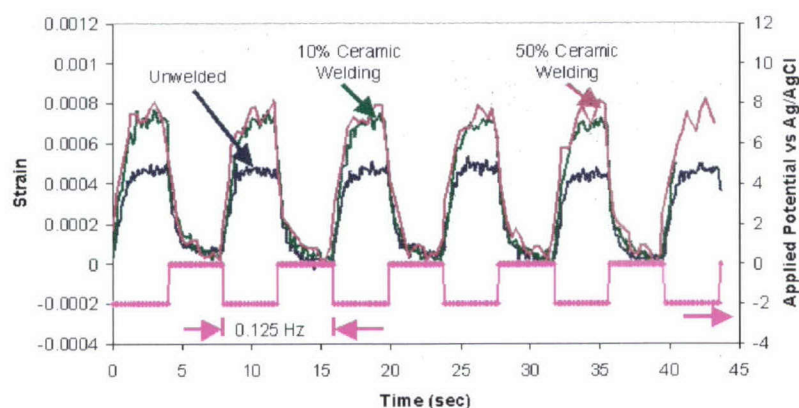
Figure 3.3.11. Actuation response of the welded and unwelded purified HiPco nanotube paper.

Figure 3.3.12 shows the actuation strain as a function of the applied potential. The potential was pulsated between 0 to the voltage plotted on the abscissa. The strain response is lower in the positive voltage range, which is attributed to extensive electrolysis. The strain to voltage response is approaches linearity in the negative voltage range, suggesting a direct correlation with the injected charge.
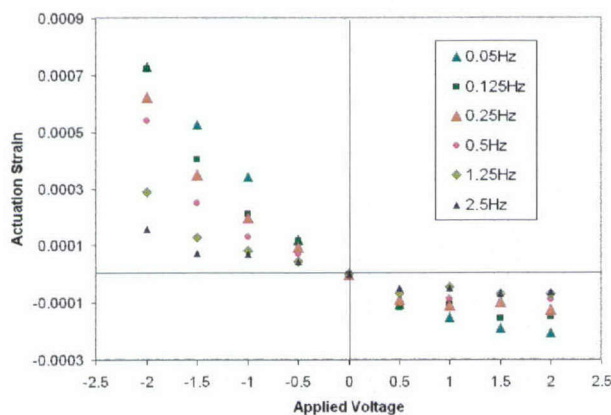
Figure 3.3.12. Strain as a function of the applied voltage for 10% welded NTP.

The actuation strain remains constant at the lower frequencies. When the frequency is high the specimen does not get enough time to charge completely and thereby the exhibited strain is lower. The frequency at which the actuation strain begins to decay is called the transition frequency. The transition frequency is similar, about 0.1 Hz for both the welded and the unwelded specimens.

Equivalent Electrical Circuit Model

An equivalent electrical circuit of the experimental setup to measure electrochemical actuation is shown in Figure 3.3.13 V_{out} is the electrical equivalent of the mechanical actuation. RE indicates the electrical resistive path from the potentiostat to the specimen and the counter electrode. RM is the electrical resistance equivalent to the creep relaxation of the specimen. RF is the resistance equivalent to the friction between the load train including the specimen and the electrolyte. The ratio of output voltage to the input voltage is equivalent to the actuation strain of the carbon nanotube specimen. The present system using 1M NaCl solution has very low viscosity and very small RF, which can be neglected. The resulting actuation strain can be given by

$$\frac{V_{out}}{V_{in}} = \frac{R_M}{R_E + R_M + iwCR_E R_M}$$
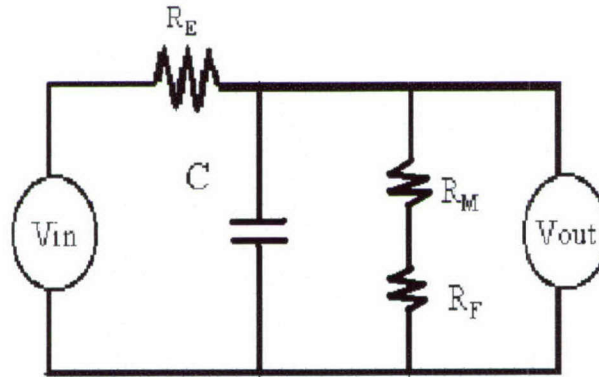
Figure 3.3.13. An equivalent electrical circuit for the setup shown in Fig. 3.3.1(b).

The time constants due to two resistive paths are

$$\tau_E = R_E C; \tau_M = R_M C$$

which gives

$$\frac{V_{out}}{V_{in}} = \frac{\tau_M}{\tau_E + \tau_M + iw\tau_E \tau_M}$$

The creep relaxation time $\tau_M >> \tau_E$ which results in

$$\frac{V_{out}}{V_{in}} = \frac{1}{1 + iw\tau_E}$$
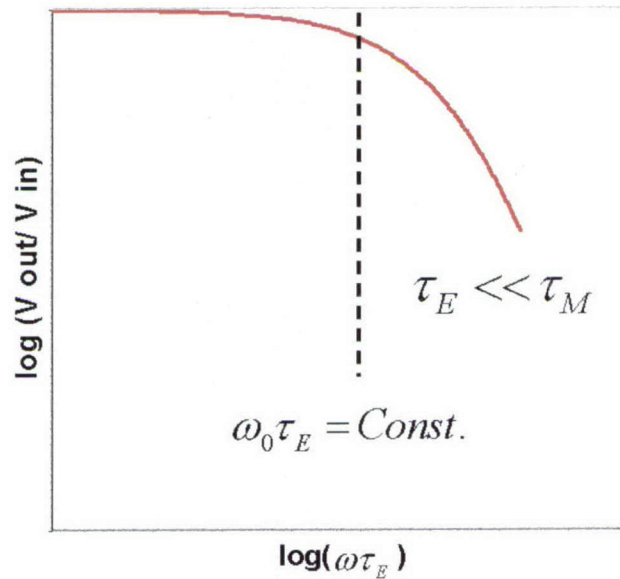
Figure 3.3.14. Plot of the actuation strain from equivalent electrical circuit in Fig. 3.3.14.

Work Density Per Cycle

The work density per cycle (per unit volume) is equal to $1/2Y\varepsilon_m^2$, where Y is Young's modulus, ε_m is maximum strain. As shown in Table 3.3.3, the work density in the welded actuators was nearly 10X higher than in unwelded CNT actuators.

Table 3.3.3. Volumetric work density of the two kinds of actuators.

	CNT actuator	SiCN welded CNT actuator
ε_m	0.04-0.1%	0.075-0.1%
Y	~1.2 GPa	~4 Gpa
$1/2 Y \varepsilon_m^2$	$(0.9 – 6) \times 10\text{-}7$	$(10.6 – 200) \times 10\text{-}7$

In summary, the polymer derived ceramic SiCN can be successfully used to weld carbon nanotube papers, thereby improving their mechanical properties and eliminating the creep exhibited by the unwelded paper. Even though the welding covers the nanotubes completely, the structure still retains the giant electrochemical capacitance after welding and exhibits electrochemical actuation. Welding of nanotube papers reduces the variability in actuation strain and leads to comparable or higher strain as in unwelded specimen, even when the welded paper contains 50% ceramic by weight. A possible implication of this result is that the SiCN used to weld the carbon nanotubes may itself exhibit carbon nanotube-like behavior. Recent Raman characterization of intrinsic SiCN has shown the presence of long-range graphene structures; this is an exciting development pointing towards an alternative method for the fabrication of structures, which are akin to carbon nanotubes.

3.4 ACTUATING MULTIFUNCTIONAL STRUCTURES (task leader, Geoff Spinks)

High Performance Carbon Nanotube Macro Actuators

The program aims in this area were to assemble macroscopic nanotube structures that facilitated significant improvements in key actuator performance: strain rate, stress generated and lifetime. The improved actuators were also to be constructed into multifunctional devices using solid-state electrolytes. Much of the materials development for high performance actuators is described in Section 3.2, where the characterization of new structures included an assessment of actuation performance. The nanotube assemblies prepared in the development of improved actuators include:

- Wet spun fibers tested in as-received condition and treated to remove polymer binder
- Welded nanotube papers
- Nanotube papers tested in ionic liquid electrolytes
- Nanotube papers prepared from various sources

The main conclusions for each of these structures that relate to the actuator goals are presented in this section.

High Strain Rate Actuators

A first estimate of the variables that influence actuation rate ($\partial \varepsilon / \partial t$) is given by

$$\frac{\partial \varepsilon}{\partial t} = \frac{\partial \varepsilon}{\partial y} \frac{\partial y}{\partial t} ,$$

where y is the charge injected so that $\partial y / \partial t$ is the current. The current decay for a step change in voltage (E) is estimated by

$$i = \frac{E}{R_s} e^{-t/RC} ,$$

where R_s is the solution resistance, R is the total cell resistance and C is the cell capacitance. The two equations give an estimate of the strain rate:

$$\frac{\partial \varepsilon}{\partial t} = \frac{\partial \varepsilon}{\partial y} \frac{E}{R_s} e^{-t/RC} .$$

The charge/strain coefficient $\partial \varepsilon / \partial y$ is fixed by the nature of the nanotube assembly and is likely influenced by the type of nanotubes, the bonding between nanotubes and the degree of bundling of nanotubes. Many attempts were made throughout the program to optimize these structures so as to improve actuation performance. Although welding had benefits in terms of actuator cycle life, most other factors had little effect on the strain to charge ratio. Figure 3.4.1 shows the response from carbon nanotube sheets.
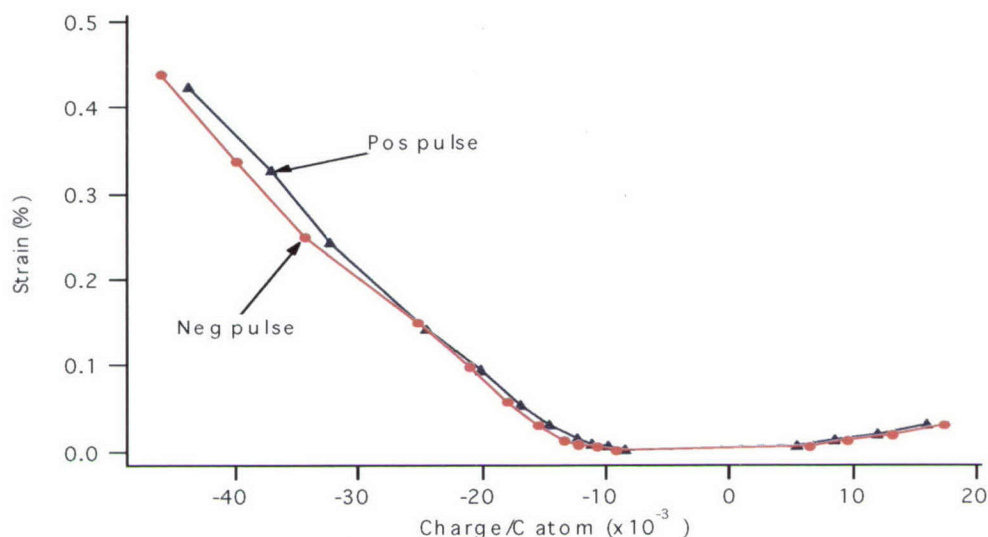
Figure 3.4.1. Strain-charge curves for a Carbolex CNT sheet constructed using data from the positive-going potential pulses or from the negative-going pulses, load 20 mN.

A second approach investigated to increase nanotube strain rate was to increase the rate of charge injection. There are two methods for achieving a higher rate of charge injection:

- Minimizing sheet/fiber thickness to reduce the effective solution resistance within the porous NT assembly
- Use resistance compensation methods to overcome the solution resistance without degrading the electrolyte.

The first method was not successful, since thin fibers prepared generally showed smaller actuation strains (and therefore strain rates) compared with nanotube sheets. The reason for the smaller actuation strain in fibers was mainly related to the effect of the polymer binder used in preparing the fibers. The binder showed poor mechanical strength when immersed in electrolytes and caused excessive creep (often leading to rupture) that masked the reversible actuation performance. Many efforts were made to remove the polymer binder and these generally produced very brittle fibers that were very difficult to test for actuation.
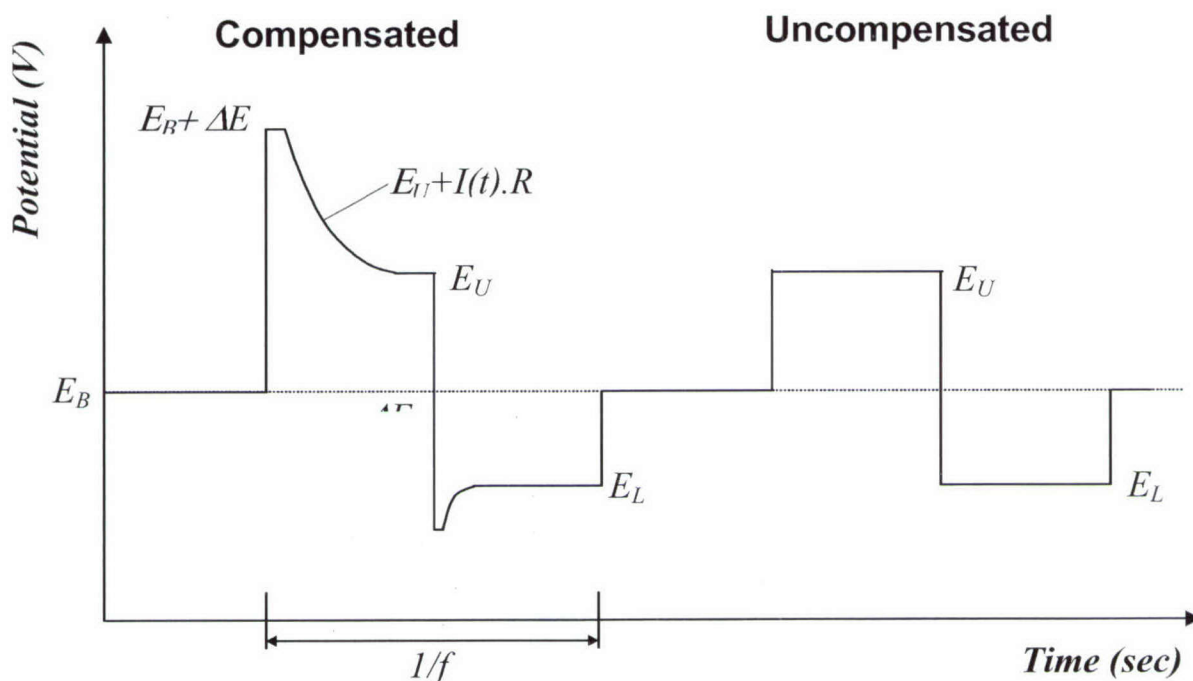
Figure 3.4.2. Example of resistance compensation techniques where the potential applied to the sample (with respect to a reference electrode) is corrected to account for the error caused by the electrolyte resistance ($I(t).R$) between the sample and the reference electrode.

Resistance compensation allows for faster charging of an electrode by applying a large cell potential for a short time (Figure 3.4.2). For a potentiostated three-electrode system an error is always present due to the difference in potential between the sample and the reference electrode. The potential difference is $I.R$ where I is the current passing between the sample and counter electrode and R is the electrolyte resistance between the sample and reference electrode. Resistance compensation techniques correct for this error by adjusting the sample potential (E) with respect to the reference potential such that:

$$E(t) = E_U + I(t).R$$

where E_U is the desired (upper) potential. An example of a shaped potential pulse using resistance compensation is shown in Figure 3.4.2. An uncompensated pulse is also shown for comparison.

55

Initial studies using the resistance compensation technique produced a five fold increase in charging rate and an increase in actuation rate of three fold to 0.9%/s. A simpler method of achieving the resistance compensation is to use large two-electrode cell voltages. Application of short pulses of high voltage (eg. 5 V) between the sample and the auxiliary electrode can effect rapid charging of the double layer and prevent electrolyte decomposition if the voltage is applied only in short pulses. The results of short (0.5 s) pulses of –5V and +0.5V for a carbon nanotube strip in acetonitrile electrolyte are shown in Figure 3.4.3. Peak strain rates of 1.3%/s (expansion) and 1.4%/s (contraction) are achieved. These values exceeded our first year goal of 1%/s.
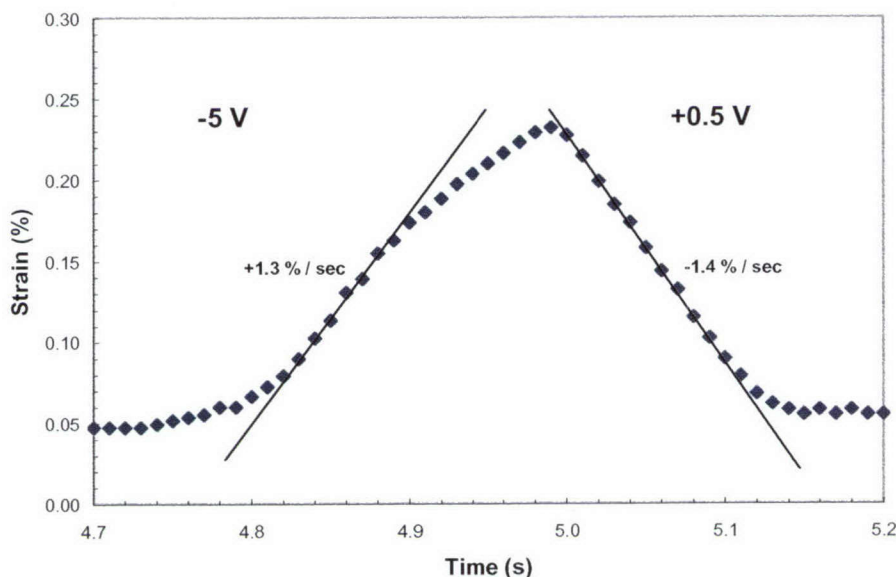
Figure 3.4.3. Actuator strain achieved using voltage pulses in a two-electrode cell using the cell potentials as shown and a pulse time of 0.5 s.

The above results were obtained during isotonic testing at constant force, but much faster responses were obtained in isometric testing. The results shown in Figure 3.4.4 demonstrate high rates of stress change are possible using resistance compensation methods for isometric actuator measurements. The maximum stress rate generated was 160 MPa/s, which corresponds to an apparent strain rate of 19%/s using the measured modulus of the nanotube sheet. This result exceeds the pre-program best results (23

MPa/s and 0.3%/s) and shows that nanotube sheets can generate 6 times the stress generated by natural muscle in only 6 msec. The result also exceeds our ambitious second year goal (5%/s) by almost a factor of four.
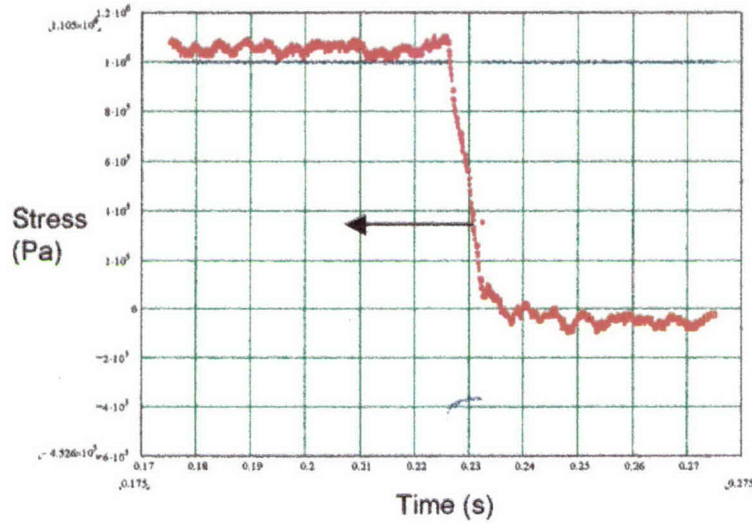

Figure 3.4.4. Stress response for NT paper stimulated by a short voltage pulse using resistance compensation technique (courtesy J. Madden, MIT).

High Stress Actuators

The stress generated by an actuator material (σ_a) can be estimated from the product of the actuator strain (ε_a) and the material's Young's modulus (Y).

$$\sigma_a \approx \varepsilon_a Y$$

Given that the actuator strain reported for nanotube assemblies (filtered sheets) of 1% is close to the predicted maximum strain, the actuator stress of nanotubes can only be increased by increasing the Young's modulus. Figure 3.4.5 shows how the actuation stress changes with increasing modulus for both 1% actuation strain and 0.2% actuation strain. The latter is more typical of nanotube assemblies and it can be seen that a modulus of 250 GPa is required to produce 500 MPa stress (Year 2 goal). However, the maximum stress generated can be limited by the breaking strength (UTS) of the material and the following approximate limit is assumed:

$$\sigma_a \approx 0.5 UTS$$

Increases in Y for nanotube assemblies have been achieved through fiber spinning with modulus and strength values of 80 GPa and 1.6 GPa, respectively. These materials

would be expected to generate 160 MPa stress at an actuation strain of 0.2%. Unfortunately, the PVA binder in these fibers disintegrated in electrolyte so that useful actuation was not achieved. Instead, it was possible to eliminate the PVA by thermal annealing to give a fiber that could be tested in electrolyte. Continuously spun NT fibers obtained from the UTD process were tested in acetonitrile electrolyte and found to generate 19 MPa in isometric operation (Fig. 3.4.6). This stress is almost 100 times higher than for un-oriented sheet and reflects the higher elastic modulus in the fiber direction. Many other attempts were made to modify the fibers through post spinning treatments or by modifications to the spinning process. Unfortunately, none of these modifications produced improved stress generation during actuation testing.
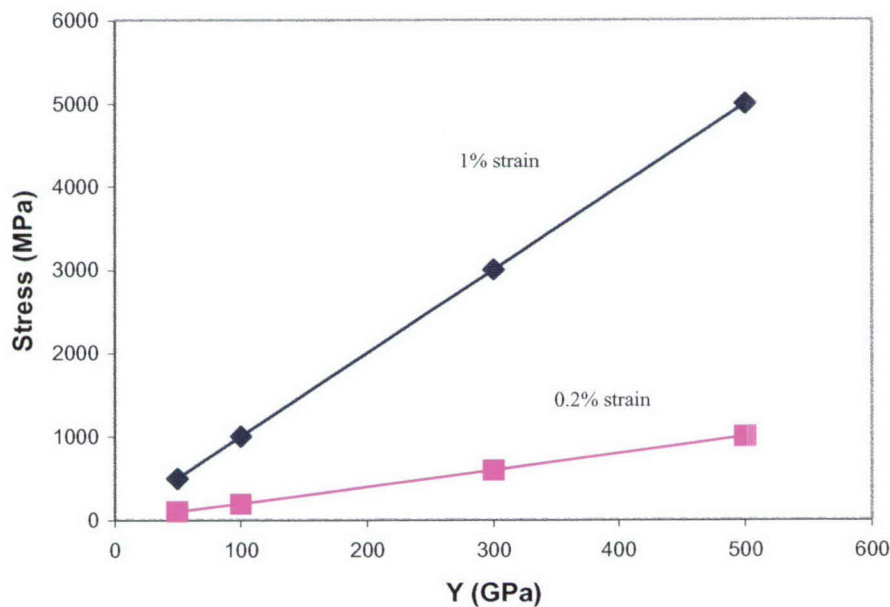
Figure 3.4.5. Calculated stress generated for actuator strains of 1% and 0.2% as a function of the actuator elastic modulus (Y).
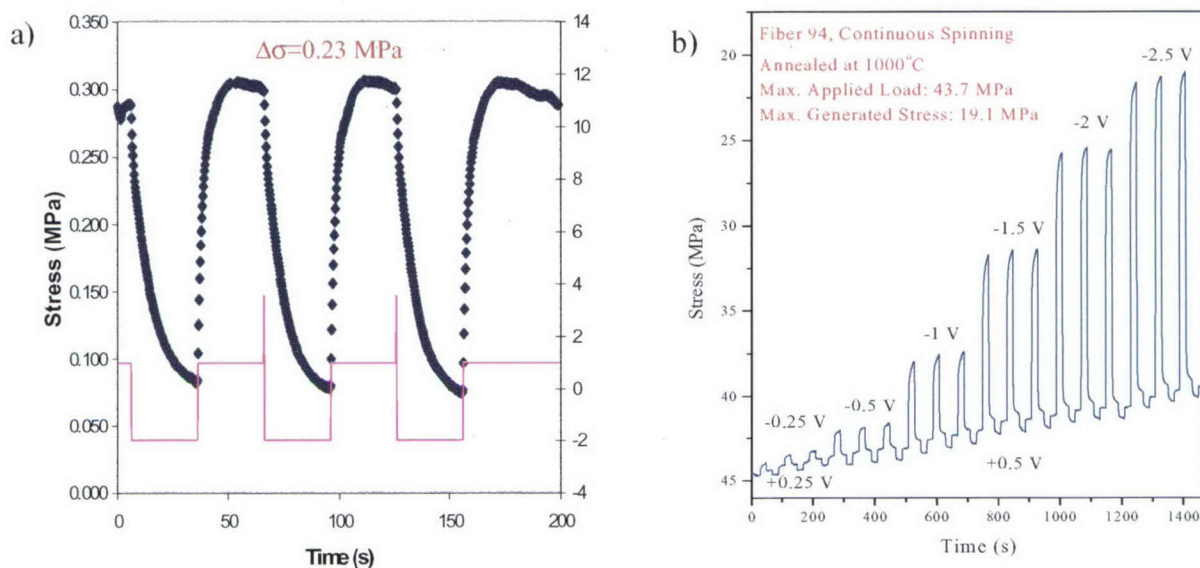
Figure 3.4.6. Isometric stress generated from a) NT sheet and b) NT fiber at the voltages shown.

Another related problem that can limit the stress generation is the non-recoverable actuation strain (creep). A significant reduction in creep was achieved through the welding of nanotube bundles using the SiCN treatment. The welding increases the nanotube sheet modulus by a factor of 5 to 16 GPa. Importantly, the welding significantly reduces the time-dependent deformation of the nanotube sheets and the creep that occurs during electrochemical cycling under load (Fig. 3.4.7). The approximate creep rate of 0.08%/cycle in the unwelded papers was reduced to 0.01%/cycle for welded papers. The actuation strains produced by welded papers were comparable to unwelded papers tested under identical conditions.
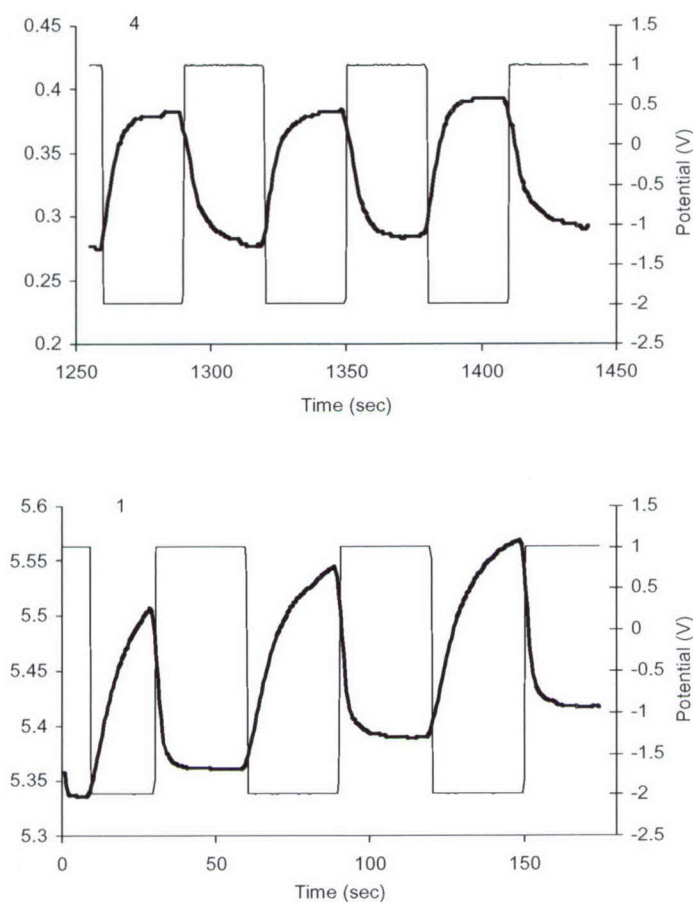
Figure 3.4.7. Strain curves for unwelded (top) and welded (bottom) CNT sheets upon application of 30 sec potential pulses between 1.0 and -2.0 V (*vs* Ag/Ag⁺) in 0.1 M TBATFB/acetonitrile.

High Cycle Life

The third year goal of 10^7 cycles of operation was not achieved; however, progress toward this goal was made by using ionic liquid electrolytes during actuation testing. The first nanotube actuation in ionic liquids was achieved during the program studies. The results of long term (8 hs/1000 cycles) actuation experiments in different electrolytes are summarized in Figure 3.4.8. Clearly, a significant decrease (40-60 %) in strain occurs as time increases when the samples are operated in organic electrolyte. In contrast, much smaller changes are observed in IL. Although the second welded CNT sheet (W3) produced very small (and noisy) strain signals, it still completed the full testing period. On the other hand the sample tested in organic electrolyte broke after around 6 hs of

operation. These findings confirm our initial observations, back last year, suggesting that IL can provide substantially higher stability for CNT actuators.

Another point to arise from these experiments is that the detrimental effect of organic solvent on strain generation appears to be more marked for the welded sheets than for the unwelded material. Whether this is due to specific effects of acetonitrile on the welding material or just a coincidence is not clear at the moment.
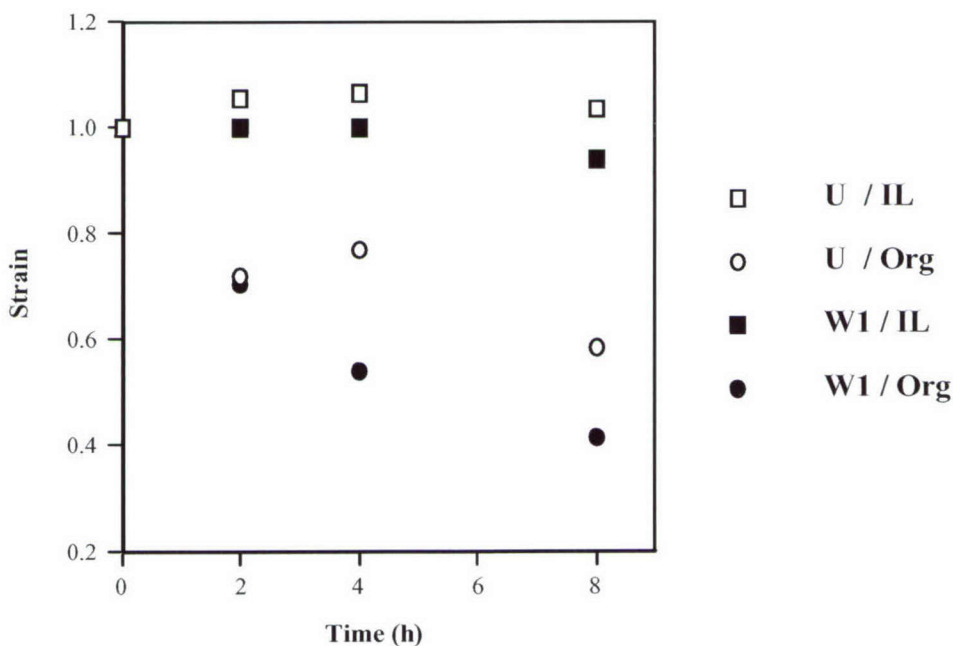

Figure 3.4.8. Normalized strain as a function of time for unwelded (U) and welded (W1) CNT sheets in ionic liquid (IL) and organic (Org) electrolyte upon application of 30 sec potential pulses between 1.0 and -2.0 V.

Demonstration Devices

The main Year 3 goal of the program was to develop practical demonstration devices and the first stage to achieving such demonstrations was the development of solid-state actuator systems. A number of prototype devices were produced that operated in bending or axial contraction mode. Unfortunately, these prototype devices showed much reduced actuation as compared with their operation in liquid electrolytes. Figure 3.4.9 shows stress generation of ~0.1 MPa for prototype solid-state actuators compared with up to 19 MPa for nanotube actuators operated in liquids. This prototype was constructed from two nanotube sheets joined by a layer of PVA/H_3PO_4 solid electrolyte.

The problems identified with solid state electrolytes included lower ionic conductivities, possible inadequate filling of the nanotube pore space and higher mechanical resistance to deformation.
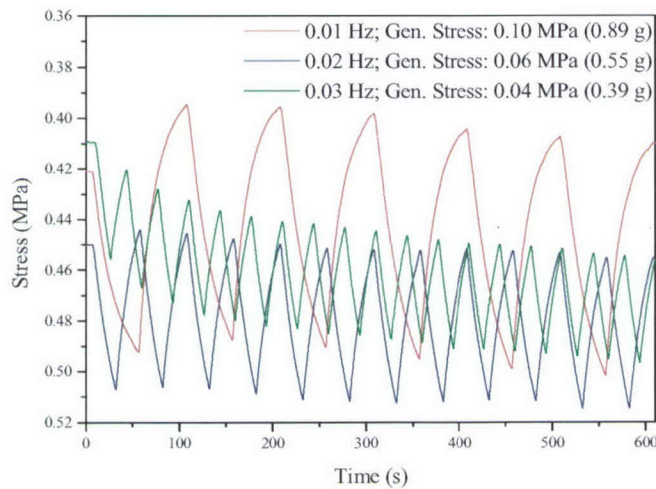

Figure 3.4.9. Prototype solid state actuator operated at different frequencies (applied potential +/- 1V).

A successful prototype was developed as an optical fiber switch. Nanotube electrodes were coated onto a single optical fiber and actuation of the nanotubes caused bending of the fiber. In this way the fiber could be moved to one of two positions. Aligning these positions with two output fibers enabled switching to be monitored. Switching times of 30 msec were demonstrated by using liquid electrolytes.

A number of other actuation composite devices were analysed by the Pisa group, including tunable surface for aeronautic applications (modifiable wings), space antenna (with modifiable curvature) and for car (tunable spoiler for a Formula 1 car). An example of the FEM analysis of the space antenna is shown in Figure 3.4.10.
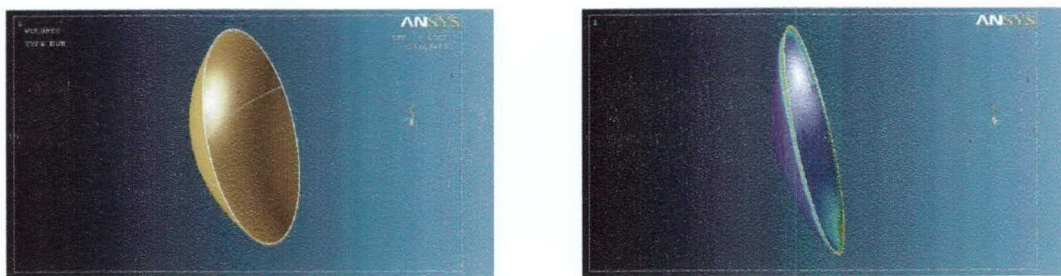
Figure 3.4.10. FEM analysis of space antenna structure using actuating NT fibers for shape change. The Young's modulus of the fibers and matrix were taken in the range 10-50 GPa and 0.01-10 MPa, respectively. The actuation strain was taken to be 0.2-1.0%.

Demonstration and Performance of Single Nanotube Actuators

Considerable effort has being directed toward the demonstration of actuation from a single nanotube. The purposes were to further elucidate the mechanisms of nanotube actuation and to explore the limits of strain, strain rate and stress generation at the fundamental limit. The major limitation in this experiment is to develop a convenient means of measuring the deformation of single nanotubes. AFM techniques are being developed to conduct these measurements.

The approach used was to produce single NT bundles suspended and anchored across a micron-size trench. An AFM was then used to both image the suspended nanotube and deflect it through a controlled amount. Once the tip made contact with the suspended nanotube, an electrical or electrochemical stimulus was applied and the amount of NT deformation is directly determined from the tip deflection.

The Stuttgart team's approach for investigating length changes in an individual nanotube is to measure the deflection of an AFM cantilever placed on a free-standing tube embedded at both ends. Free-standing bundles of SWNTs embedded between two layers of PMMA have been successfully created (Fig. 3.4.11). A conducting AFM tip was placed on the freestanding bundle, and a sinusoidal potential was applied (Fig. 3.4.12. Since electrostatic attraction is proportional to the square of the applied potential, the cantilever response corresponding to it must appear with twice the applied frequency. In this way, actuation can be distinguished from electrostatic attraction.

The measurement shows that there is a non-negligible signal due to the electrostatic attraction, while the actuation peak is almost two orders of magnitude smaller (and hardly above the noise). Since this is a nanotube bundle, the small actuation is not surprising. Taking the relative length changes predicted for a single tube however, the length change of a 500 nm long nanotube would be around 1Å. Due to the geometry of the setup, the deflection AFM tip will change by a much larger value than this. It will still be smaller than the electrostatic effect, so care must be taken to distinguish these effects, but should be detectable with the AFM.

Our measurements show that it is necessary to take into account electrostatic attraction in the actuation measurements on nanotubes charged via the AFM tip, which was not considered before. For electrostatically charged tubes, it is required to have an individual SWNT in order to achieve a measurable charge-induced length change. Then, the signal should be detectable; the noise level in our measurements show that the sensitivity of the AFM is sufficient and work is in progress to achieve free-standing individual single-walled nanotubes in different configurations.
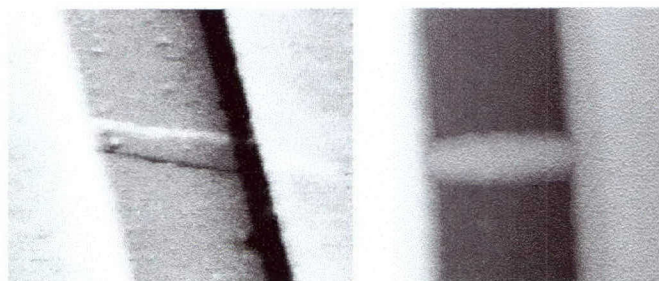
Figure 3.4.11. SEM (left) and AFM (right) of a free-standing SWNT bundle. The width of the trench is 500 nm
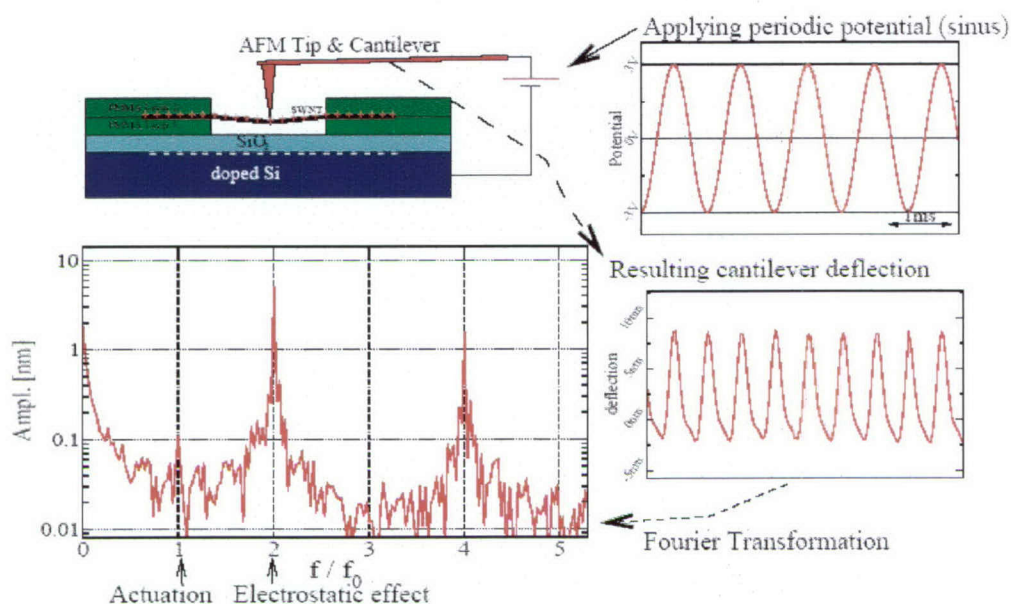
Figure 3.4.12. An actuation measurement. Charge is injected into the free-standing carbon nanotube, and the resulting cantilever deflection is measured. The different dependence of the actuation and the electrostatic attraction from the applied potential is exploited to distinguish these two effects.

At the University of Florida, single nanotube actuation was detected in a suspended nanotube in aqueous electrolyte. Again an AFM tip was used to detect the movement. The displacements were very small (Fig. 3.4.13) which was attributed to problems with electrical contact and with the difficulty in using a reference electrode in the AFM fluid cell.
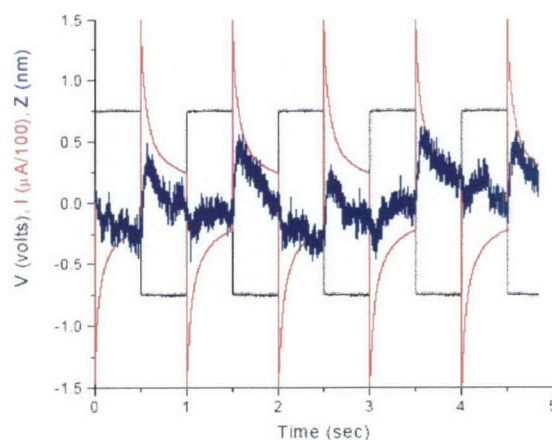
Figure 3.4.13. Piezo-stage Z signal in response to cantilever deflection (due to nanotube length change) in NaCl electrolyte. The deflection observed corresponds to a length change in the nanotubes of ~0.01%

65

Conclusions

Considerable advances in the performance of carbon nanotube actuators have been made during this program. We have achieved nearly 20%/s strain rate which is almost an order of magnitude higher than the pre-program best results. We have demonstrated significantly improved operational lifetimes by the introduction of ionic liquid electrolytes and we have reduced the non-recoverable creep by a factor of 8 by introducing strong bonding (welding) between nanotube bundles. Furthermore, we have quantified the extent of single nanotube actuation by two independent tests. We have constructed both solid state actuator prototypes and made a demonstration optical fiber switch using nanotube actuators. Unfortunately, the goal of producing high stress actuators has still eluded us despite great advances in producing high modulus nanotube fibers. The simultaneous demands of high modulus, high conductivity, high surface area (porous) and high strength for actuators have been difficult to achieve, despite much progress being made.

3.5 ENERGY STORING MULTIFUNCTIONAL STRUCTURES (task leader, John Ferraris)

General Methodology

Sample designation code: Designation codes were used to distinguish different types of CNT fibers and their processing methods, unless specified. The samples are labeled according to the following scheme: The first letter indicates if the fiber is made of Raw (unpurified) nanotubes, Purified single-walled nanotubes or Double-walled nanotubes (R, P or D). The second letter designates the CNT synthesis method: (L) for laser ablation and (H) for HiPCo. The third letter designates the "spinning solution" (or coagulation bath) (from) into which the fibers were spun: P for polyvinyl alcohol [PVA], (S) for concentrated sulfuric acid, and (O) for oleum. The fourth letter designates if the sample is annealed or unannealed (A or U). These four letters are followed by sample numbers provided to us by the fiber-spinning group and correspond to differences in other parameters such as drawing speeds and annealing temperatures.

Single-electrode capacitance measurements: All the experiments in non-aqueous solvents were conducted in a nitrogen-filled dry box. Single-electrode capacitance measurements were performed using a three-electrode cell where the carbon nanotube fiber/paper of approximately 1 cm in length and attached on one end onto a platinum foil (~3 mm x 3 mm) or connector pin using "silver paint" to facilitate subsequent connection to the potentiostat, served as the working electrode. A high surface area (2000 m^2/g) carbon felt wrapped in stainless-steel mesh was used as the counter electrode and Ag/Ag^+ was used as the reference electrode. Cyclic voltammetry experiments were performed by sweeping the potential in an electrolyte at different scan rates using an EG&G PARC 273A potentiostat/galvanostat. Plots of current (i) versus scan rate at a potential chosen from a featureless region of the cyclic voltammogram (typically at 0V to 0.4 V) were constructed and the capacitance was extracted from the slope of the best-fit straight line. Specific capacitance was then calculated by dividing this capacitance value by the sample's weight. The specific capacitance values were also calculated at slow scan rates by measuring the current at a specific potential where no redox processes are occurring and dividing it by the scan rate (Equation 1). The specific capacitance was then calculated by dividing the capacitance by the weight of the sample analyzed.

Capacitance Measurements of Fiber Supercapacitors: The supercapacitors were constructed using two individual fibers as electrodes, separated by a gel electrolyte system. The individual fibers were separately coated with a gel electrolyte and then air-dried. The electrolyte-coated fibers were then entwined and recoated using the same gel electrolyte and dried again. The two leads of the resulting device were attached to platinum foil or connector pins using silver paste. The cyclic voltammograms (CV) of the devices were obtained by sweeping the potential at different potential windows and different scan rates. The plot of current vs. scan rate was used to determine the specific capacitance of the respective device. The capacitance was also obtained at the slowest scan rate using Equation 1.

$$C = \frac{i}{V/s} = \frac{i*s}{V} = Farads \qquad \text{Equation 1}$$

Charge-discharge measurements: The devices were connected to the Arbin Instruments BT-2043 Cycler, charged to a specific potential at constant current and discharged to 0V at varying discharge currents. The energy and power densities were calculated using Equations 2 and 3 shown below.

$$E = \frac{i * t * V/2}{3600 * M} \qquad \text{Equation 2}$$

$$P = \frac{E}{t} \qquad \text{Equation 3}$$

where: E = energy density (Wh kg^{-1})
P = power density (W kg^{-1})
I = current (A)
t = discharge time (s or hr)
V = potential window: charge and discharge (V)
M = weight of the device (kg)

Technical Results

The program was started by characterizing the electrochemical properties of different CNT fibers spun by the UTD fiber-spinning group. Single electrode capacitance measurements of different types of CNT fibers are summarized in Table 3.5.1. The CNT fibers studied were prepared following different synthesis methods and spun into fibers using a variety of dispersions including surfactant and acid dispersions (oleum, H_2SO_4), and spinning solutions/coagulation baths (polyvinyl alcohol, PVA, H_3PO_4, HCl), and subjected to different drawing speeds and annealing protocols.

Highlights of the electrochemical characterization showed the increased capacitance of CNT fibers spun in PVA (RHPU) when annealed (1 F/g to 47 F/g). The implication here is that the surfactant or the coagulant is preventing access to the CNT surfaces within the fibers resulting in low capacitance of the unannealed fibers. Annealing removes the insulating components present in the CNT fiber matrix and increases the electrochemically accessible surface area, therefore, increasing capacitance. The opposite effect was observed for oleum-spun Raw HiPCo fibers wherein annealing (at 1000 °C) dramatically decreases the capacitance of the fibers (from 136 F/g to 31 F/g).

Table 3.5.1. Single-electrode specific capacitance of different CNT fibers.

Entry	Sample designation	Specific Capacitance (F/g)
1	RHPU [2.6]	1
2	RHPU [30.3]	0.23
3	RHPA (450)	42
4	RHPA (1000)	47
5	PHPU [2.6]	0.12
6	PLPU	14.5
7	PLPA (1000)E	13.5
8	PLPA (1000)T	18
9	PHOUT	45
10	PHOUE	93
11	PHOUE	84
12	PHOA (1000)	15
13	RHSU	64
14	RHSU	31
15	RHOUT (Q1)	136
16	RHOA	31
17	RHSUE	52 (25 mV/s)
18	DSUE	50 (5 mV/s) (2V to −1.5V)
19	PFCNF-H_3PO_4-UE	48
20	PFCNF-H_3PO_4-AE (500)	69
21	PFCNF-H_3PO_4-AE (800)	95
22	PFCNF-H_3PO_4-AE(1000)	100
23	PFCNF-HCl-UE	48 (5 mV/s) (± 1.5V)
24	SW/MW- (60:40)-H_3PO_4-UE	83

1st letter: **R:** Fibers from **R**aw (unpurified) CNTs; **P:** Purified CNTs; **D:** Double-walled carbon nanotubes
2nd letter: **H:** HiPCo; **L:** laser ablated; **S:** dispersed in sulfuric acid
3rd letter: **P:** spun in PVA; **S:** dispersed in sulfuric acid; **O:** dispersed in oleum; **U:** unannealed
4th letter: **U:** unannealed; **A:** annealed
(°C); [draw rate. mm/min];
T: tetraethyl ammonium PF_6/acetonitrile;
E: ethylmethylimidazolium bistrifluoromethane sulfonimide (ionic liquid)
PFCNF-H_3PO_4: Polymer-free carbon nanotube fiber spun in 85% H_3PO_4
PFCNF-HCl: Polymer-free carbon nanotube fiber spun in HCl
SW/MW-H_3PO_4: Single-walled/Multi-walled fibers spun in H_3PO_4

This decrease may be due to either the existence of intercalated HSO_4^- ions in the unannealed fibers or degradation of the CNTs by reaction with catalyst or spinning

component residues upon annealing at high temperatures. A similar decrease in capacitance upon annealing (84 F/g to 15 F/g) was observed for Purified HiPCo fibers spun from oleum. Since the residual catalyst concentration is greatly reduced in the purified CNTs, these data suggest that the catalyst does not play a major role in causing the decrease in capacitance upon annealing at 1000 °C.

The similar capacitances obtained from annealed fibers spun in PVA (RHPA) at 450 °C (42 F/g) and 1000 °C (47 F/g) suggests that lower annealing temperatures can be used without compromising the capacitance values, preventing the fibers from becoming too brittle to handle. Although the Annealed, Raw HiPCo fibers spun in PVA (RHPA) have relatively high specific capacitance values (40-50 F/g), these fibers have poor mechanical properties. The annealing process increases the specific capacitance of RHPU fibers, however, it also removes the PVA present in the matrix and in the process makes the fiber very brittle and very hard to handle. This triggered and investigation to dope its unannealed counterpart with H_3PO_4 to increase its conductivity prior to fiber supercapacitor device fabrication.

We have achieved impressive results in the continuous spinning of CNTs in PVA coagulation bath, forming super-tough carbon nanotube fibers, which is discussed further in the section dealing with spinning. Unfortunately, the toughness of these fibers is a result of the formation of a PVA-CNT matrix, and produces as-spun fibers that are quite resistive (due to the presence of ~40% polymer in the bulk of the fiber). In order to circumvent this problem, we used a gel electrolyte system containing phosphoric acid (H_3PO_4) to partially dope the fibers and increase their conductivity. The device constructed following this protocol will be discussed later.

Another solution to this problem is the spinning of fibers that are polymer-free having enough toughness to afford multifunctionality. These polymer-free fibers (pure CNT fibers without PVA) were spun in 85% H_3PO_4 producing acid-doped fibers. The 48 F/g

specific capacitance we reported from these unannealed fibers increased with increasing annealing temperature (Entries 20-22 in Table 1). Polymer-free fibers were also spun in HCl and provided similar capacitance values (48 F/g) as those spun in H_3PO_4. Although the fibers also became more brittle after annealing, we were able to fabricate devices from them as well as from unannealed fibers and will be discussed in the next section of this report. Other types of carbon nanotubes, such as double-wall nanotubes (50 F/g) spun from H_2SO_4 and nanotube composites comprising single-walled and multi-walled nanotubes (83 F/g) also exhibited respectable single-electrode specific capacitances.

The highest single-electrode capacitance obtained was from CNT fibers spun from oleum (136 F/g), however, the safety and handling issues related to the use of oleum are severe disadvantages. In addition, the fibers spun from oleum swell upon cycling in an organic electrolyte becoming very soft and crumbling when handled. We have observed that the continuous increase in capacitance is related to the swelling of these fibers, which is also accompanied by an increase in redox peaks generated upon repeated cycling in different organic electrolytes. The increase in capacitance thus can be due to the combination of double-layer charging and redox processes brought about by the strong oxidizing power of oleum. We have spun fibers from sulfuric acid, a milder dispersion compared to oleum, and obtained relatively high specific capacitances (~50-60 F/g). These fibers were also superior to the oleum-spin fibers in terms of handling. Although swelling of the H_2SO_4-spun fibers upon repeated cycling in 1M $TBABF_4$/ACN electrolyte also occurred, it did so to a lesser extent compared to the oleum-spun fibers. Part of the swelling of these fibers is due to the deposition of an electroactive polymer (polyacetonitrile, PACN) onto/into the fibers when cycled repeatedly at high potentials. The formation of PACN provides redox processes in combination with double-layer charging that results in increased capacitance and thus has potential advantages.

We thus expanded our efforts to understand the swelling of the CNT fibers (spun from CNT dispersed in H_2SO_4) upon repeated cycling (~45 cycles) in 1M $TBABF_4$/ACN electrolyte solution at high potential range (2V to –2V)., The measured specific

capacitance of a single CNT fiber cycled at 25 mV/s in 1M TBABF$_4$/ACN over a potential range of -1V to 1V was 17 F/g (Figure 3.5.1(a)).
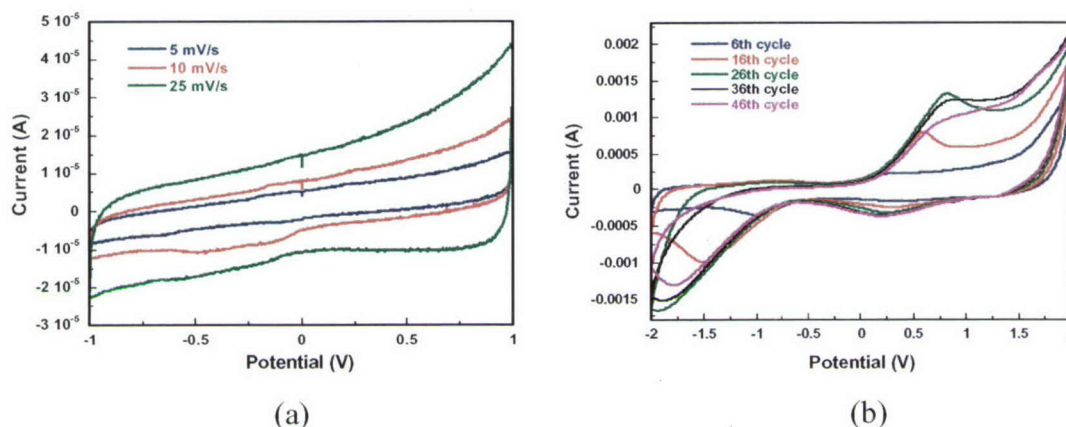

(a)   (b)

Figure 3.5.1. Cyclic voltammograms of CNT fiber (spun from H$_2$SO$_4$) (RHSU) in 1M TBABF$_4$/ACN electrolyte, vs. Ag/Ag$^+$ (0.01M AgNO$_3$) (a) at different scan rates (-1V to 1V potential window), Specific capacitance at 25 mV/s: 17 F/g (b) repeated cycling of CNT fiber (dispersed in H$_2$SO$_4$), at 25 mV/s (2V to –2V potential window), Specific capacitance: 162 F/g (46th cycle).

Repeated cycling of this same fiber (45 cycles) in the same electrolyte system over a wider potential window (-2V to 2V, 25 mV/s) resulted both in fiber swelling and increased specific capacitance (from 17 F/g to 162 F/g) (Figure 3.5.1(b)). Redox processes at ~0.8V become evident as the fiber is continuously cycled over this potential range. The observed redox processes are a result of the formation of an electroactive polymer, polyacetonitrile (PACN), onto/into the CNT fibers, thus forming a conductive polymer (PACN)/CNT fiber composite. The formation of polyacetonitrile at high potentials was recently observed on carbon paper substrates (Spectracarb™) causing increased surface area and therefore increased capacitance.

Figure 3.5.2 shows the continuous increase in specific capacitance with cycle number. After 40 cycles, the capacitance levels off suggestive of a saturation of the accessible polymerization sites.
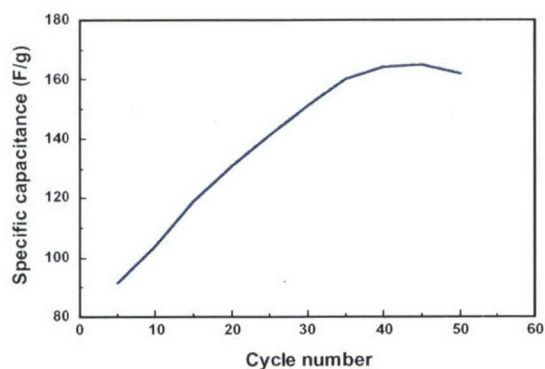
Figure 3.5.2. Plot of Specific capacitance vs. Cycle number, CNT fiber (dispersed in H$_2$SO$_4$) (RHSU) in 1M TBABF$_4$/ACN electrolyte, at 25 mV/s (2V to –2V potential window, vs. Ag/Ag$^+$ (0.01M AgNO$_3$).

We obtained similar results using different electrolytes (different ion sizes) with specific capacitance increasing as the cycle number increases. The highest capacitance (300 F/g) on single fiber electrodes was obtained by repeated cycling at a slower scan rate (10 mV/s).

The PACN-coated fibers were treated with 1M KOH followed by washing with deionized water to remove the PACN. A specific capacitance of 66 F/g (Figure 3.5.3-a) was measured in 1M TBABF$_4$/ACN (1V to –1V, 25 mV/s) from the KOH-washed fiber. This capacitance value is much higher than the baseline specific capacitance value (17 F/g) obtained from the original CNT fiber, but lower than the 162 F/g obtained from the CNT fiber/PACN composite. Removing the PACN from the fibers by base treatment results in increased accessible surface area (the fiber remains expanded) as evidenced by the increased specific capacitance. The cyclic voltammograms (Figure 3.5.3-a) obtained from these runs were more "box-like." However, cycling the same fiber to the potential range of 1.5V to –1.5V again allows the formation of PACN (as indicated by the redox processes present in the cyclic voltammograms) and increased specific capacitance (127 F/g) (Figure 3.5.3-b). Therefore, the high specific capacitance values previously reported for CNT fibers (H$_2$SO$_4$) are due to a combination of double-layer charging and pseudocapacitance.

(a)   (b)
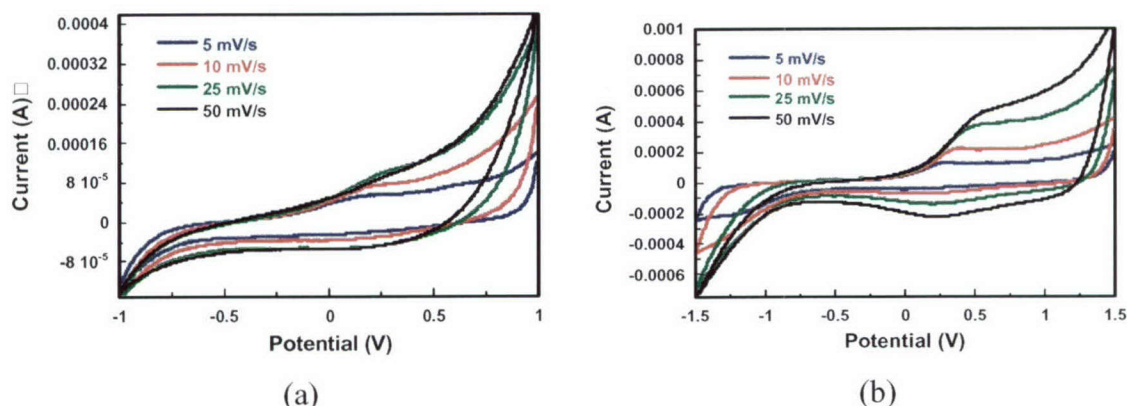
Figure 3.5.3. Cyclic voltammograms of CNT fiber (dispersed in H_2SO_4) (RHSU) in 1M TBABF$_4$/ACN electrolyte after KOH-wash, at different scan rates (vs. Ag/Ag$^+$ (0.01M AgNO$_3$), (a) 1V to –1V potential window, Specific capacitance at 25 mV/s: 66 F/g; (b) 1.5V to –1.5V potential window, Specific capacitance at 25 mV/s: 127 F/g).

When as-received CNT fibers (H_2SO_4) were cycled in the ionic liquid electrolyte, ethylmethylimidazolium imide (EMIIm), the working potential window could be increased without forming PACN. Specific capacitance measurements on these fibers gave 18 F/g (Figure 3.5.4-a) when cycled in the 1V to –1V range at 25 mV/s increasing to 42 F/g over the 2V to –1.5V cycling range (Figure 3.5.4-a).

(a)   (b)
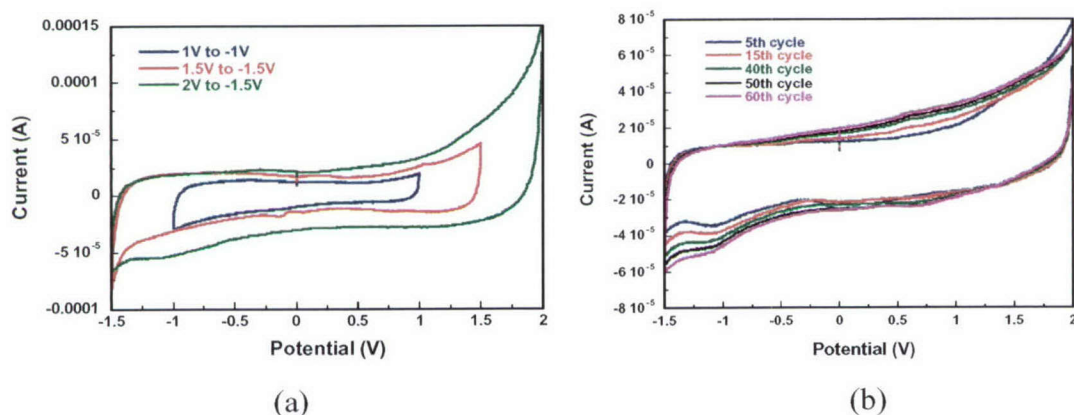
Figure 3.5.4. Cyclic voltammograms of CNT fiber (dispersed in H_2SO_4) (RHSU) in EMIIm (ionic liquid electrolyte) at 25 mV/s, (vs. Ag/Ag$^+$ (0.01M AgNO$_3$) (a) different potential windows, Specific capacitance at 1V to –1V: 18 F/g, at 2V to-1.5V: 42 F/g; (b) repeated cycling of CNT fiber (dispersed in H_2SO_4) in EMIIm (ionic liquid electrolyte), at 25 mV/s (2V to –1.5V potential window), Specific capacitance: 50 F/g (60th cycle).

Repeated cycling of the fibers in EMIIm in the 2V to –1.5V potential range increased the specific capacitance from the initial 40 F/g to 50 F/g (after 60 cycles) (Figure 3.5.4-b). *This result indicates that EMIIm also swells the fibers upon cycling without forming PACN.* More importantly, the cyclic voltammograms in Figure 3.5.4-b show "box-like" profiles, which are characteristic of double-layer charging.

Repeated cycling (45 cycles) of the fibers in 1M TBABF$_4$/ACN followed by KOH-washing prior to cycling in EMIIm did not enhance the specific capacitance of the fibers above the 42 F/g obtained when the fiber was only cycled in EMIIm electrolyte system. We were able to fabricate fiber supercapacitor devices using both types of electrodes (composite electrodes of PACN/RHSU and RHSU cycled in EMIIm), which will be discussed in the next section. Other types of composite fibers using a combination of single-walled and multi-walled fibers were investigated.

Fiber Supercapacitor Devices

A summary of the fiber supercapacitor devices fabricated and characterized is shown in Table 3.5.2. The low specific capacitance of single-electrode Unannealed, Raw HiPCo fibers spun in PVA (RHPU) was improved by dipping the fibers in an electrolyte comprised of 2M H$_3$PO$_4$ in 5% PVA to dope the fibers and improve their conductivity. These devices gave specific capacitance values in the range of **5-6 F/g** (Figure 3.5.5) and are strong enough to be woven into textiles (Figure 3.5.6). Fibers spun from H$_2$SO$_4$ as well as fibers spun in a coagulation bath consisting of 50:50 PVP and PVA gave specific capacitance values around 2-4 F/g using the same electrolyte. We also tried to improve the conductivity of RHPU fibers by soaking these fibers in 85% H$_3$PO$_4$ prior to coating with 2M H$_3$PO$_4$/5% PVA electrolyte. Unfortunately, there was no improvement in the capacitance of this device owing to the ineffective incorporation of H$_3$PO$_4$ into the fibers.
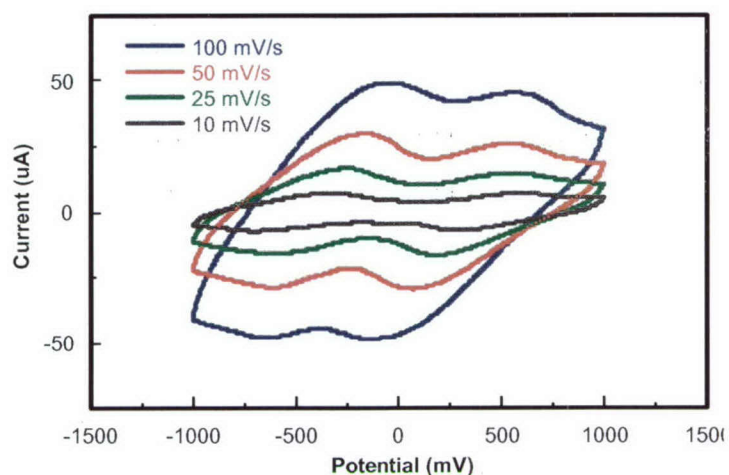
Figure 3.5.5. Cyclic Voltammogram of RHPU/2M H_3PO_4-5%PVA supercapacitor device at different scan rates (with IR compensation), *Entry 2* in Table 3.5.2.
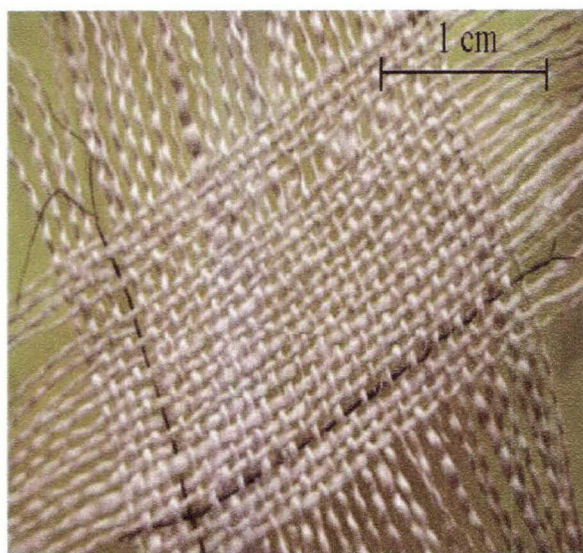
Figure 3.5.6. Photograph of a textile containing two nanotube-fiber supercapacitors woven in orthogonal directions. The helically wound nanotube fibers are separated at the capacitor ends so that electrical connections can be made.

Several fiber supercapacitor devices were fabricated using fibers spun from H_2SO_4 (RHSU), and repeatedly cycled in 1M $TBABF_4$/ACN, consequently forming the electroactive polymer PACN. The composite fibers coated with either $LiBF_4$/5% PVA or $LiBF_4$/polymethylmethacrylate (PMMA) / ethylene carbonate (EC) / propylene carbonate (PC) electrolyte gave a specific capacitance of **12 F/g** (Figure 3.5.7). Although redox

peaks were not observed in the cyclic voltammograms of these devices, the relatively high specific capacitance obtained from these fibers is due to the combination of double-layer and faradaic effects present in the devices.

(a)　　　　　　　　　　　　　　　(b)
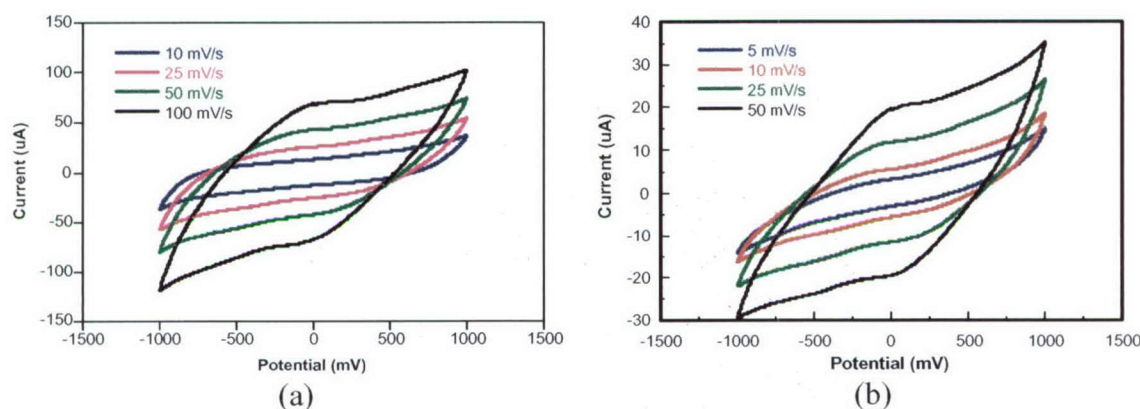
Figure 3.5.7. Plot of current vs. potential for (a) RHSU-2M LiBF$_4$/5%PVA fiber supercapacitor device at different scan rates, fibers cycled in 1M TBABF$_4$/ACN prior to device fabrication, *Entry 7* in Table 3.5.2; (b) RHSU- 1M LiBF$_4$/PMMA/EC/PC fiber supercapacitor device at different scan rates, fibers cycled in 1M TBABF$_4$/ACN prior to device fabrication, *Entry 8* in Table 3.5.2.

Different electrolyte systems were studied to fabricate solid-state devices that are stable at a wide potential window (~4V) and have significant conductivities (10 mS cm^{-1}). These electrolytes comprised ionic liquids (IL) or molten salts, typically consisting of a nitrogen-containing organic cation and inorganic anion. These electrolytes are liquid at room temperature, non-volatile, nonflammable, and have high thermal stability. Ionic liquids can also be obtained in a very dry state, making them very suitable in moisture-sensitive systems. One advantage of ionic liquids is that they can either be transformed into soft, elastomeric solids at room temperature by addition of small amounts of an elastomeric polymer, forming a polymer-in-salt composite or they can be used as solvents to synthesize an elastomeric polymer to form a polymer ionic liquid.

We used these polymer ionic liquids (PIL) as our solid-state electrolyte by *in-situ* polymerization of methylmethacrylate (MMA) dissolved in an ionic liquid

(ethylmethylimidazolium imide, EMIIm) in the presence of an initiator (benzoyl peroxide) and a cross-linker (tetraethylene glycol diacrylate) onto the CNT fiber electrodes.

Devices made of CNT paper (from CNTs dispersed in H_2SO_4) cycled in 1M TBABF$_4$/ACN and in EMIIm ionic liquid, and coated with PIL electrolyte were initially fabricated and gave specific capacitance values of **11 F/g** at 2V to –1.5V potential range (Figure 3.5.8-a). CNT fibers spun from H_2SO_4, cycled in 1M TBABF$_4$/ACN and EMIIm ionic liquid, coated with PIL gave **6 F/g** specific capacitance at 5 mV/s and ±2V potential window (Figure 3.5.8-b).

(a)   (b)
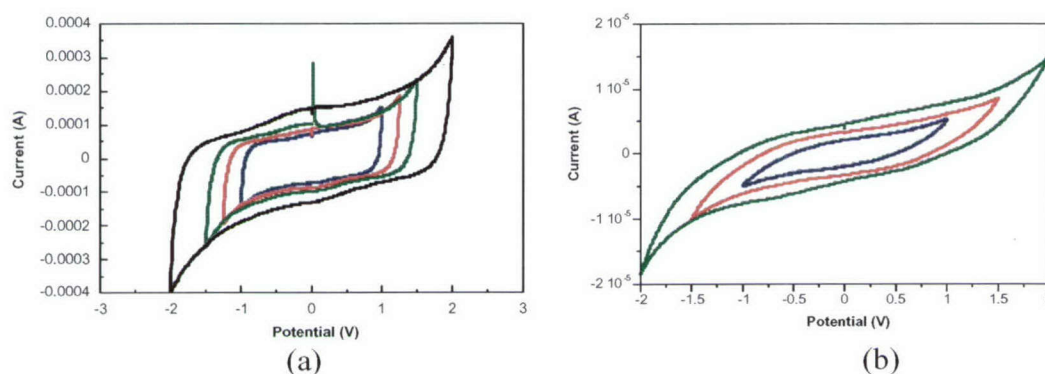
Figure 3.5.8. Cyclic voltammograms of (a) RHSU paper-PIL supercapacitor device at varying potential range (5 mV/s), *Entry 9* in Table 3.5.2; (b) RHSU-PIL supercapacitor device at varying potential range (5 mV/s), *Entry 10* in Table 3.5.2. Electrodes were cycled in 1M TBABF$_4$/ACN, and EMIIm prior to device fabrication.

It is interesting to note that even without forming polyacetonitrile onto the fibers, repeated cycling in an ionic liquid such as EMIIm also gave ~50 F/g single-electrode capacitance. Redox peaks were not observed when these fibers were cycled in EMIIm, therefore, the increase in single electrode capacitance from 40 F/g to 50 F/g after 60 cycles is likely due to the ion insertion/extraction processes, which increases the electrochemically accessible surface area in the fibers. The devices fabricated using fibers spun from H_2SO_4 (RHSUE) (repeatedly cycled in EMIIm) and PIL electrolyte gave

"box-like" features consistent with double-layer charging with specific capacitance of **11 F/g** at 5 mV/s, at 2V to −1.5V potential window (Figure 3.5.9).
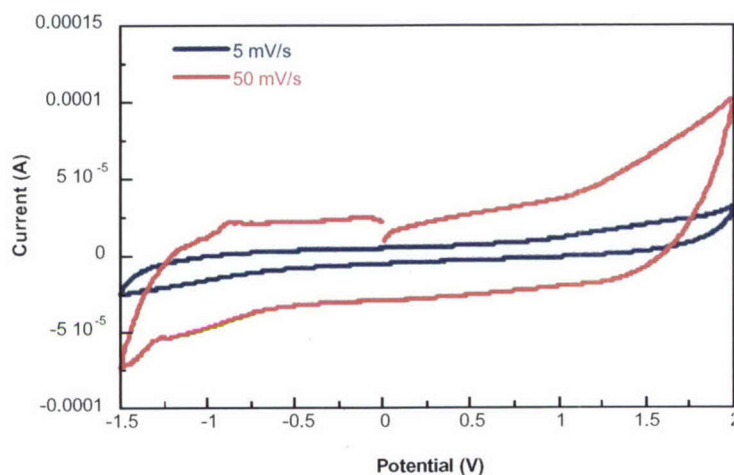
Figure 3.5.9. Cyclic voltammogram of a RHSUE-PIL supercapacitor device at different scan rates (2V to −1.5V), *Entry 11* in Table 3.5.2.

We also constructed fiber supercapacitor devices using double-walled carbon nanotube fibers (DSUE) (cycled in EMIIm), coated with PIL electrolyte. These devices afforded specific capacitances of **8 F/g** when cycled in the 2V to −1.5V potential window at 5 mV/s with characteristic double-layer features at slow scan rates (Figure 3.5.10).
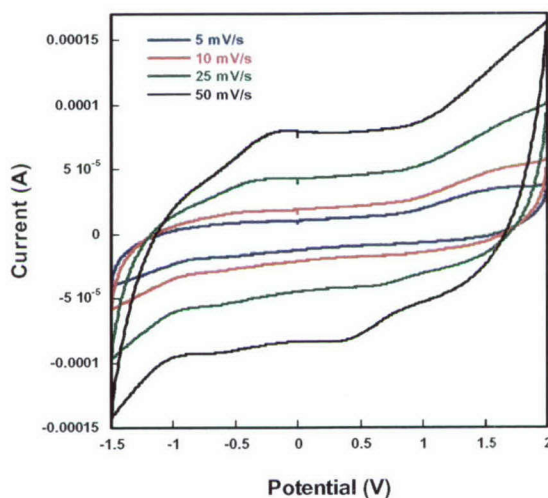
Figure 3.5.10. Cyclic voltammograms of DSUE-PIL fiber supercapacitor device at different scan rates (2V to −1.5V potential range), *Entry 12* in Table 3.5.2.

In order to improve the electrochemical properties of our CNT fibers while maintaining acceptable mechanical properties, we constructed devices using polymer-free fibers (pure CNTs without PVA). These fibers were spun in acid (H_3PO_4 or HCl) from a dispersion of CNTs in lithium dodecylsulfate (LDS). Tensile strength measurements of annealed (1000 °C) polymer-free fibers spun in H_3PO_4 gave 46 MPa and unannealed PFCNFs spun in HCl gave 90 MPa as opposed to the fibers spun from H_2SO_4 (dispersed in H_2SO_4 (RHSU)), spun in ether), which are weaker. Annealed PFCNFs (1000 °C) using the PIL electrolyte system gave a specific capacitance of **9 F/g** at ±1.5V at 5 mV/s, while unannealed PFCNFs spun in HCl using PIL electrolyte provided a specific capacitance of **7.35 F/g** (Figure 3.5.11).

(a)   (b)
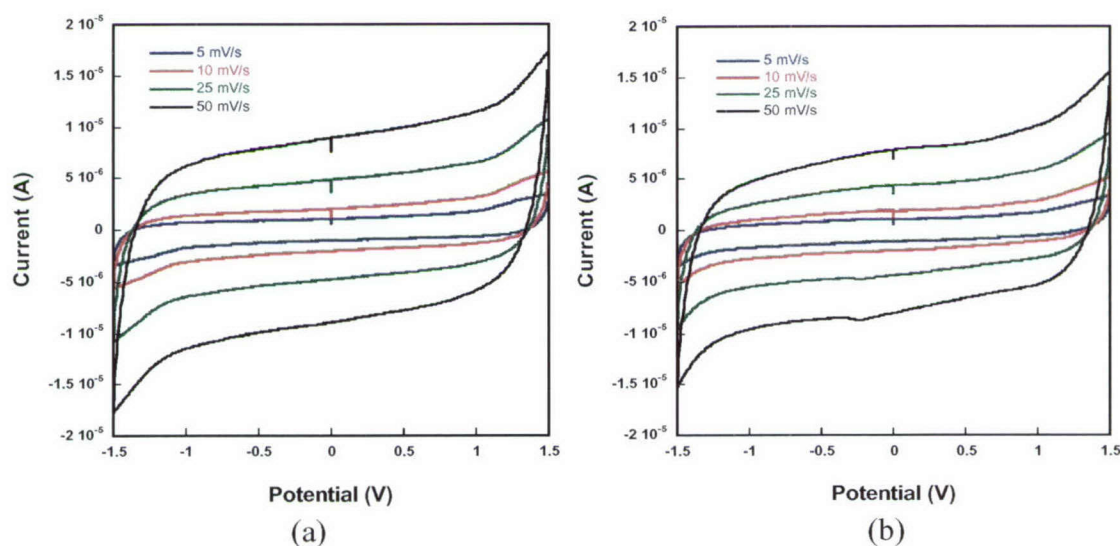
Figure 3.5.11. Cyclic voltammograms of (a) PFCNF-H_3PO_4-AE(1000)-PIL fiber supercapacitor device at different scan rates, *Entry 13* in Table 3.5.2; (b) PFCNF-HCl-UE-PIL fiber supercapacitor device at different scan rates, *Entry 14* in Table 3.5.2. Electrodes were cycled in EMIIm prior to device fabrication.

Energy and Power Densities

Charge-discharge studies were performed on RHPU-2M H_3PO_4/5%PVA fiber supercapacitor device by charging to 0.5V at constant current (1 uA) and discharging to 0V at varying rates (0.25, 0.5, 0.75, 1.0, 2.0, 3.0, 5.0, and 7.5 uA). The Ragone plot (power density vs. energy density) (Figure 3.5.12) showed energy and power densities of **0.14, 0.13, and 0.12 Wh/kg** and **2.78, 13.8, and 21.0 W/kg** at 1.0, 5.0, and 7.5 µA

discharge currents, respectively. The performance characterization of the fiber supercapacitors was then extended out to 1V by charging at 5 µA constant current and discharging to 0V at -1.0 and -5.0 µA. The expected 4X increase in energy density at 1.0V (**0.57 and 0.61 Wh/kg** vs 0.14 and 0.13 Wh/kg previously reported for 0.5V charging) was observed for both −1.0 and −5.0 µA discharge currents, respectively, and is within a factor of 2-3 of typical values observed for commercially available aqueous-based DLCs operating at 1V.
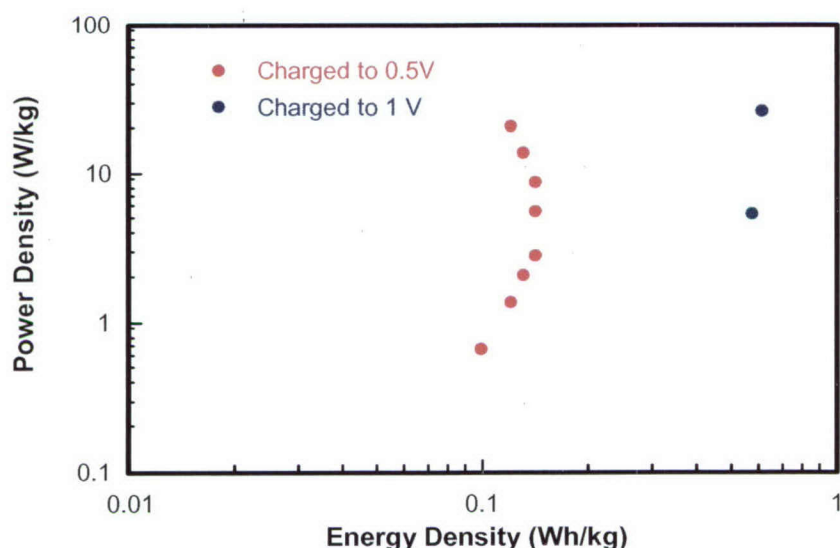
Figure 3.5.12. Ragone plot of RHPU-2M H_3PO_4/5%PVA fiber supercapacitor device, *Entry 2* in Table 3.5.2.

The energy and power densities of CNT fiber supercapacitor devices using fibers spun from H_2SO_4 (RHSUE) and PIL electrolyte were also measured by charge-discharge measurements. The device was charged to 0.5V, 1.0V, and 1.5V at constant current and discharged to 0V at varying discharge currents (25, 50, 75, 100, 150, 175, 200, 250, 300 µA). The energy and power densities at 1.5V charging were **1.34 Wh/kg** and **1.2 kW/kg**, respectively, and are stable for at least 2300 cycles (Figure 3.5.13).
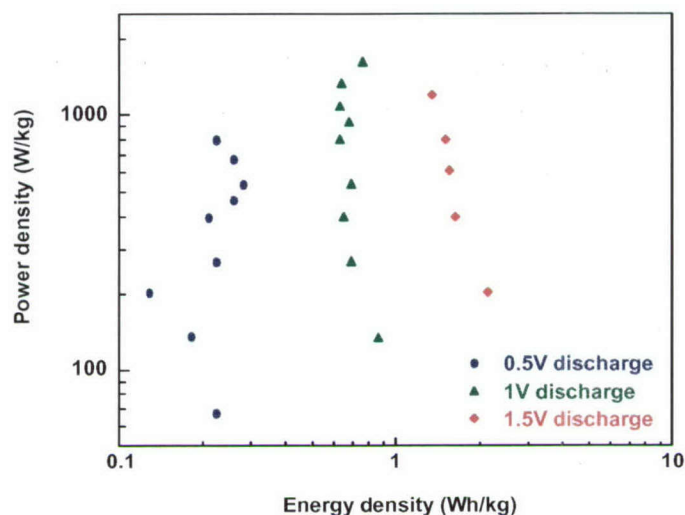
Figure 3.5.13. Ragone plot of RHSUE-PIL fiber supercapacitor device, *Entry 11* in Table 3.5.2.

Fiber devices comprising DSUE-PIL were charged to 1V, 1.5V and 2V at constant current (25 µA) and discharged to 0V at different discharge currents (-25, -50, -100, -150, -200, -250, -300 µA) to measure the energy and power densities. When charged to 2V an energy (power) density of **5.7 Wh kg^{-1} (86.2 W kg^{-1}.)** was observed. Increasing the discharge rate afforded **1.2 Wh kg^{-1}** and **1.0 kW kg^{-1}** (Figure 3.5.14). The device also showed stable charge-discharge processes for at least 2100 cycles.
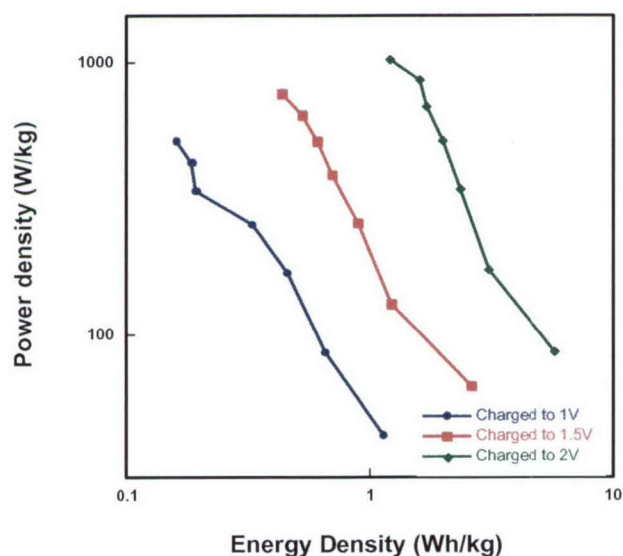
Figure 3.5.14. Ragone plot of DSUE-PIL fiber supercapacitor device, *Entry 12* in Table 3.5.2.

Table 2. Specific capacitance of fiber supercapacitor devices.

Entry	Sample designation	Electrolyte	Specific capacitance (F/g)
1	RHPU	2M H_3PO_4/5%PVA	5.40
2	RHPU	2M H_3PO_4/5%PVA	6.85
3	PHPA76	2M H3PO4/5%PVA	2.20
4	RHSU	2M H_3PO_4/5%PVA	3.70
5	RHPPU (PVP:PVA)	2M H_3PO_4/5%PVA	2.20
6	RHPU74	(soaked in 85% H_3PO_4) 2M H_3PO_4/5%PVA	4.20
7	RHSU	$TBABF_4$/ACN, 2M $LiBF_4$/5%PVA	12.0
8	RHSU	$TBABF_4$/ACN 1M $LiBF_4$/PMMA/EC/PC	12.6
9	RHSU paper	$TBABF_4$/ACN, EMIIm, PIL (1:0.75 MMA:EMIIm)	5.98 ($\pm$1V) 7.05 ($\pm$1.25V) 8.12 ($\pm$1.5V) 11.5 ($\pm$2V) (5 mV/s)
10	RHSU	$TBABF_4$/ACN, EMIIm, PIL (1:0.75 MMA:EMIIm)	3.50 ($\pm$1V) 4.50 ($\pm$1.5V) 6.00 ($\pm$2V) (5 mV/s)
11	RHSUE	EMIIm PIL (1:0.75 MMA:EMIIm)	6.0 ($\pm$1V) 11.0 (2V to $-$1.5V) (5 mV/s)
12	DSUE	EMIIm PIL (1:0.75 MMA:EMIIm)	8.00 (5mV/s) (2V to-1.5V)
13	PFCNF-H3PO4-AE (1000)	EMIIm PIL (1:0.75 MMA:EMIIm)	9.00 ($\pm$1.5V) (5 mV/s)
14	PFCNF-HCl-UE	EMIIm PIL (1:0.75 MMA:EMIIm)	7.35

$TBABF_4$/ACN: single-electrode fibers repeatedly cycled in 1M $TBABF_4$/ACN electrolyte prior to device fabrication

EMIIm: single-electrode fibers repeatedly cycled in EMIIm ionic liquid electrolyte prior to device fabrication

PIL: 1:0.75 mole% MMA:EMIIm, 2 mole% benzoyl peroxide and tetraethylene glycol diacrylate with respect to MMA

Our solid-state fiber supercapacitor devices display specific capacitance values ranging from 6 F/g to 12 F/g and energy and power densities reaching 1.34 Wh/kg and 1.0 kW/kg, respectively. We anticipate that these promising results could be further enhanced by increasing the electrochemically accessible surface area while maintaining enough strength and toughness for mechanical usage. At present the electrochemical performance of these devices are limited by the inherently lower conductivities of the solid-state electrolytes being used, as compared to liquid electrolytes.

3.6 OTHER FUNCTIONS FOR MULTIFUNCTIONAL STRUCTURES
(task leader, Gordon Wallace)

The function of this section was to explore in an opportunistic manner that did not distract significant effort from the main program thrusts. Leveraging of effort was possible since these other functions use a similar two-electrode structure as do the actuation and energy storage functions.

Thermoelectrochemical Energy Harvesting

Single-wall carbon nanotubes (SWNTs), supplied by Carbon Nanotechnologies Inc., or multi-wall carbon nanotubes (MWNTs), synthesized by University of Texas at Dallas, were dispersed in 1% Triton X-100 and filtered off using 0.22 µm pore size polyvinylidene fluoride (PVDF) membrane at 400 kPa nitrogen pressure. After washing by filtration with water followed by methanol, the CNT mat was allowed to dry on the membrane. When dry, the CNT mat was peeled off the membrane and cut into strips to be used as electrodes (anode and cathode) for thermoelectrochemical energy harvesting.

Thermoelectrochemical energy harvesting was performed in a cell as depicted in Figure 3.6.1. The inter-electrode distance was 10 cm. The cold side was cooled by a cold water jacket whilst the hot side was heated with a heating coil.
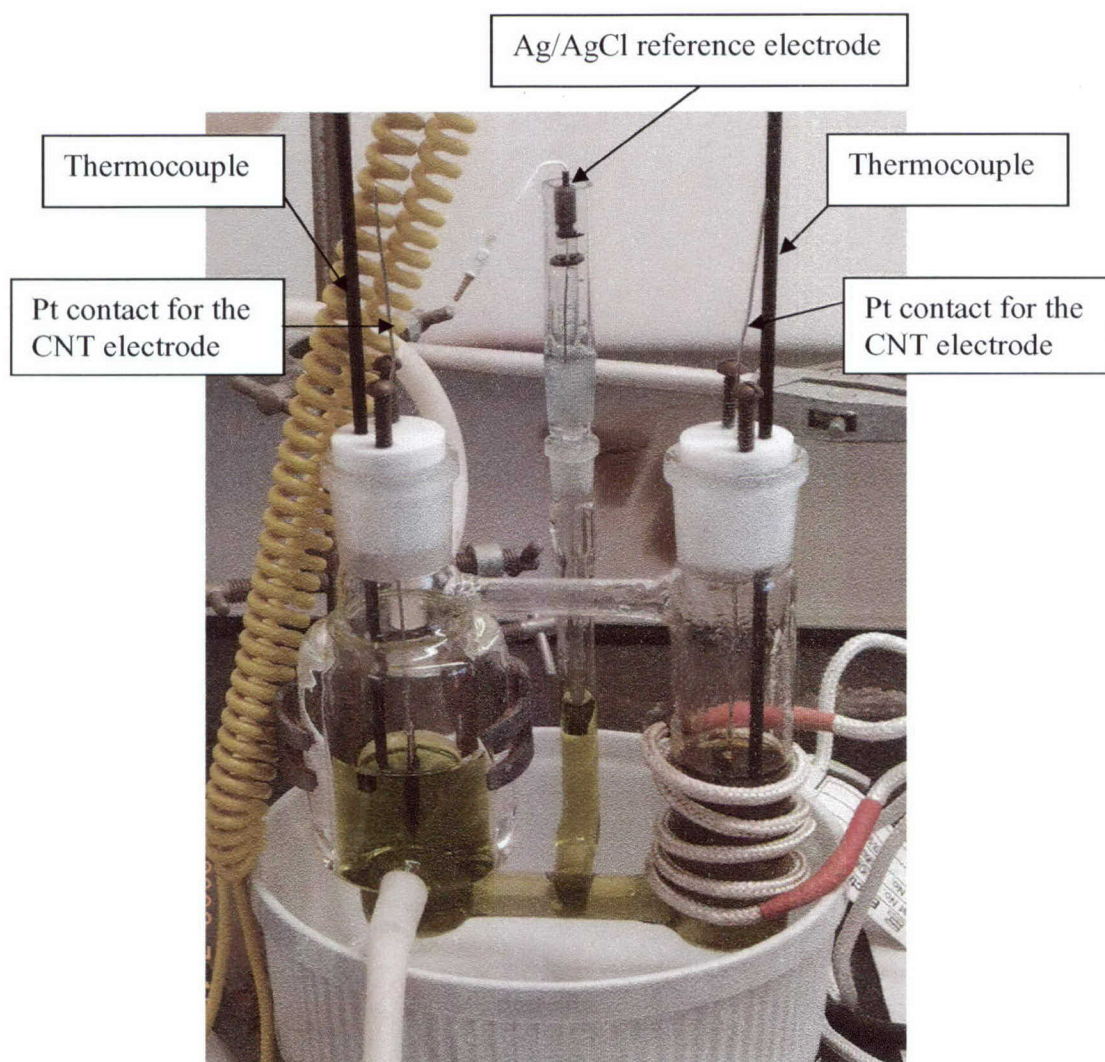
Figure 3.6.1. Thermoelectrochemical energy harvesting cell.

The following electrolytes were considered: 30% HNO_3 in water, K_4FeCN_6/K_3FeCN_6 in water, $FeCl_2/FeCl_3$ in water or in 1M HCl. In addition, Iodolyte TG500 (Solaronix SA) and a number of ionic liquids were also considered (Figure 3.6.12); especially for high temperature (> 100 $^\circ$C) applications.
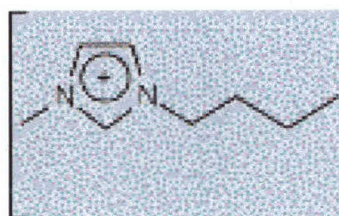
$[FeCl_4]^-$ or $[FeCl_3]^-$
or BF_4^- or
$(CF_3SO_2)_2N^-$

Figure 3.6.2. 1-Butyl-3-methyl imidazolium cation with a variety of anions.

Results and Discussion

Initial investigations were performed on HiPco SWNT electrodes in 30% nitric acid. The results (Table 3.6.1) show that, for a temperature difference of 61.5 – 61.7 $^{\circ}$C, the performance decreased over time; the short circuit current density halved between 17 hours and 46 hours of operation.

Table 3.6.1. Thermoelectrochemical results obtained from 'as received' HiPco SWNT electrodes after several hours of operation at maximum temperature difference in different electrolytes.

Hours of operation	Electrolyte	Temperature difference ($^{\circ}$C)	V_{oc} (mV)	I_{sc} (A/kg)	Maximum Power ((I_{sc} x V_{oc})/4, W/kg)
17	30% HNO_3	61.5	49.6	49.0	0.61
	0.4M ferri-/ferro-cyanide	63.5	85.9	136.0	2.9
46	30% HNO_3	61.7	60.0	24.8	0.37
	0.4M ferri-/ferro-cyanide	61.6	79.1	124.5	2.5

It was also observed that there was 24.2% weight loss for the hot cathode. This is clear evidence that the SWNT electrode was degraded by the hot nitric acid. This was independently confirmed by Raman Spectroscopy and cyclic voltammetry (CV) of the SWNT electrodes after the thermoelectrochemistry experiments.

In view of these findings on the degradation of SWNTs by hot 30% nitric acid, an alternative redox system was identified. This system is the ferri-/ferro-cyanide system where the hot side is the anode and the cold side is the cathode; which is opposite to the 30% nitric acid system. Preliminary experiments using 0.4 M each of potassium ferricyanide and potassium ferrocyanide were performed and the encouraging results are given in Table 3.6.1.

Table 3.6.1 shows that thermoelectrochemical power generation from the ferri-/ferro-cyanide system is consistently much higher than from the 30% nitric acid system. This is especially so at longer periods of operation because the drop in maximum power generation was much more severe in the 30% nitric acid system. For example, the maximum power generated from the ferri-/ferro-cyanide system after 17 hours of operation was 4.8 times higher than from 30% nitric acid, but this multiple increases to 6.7 times after 46 hours of operation. No weight loss of the hot electrode was observed, indicating that the SWNT electrode is stable in hot ferri-/ferro-cyanide electrolyte. The similar CVs of the SWNT electrode obtained before and after thermoelectrochemistry also lend credence to this stability. Therefore, further investigations were focused on the promising ferri-/ferro-cyanide system.

Effect of Electrolyte

Initially, the concentration and composition of the electrolyte were considered. Thus, dilute solutions of 0.2 M potassium ferricyanide/0.2 M potassium ferrocyanide with or without 0.8 M KCl supporting electrolyte were tested in addition to the 0.4 M potassium ferricyanide/0.4 M potassium ferrocyanide. The electrodes used were made from 'as received' HiPco SWNT. The results show that the Open Circuit Voltages (V_{oc}) generated were quite similar (Fig. 3.6.3), but higher Short Circuit Currents (I_{sc}) were obtained from 0.4M ferri-/ferro-cyanide or from 0.2M ferri-/ferro-cyanide in 0.8M KCl supporting electrolyte (Fig. 3.6.4). Both V_{oc} and I_{sc} values increased linearly with increasing Temperature Difference (ΔT). The maximum power (P_{max}) in all three solutions increased non-linearly with increasing ΔT and the values were similar (Fig. 3.6.5).

The results obtained after operation over an extended period of time (Table 3.6.2) show that the thermoelectrochemical performance in 0.4M ferri-/ferro-cyanide was better and more stable than in the other two electrolytes investigated. After 46 hours, V_{oc} was 79.1 mV, I_{sc} was 124.5 A/kg and P_{max} was 2.46 W/kg; which is over 50% higher than those obtained from the other two electrolyte solutions.
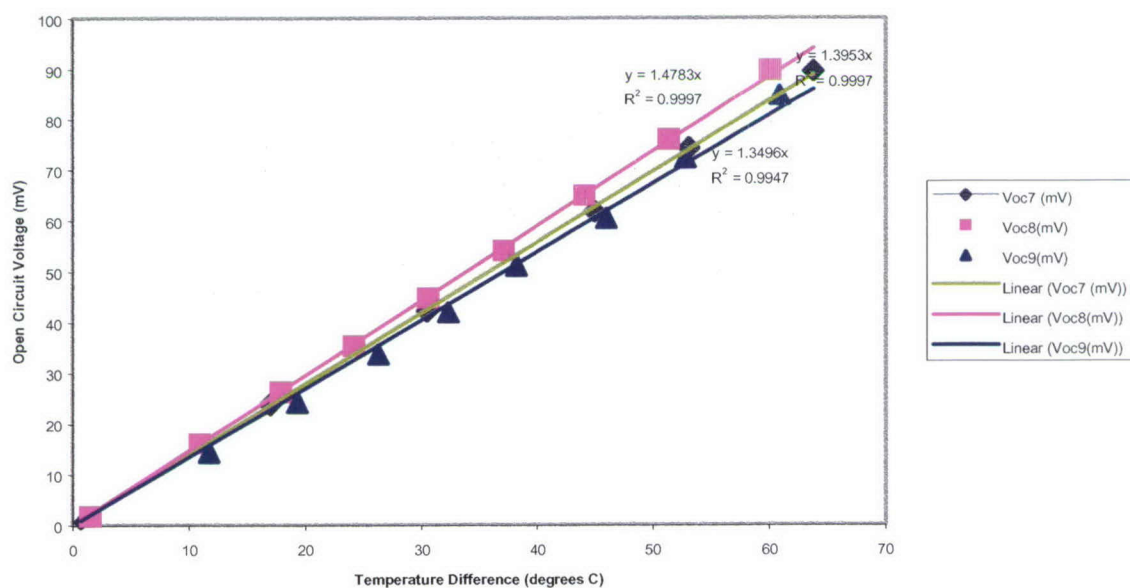

Figure 3.6.3. Open Circuit Voltage vs Temperature Difference for HiPco SWNT (7: 0.4M ferri-/ferro-cyanide, 8: 0.2M ferri-/ferro-cyanide, 9: 0.2M ferri-/ferrocyanide in 0.8M KCl).
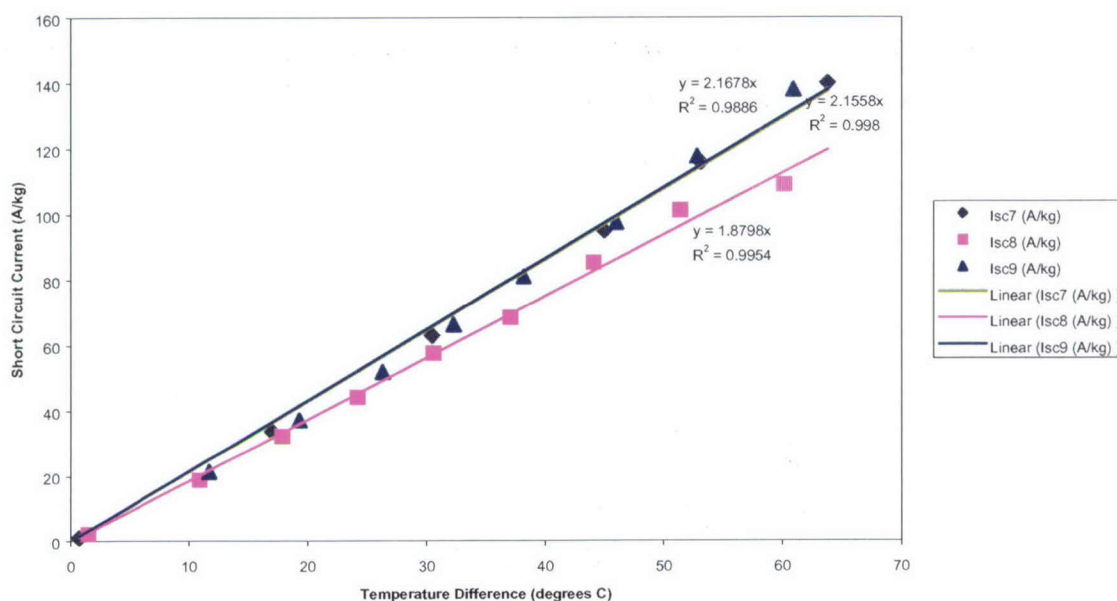
Figure 3.6.4. Short Circuit Current vs Temperature Difference for 'As Received' HiPco SWNT Electrodes (7: 0.4M Ferri-/Ferro-cyanide, 8: 0.2 M Ferri-/Ferro-cyanide, 9: 0.2 M Ferri-/Ferro-cyanide in 0.8 M KCl).
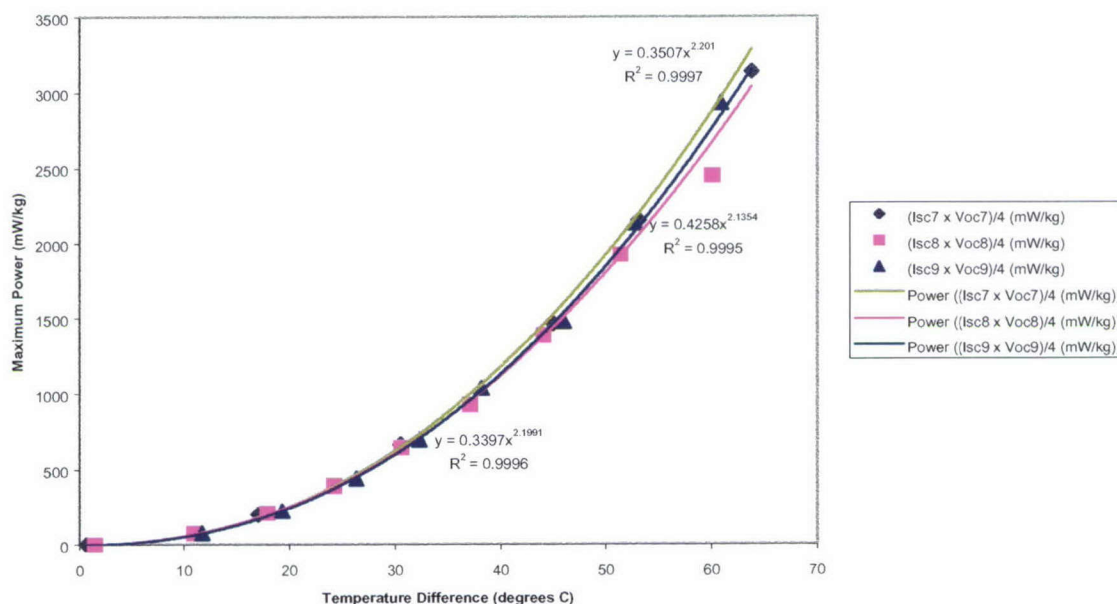
Figure 3.6.5. Maximum Power vs Temperature Difference for 'As received' HiPco SWNT Electrodes (7: 0.4M Ferri-/Ferro-cyanide, 8: 0.2M Ferri-/Ferro-cyanide, 9: 0.2M Ferri-/Ferro-cyanide in 0.8M KCl).

Table 3.6.2. Thermoelectrochemical results obtained from 'as received' HiPco SWNT electrodes after several hours of operation at maximum temperature difference in different electrolytes.

Hours of operation	Electrolyte	Temperature difference (^oC)	V_{oc} (mV)	I_{sc} (A/kg)	Maximum Power ((I_{sc} x V_{oc})/4, W/kg)
17	0.4M ferri-/ferro-cyanide	63.5	85.9	136.0	2.92
	0.2M ferri-/ferro-cyanide	59.5	80.3	108.0	2.17
	0.2M ferri-/ferro-cyanide in 0.8M KCl	61	80.3	128.6	2.58
46	0.4M ferri-/ferro-cyanide	61.6	79.1	124.5	2.46
	0.2M ferri-/ferro-cyanide	55.6	69.8	91.1	1.59
	0.2M ferri-/ferro-cyanide in 0.8M KCl	61.4	64.5	93.1	1.50

Effect of Different SWNT Electrodes

Using the best electrolyte system studied (0.4M ferri-/ferro-cyanide), the performance of different SWNT electrodes was investigated. Purified laser produced SWNT, 'as received' HiPco SWNT, and purified HiPco SWNT were considered; where the purification was performed to remove metal impurities such as residual iron catalyst. All three types of SWNT electrodes considered generated similar linear trends of V_{oc} vs ΔT in 0.4M ferri-/ferro-cyanide. Their thermoelectric coefficients had values of 1.4 mV/^oK.

Comparison of the I_{sc} values obtained, however, shows that I_{sc} for purified HiPco SWNT electrodes > 'as received' HiPco SWNT electrodes > purified laser produced SWNT electrodes (Figure 3.6.6).
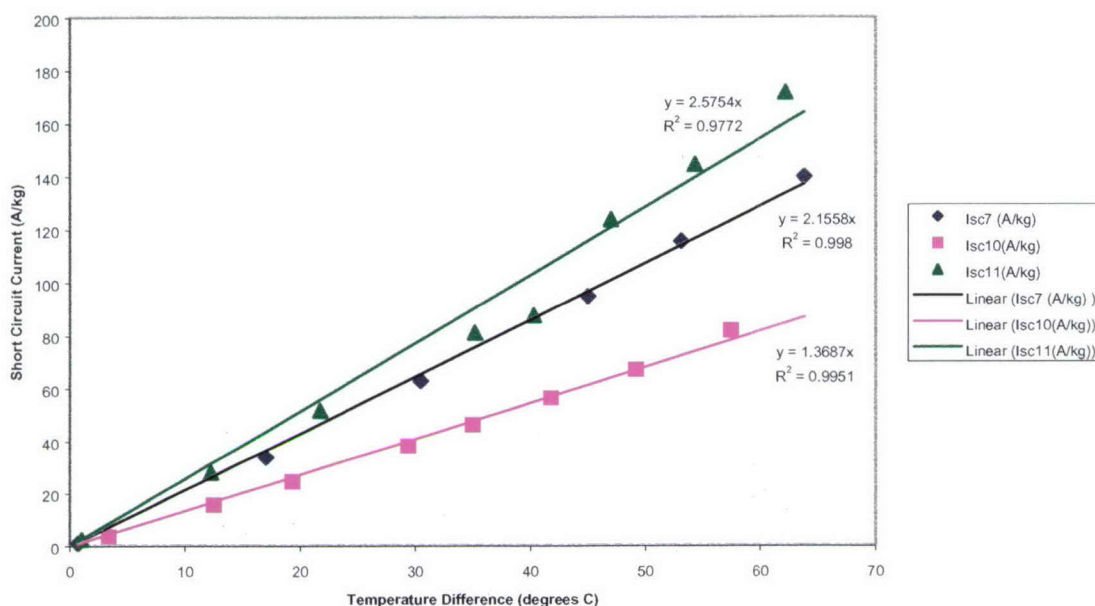
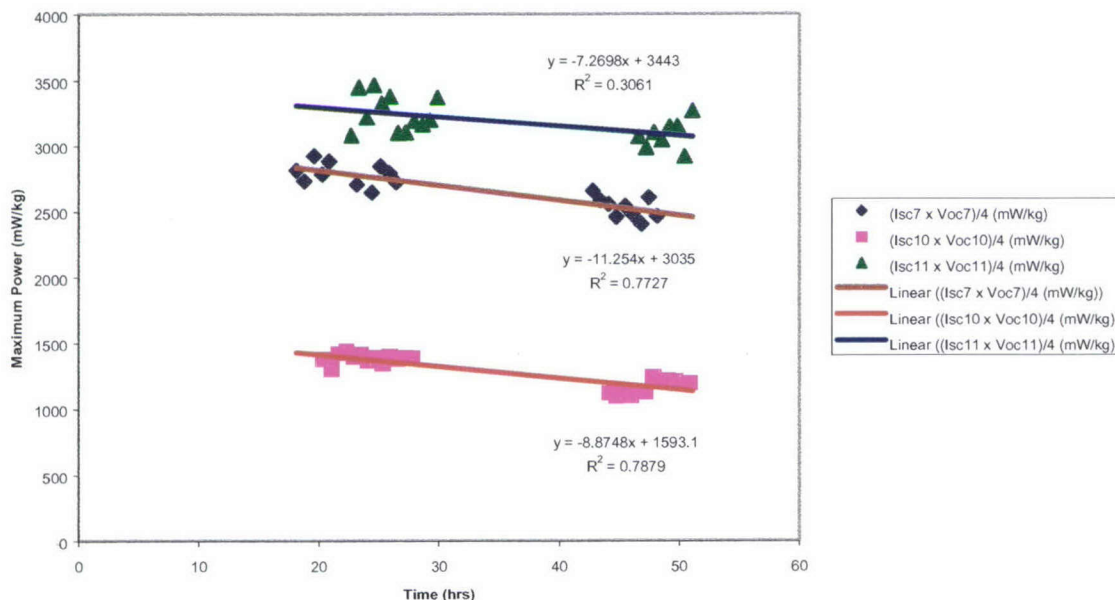**Figure 3.6.6.** Short Circuit Current vs Temperature Difference for SWNT Electrodes (7: 'as received' HiPco, 10: purified laser produced, 11: purified HiPco) in 0.4M Ferri-/Ferro-cyanide.

P_{max} for HiPco SWNT electrodes, purified or 'as received', was higher than for purified laser produced SWNT electrodes (Figure 3.6.7).

The results obtained over an extended period of operation are presented in Table 3.6.3. HiPco SWNT (purified or 'as received') electrodes generated more than double the P_{max} generated by purified laser produced SWNT electrodes.
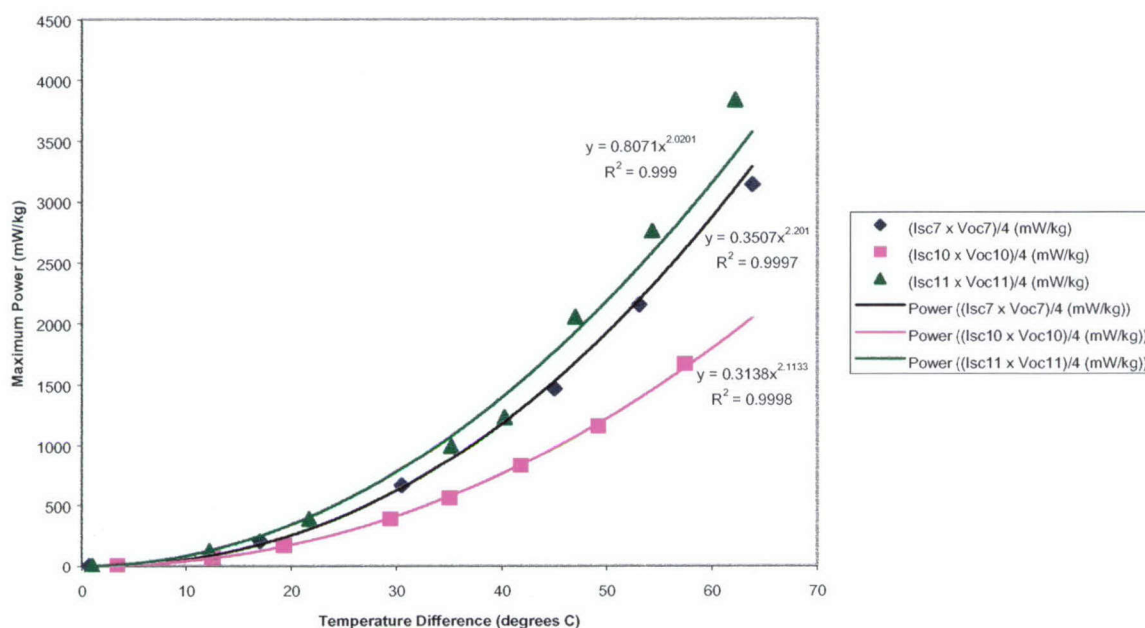
Figure 3.6.7. Maximum Power vs Temperature Difference for SWNT Electrodes (7: 'as received' HiPco, 10: purified laser produced, 11: purified HiPco) in 0.4M Ferri-/Ferro-cyanide.

Table 3.6.3. Thermoelectrochemical results obtained from different SWNT electrodes after several hours of operation at maximum temperature difference in 0.4M ferri-/ferro-cyanide.

Hours of operation	Type of SWNT electrode	Temperature difference (^{o}C)	V_{oc} (mV)	I_{sc} (A/kg)	Maximum Power ((I_{sc} x V_{oc})/4, W/kg)
17	Purified laser produced	57.9	75.5	75.4	1.42
	As received HiPco	63.5	85.9	136.0	2.92
	Purified HiPco	62.5	83.0	148.4	3.08
46	Purified laser produced	58.5	68.6	69.8	1.20
	As received HiPco	61.6	79.1	124.5	2.46
	Purified HiPco	63.3	81.4	152.0	3.09

It is also noticeable from Figure 3.6.8 that the power generated by purified laser produced SWNT and purified HiPco SWNT electrodes deteriorated less than for 'as received'

HiPco. It is obvious that the residual iron catalyst in the 'as received' HiPco SWNT electrodes did not improve the performance of the electrodes. It can be concluded that the thermoelectrochemical performance of SWNT electrodes is primarily a surface area phenomenon. Therefore, any factor that changes the surface area of the SWNT electrodes will affect their thermoelectrochemical performance.

Figure 3.6.8. Maximum Power vs Time for SWNT Electrodes (7: 'as received' HiPco, 10: purified laser produced, 11: purified HiPco) in 0.4 M Ferri-/Ferro-cyanide.

The electrons per carbon calculated from the charge generated by these SWNT electrodes in 0.4M ferri-/ferro-cyanide was an average of 1.

Further Investigations on the ferri-/ferro-cyanide system

The focus was on performing experiments that will elucidate the thermoelectrochemistry that is occurring at the hot anode where ferrocyanide is oxidized to ferricyanide. Cyclic voltammetry was run for "as received" HiPco SWNT electrode, as well as commercial glassy carbon electrode, in 0.4M ferri-/ferro-cyanide at various temperatures. Scan rates ranging from 10 mV/s to 100 mV/s were used. Typical cyclic voltammograms obtained
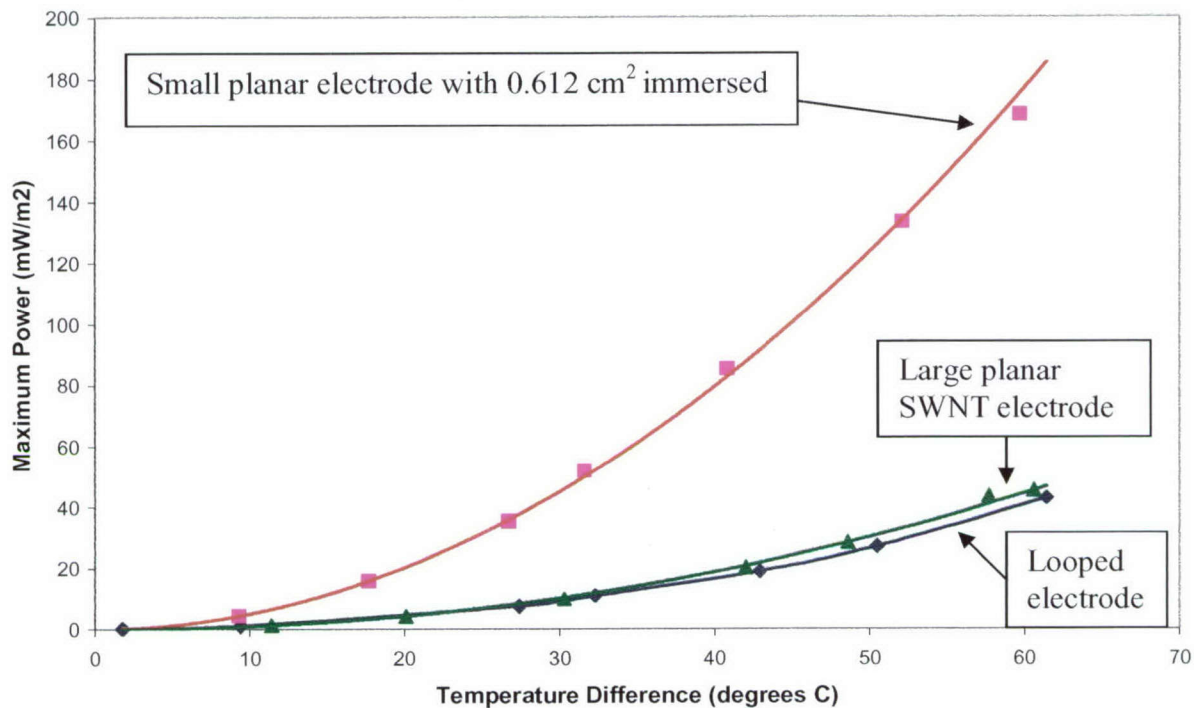
Figure 3.6.18. Comparison of Maximum Power Densities (mW/m^2) for 'as received' HiPco SWNT electrodes in different configurations.
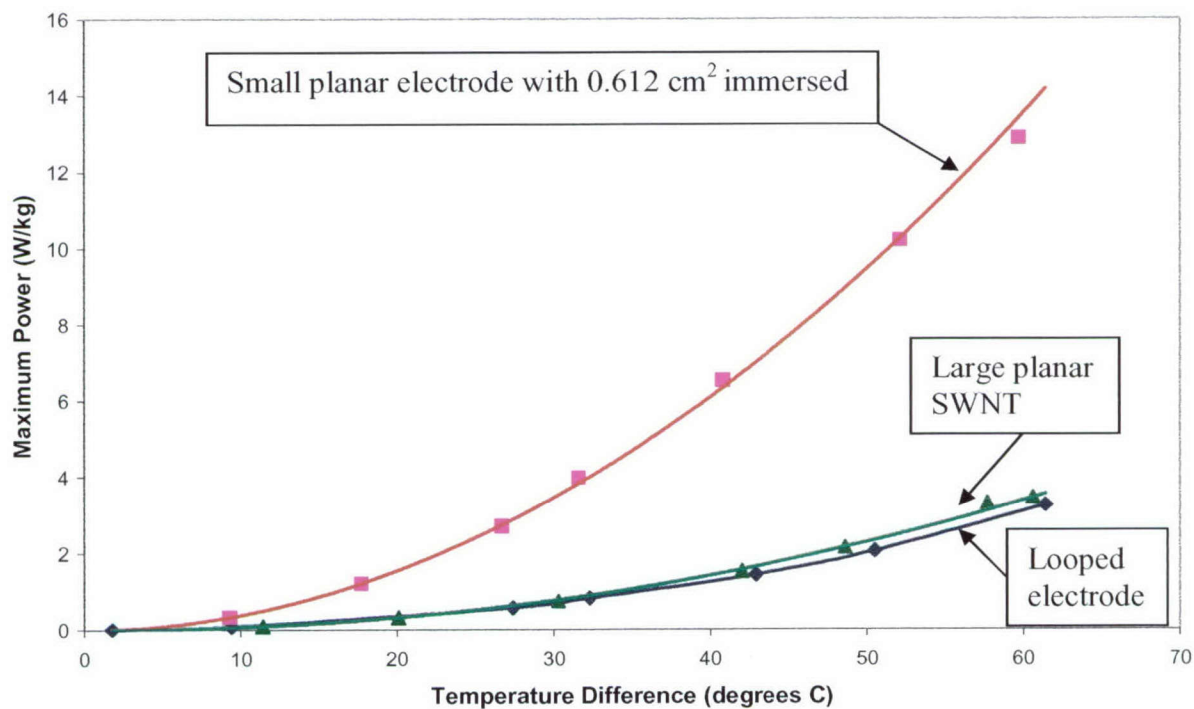
Figure 3.6.19. Comparison of Maximum Power Densities (W/kg) for 'as received' HiPco SWNT electrodes in different configurations.

Effect of Electrode Materials

Using the best electrolyte system studied (0.4M ferricyanide/0.4M ferrocyanide), the performance of different electrode materials was investigated. Purified laser produced SWNT, 'as received' HiPco SWNT, purified HiPco SWNT, Rinzler II SWNT, and Spectracarb 2225C activated carbon fabric electrodes were considered.

Most types of SWNT electrodes considered generated similar linear trends of open circuit voltage (V_{oc}) vs temperature difference (ΔT) in 0.4M ferricyanide/0.4M ferrocyanide. Their thermoelectric coefficients had values of 1.4 mV/^{o}C. The Rinzler II SWNT (from Edgar Munoz) and the Spectracarb electrode, however, had a slightly lower thermoelectric coefficient of 1.3 mV/^{o}C. De-oxygenation of the solution (by purging with nitrogen for 6 hours) and cell did not affect the V_{oc} obtainable.

Comparison of the short circuit current (I_{sc}) values obtained, however, shows that I_{sc} for Rinzler II SWNT > purified HiPco SWNT electrode > 'as received' HiPco SWNT electrode > purified laser produced SWNT electrode > Spectracarb 2225 series activated carbon fabric electrode (Fig. 3.6.20). SWNT electrodes produced I_{sc} values that were 2 to 5 times that produced by the Spectracarb activated carbon electrode. The 'as received' HiPco SWNT electrodes appear to produce 1.6 times higher I_{sc} when the solution and cell were de-oxygenated, but this result could be due to the use of different electrodes in the experiments.
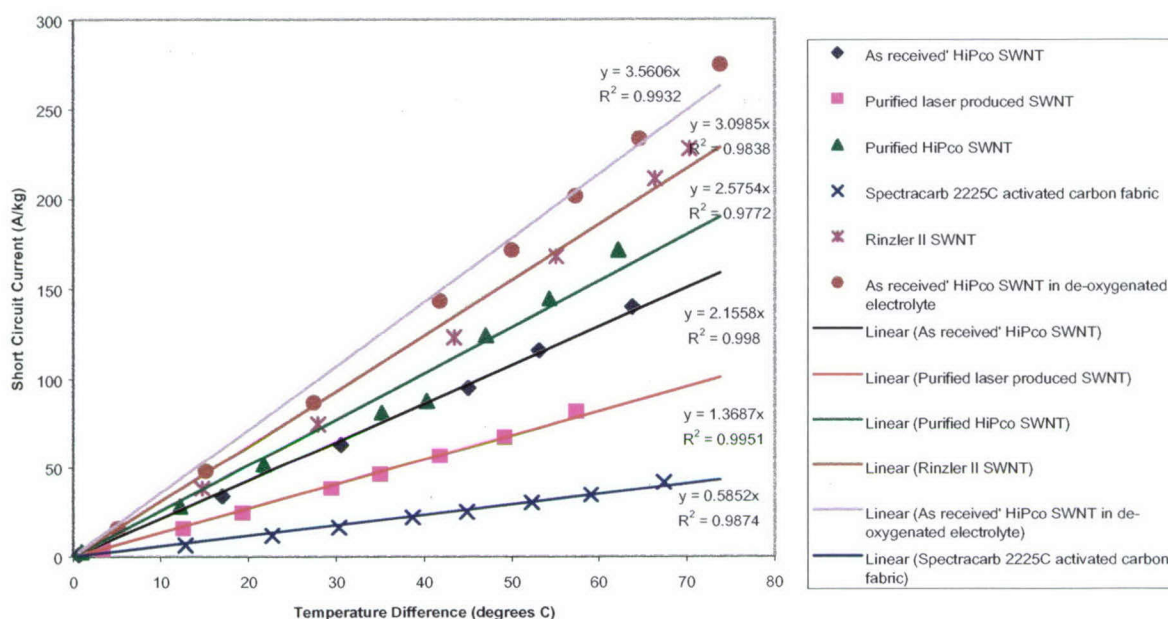
Figure 3.6.20. Short Circuit Current vs Temperature Difference for different electrode materials in 0.4M Ferri-/0.4M Ferro-cyanide.

Maximum power (P_{max}) for Rinzler II SWNT electrodes was higher than for HiPco SWNT electrodes (purified or 'as received') that was in turn higher than for purified laser produced SWNT electrodes that was, in turn, higher than for the Spectracarb electrodes (Fig. 3.6.21). P_{max} for SWNT electrodes were 2.5 to 5 times higher than for the Spectracarb electrode. The highest P_{max} was generated by the Rinzler II SWNT electrodes (5.5 W/kg at a ΔT of 70.3 ^{o}C). De-oxygenation of the solution and cell produced a higher P_{max} for 'as received' HiPco SWNT, but this may be due to the different electrodes used.
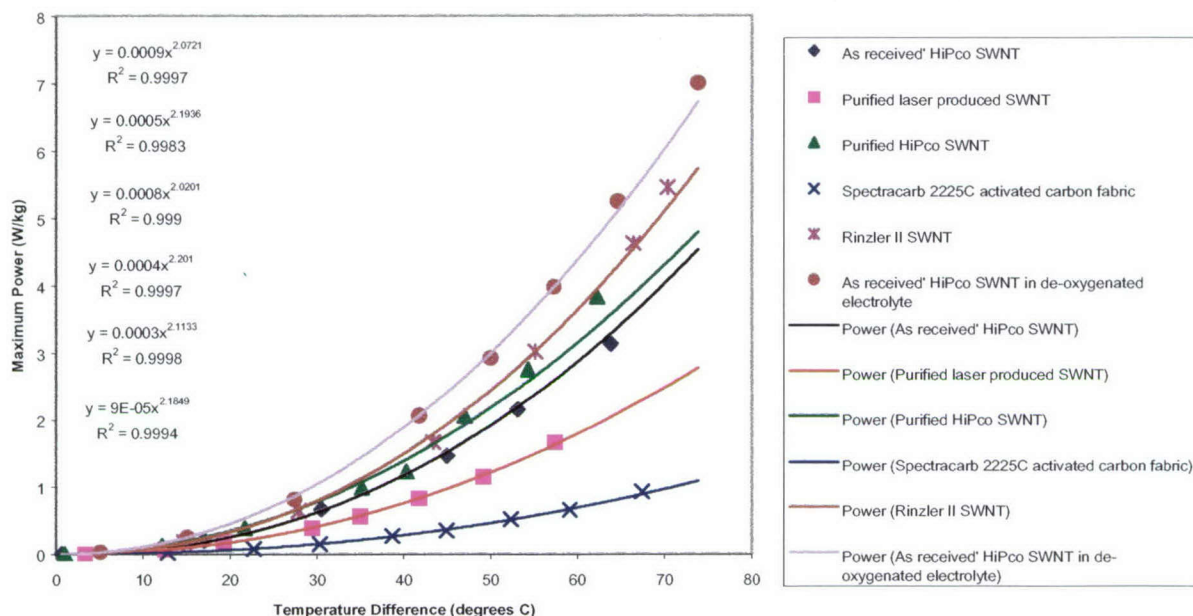
Figure 3.6.21. Maximum Power vs Temperature Difference for different electrode materials in 0.4M Ferri-/0.4M Ferro-cyanide.

The results obtained over an extended period of operation (Fig. 3.6.22) show that Rinzler II SWNT electrodes produced the highest P_{max} and HiPco SWNT (purified or 'as received') electrodes generated more than double the P_{max} generated by purified laser produced SWNT electrodes. It is also noticeable from Fig. 3.6.22 that the power generated by purified laser produced SWNT electrodes deteriorated less than that for other SWNT electrodes. It is obvious that the residual iron catalyst in the 'as received' HiPco SWNT electrodes had no significant effect on the performance of the electrodes. It can be concluded that the thermoelectrochemical performance of SWNT electrodes is primarily a surface area phenomenon. Therefore, any factor that changes the surface area of the SWNT electrodes will affect their thermoelectrochemical performance. On the other hand, comparison of the performance of SWNT electrodes with the Spectracarb 2225C activated carbon fabric electrode shows that SWNT electrodes generate 2 to 5 times the power generated by the Spectracarb electrode; even though the Spectracarb probably has 8 times the BET surface area of SWNT electrodes per gram.

107

The deterioration in performance over time is not ameliorated by de-oxygenation of the solution and cell. The rust colored precipitate produced when the cell is operated over an extended period is inherently due to the instability of the ferricyanide/ferrocyanide electrolyte at high temperatures because the precipitate was also obtained when the cell was operated *without any electrodes* at a temperature difference of 72 $^\circ$C (hot side was 93.6 $^\circ$C and cold side was 21.6 $^\circ$C) for 21 hours. This result also suggests that the power generated by SWNT electrodes is due to the thermoelectrochemical phenomenon.
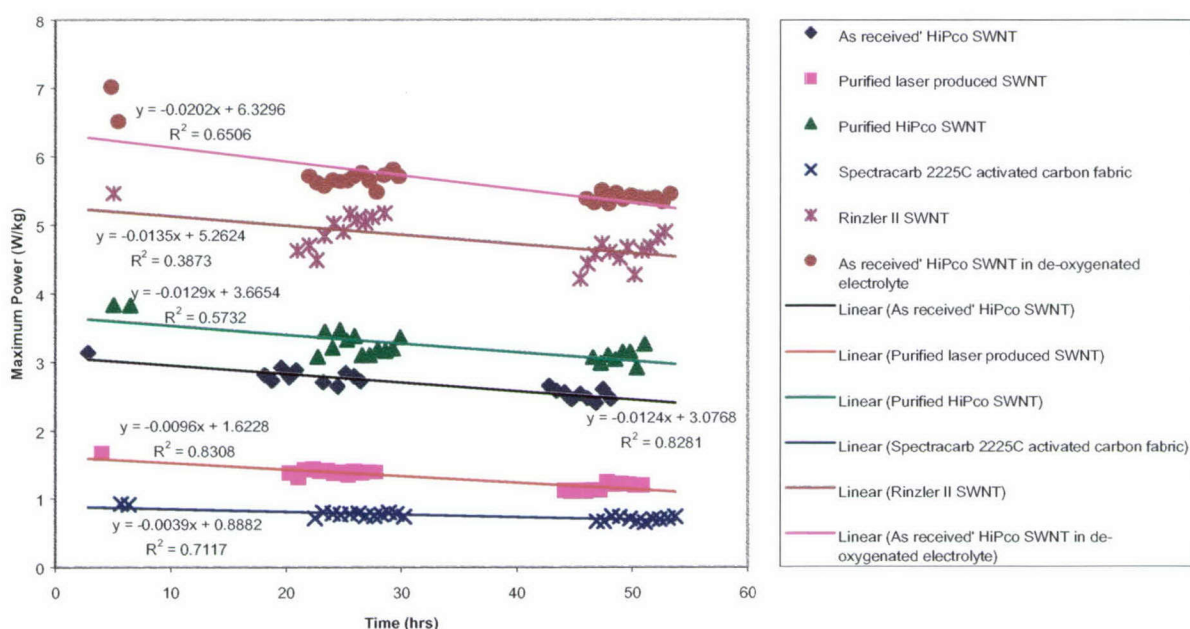
Figure 3.6.22. Maximum Power vs Time for different electrode materials in 0.4M Ferri-/0.4M Ferro-cyanide.

Extremely exciting results, however, were obtained by Sergey Li when he ran a thermoelectrochemical experiment in 0.4M ferri-/0.4M ferro-cyanide using Rinzler II buckypaper from Edgar Munoz. As can be seen from Figure 3.6.23, 388 A/kg short circuit current and 116 mV open circuit voltage were obtained for a temperature difference of 68 $^\circ$C. This short circuit current is at least 2X that previously obtained from other electrode materials by Chee Too, and the open circuit voltage is about 30% higher.

108
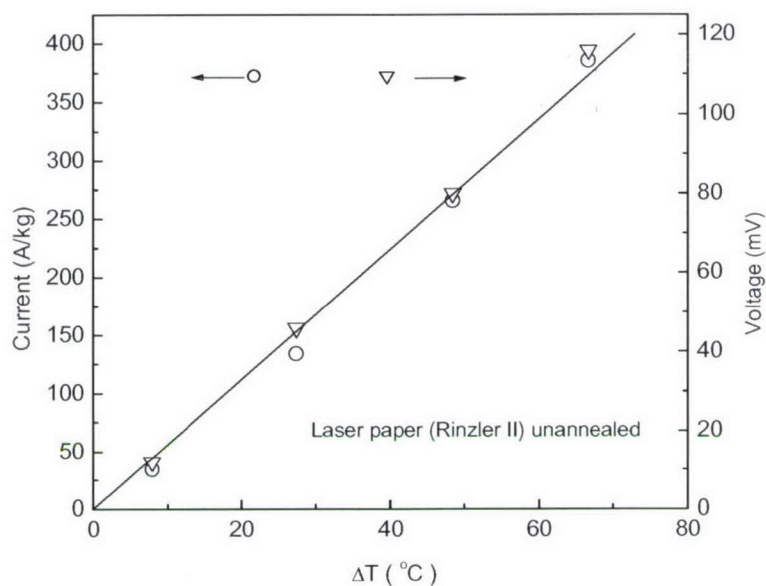
Figure 3.6.23. Short-circuit current and open-circuit voltage as a function of temperature difference between anode and cathode.

Consequently, a high maximum power of 11 W/kg at a temperature difference of 68 $^{\circ}$C was obtained (Fig. 3.6.24). This maximum power is double that obtained by Chee Too with Rinzler II buckypaper and much higher than results obtained from other materials by Chee Too. The Rinzler II buckypaper used by Sergey Li was from a different batch to that used by Chee Too; although both buckypapers were fabricated by Edgar Munoz.
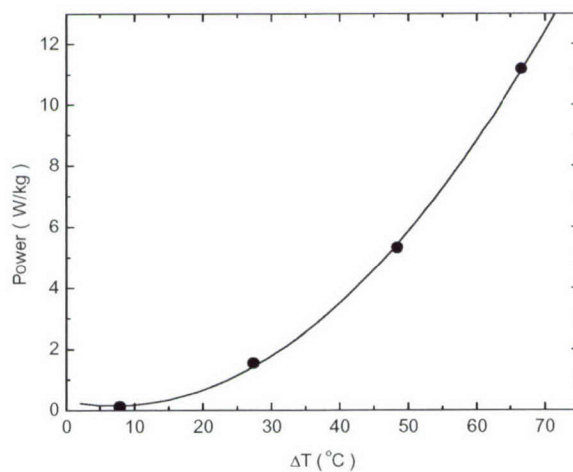
Figure 3.6.24. Power of thermocell as a function of temperature difference between anode and cathode.

Effect of Electrode Size on Thermoelectrochemical Performance

Initial investigations into stacking of SWNT electrodes to produce more power using aqueous 0.4M ferri-/0.4M ferro-cyanide showed that, for electrodes of 5.67 cm^2 geometric area, two electrodes separated with a spacer of hard filter paper produced similar Open Circuit Voltages and total Short Circuit Currents as for a single electrode. Therefore further work was directed at investigating the effects of electrode thickness and electrode geometric area on thermal energy harvesting.

Electrodes of similar geometric areas (5.67 cm^2) but with a range of thicknesses were compared for performance. The Open Circuit Voltages (100 mV for ΔT of 70 $^{\circ}$C) and absolute Short Circuit Currents (1.3 mA for ΔT of 70 $^{\circ}$C) obtained were similar regardless of the thickness. Consequently, when the mass of the electrodes are taken into account (Fig. 3.6.25), the thinner electrodes produced higher Short Circuit Current Densities (160 A/kg for a temperature difference of 70 $^{\circ}$C).
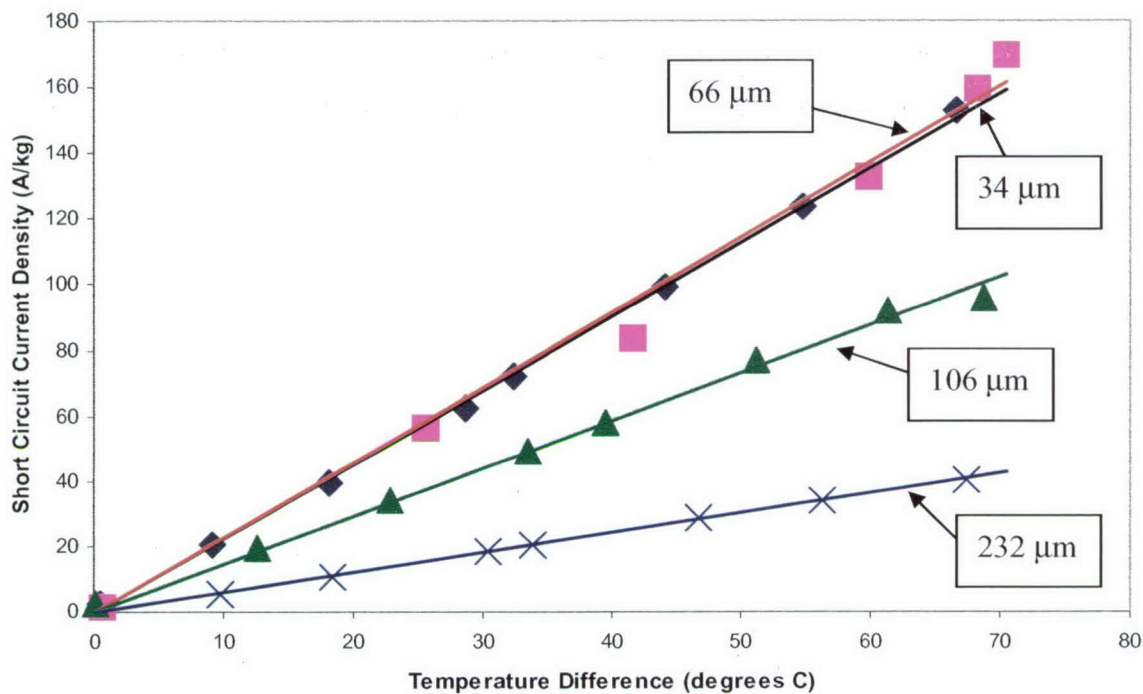
Figure 3.6.25. Short Circuit Current Density obtained at 'as received' HiPco SWNT Electrodes of Different Thicknesses (34 μm, 66 μm, 106 μm and 232 μm).

From the thickness results it was concluded that the electrode/electrolyte system in the cell might be saturated and so smaller electrodes were considered. Electrode geometric areas ranging from 0.612 cm^2 to 5.67 cm^2 were investigated. As expected, the Open Circuit Voltages were similar (90 mV for ΔT of 67 ^{o}C).

The Short Circuit Current Density, whether expressed as A/m^2 or A/kg (Fig. 3.6.26 and Fig 3.6.27 respectively), improved as the electrode size was reduced. Consequently, the Maximum Power Density, whether expressed as mW/m^2 or W/kg (Fig. 3.6.28 and Fig 3.6.29 respectively), also improved as the electrode geometric area was diminished. It is notable that, with the 1.12 cm^2 or 0.612 cm^2 electrode, the Maximum Power Density generated was 13-14 W/kg at a temperature difference of 60-66 ^{o}C.

All the experiments were performed with the cold cathode maintained at room temperature (18 – 22 ^{o}C) with cold tap water flowing through the condenser.
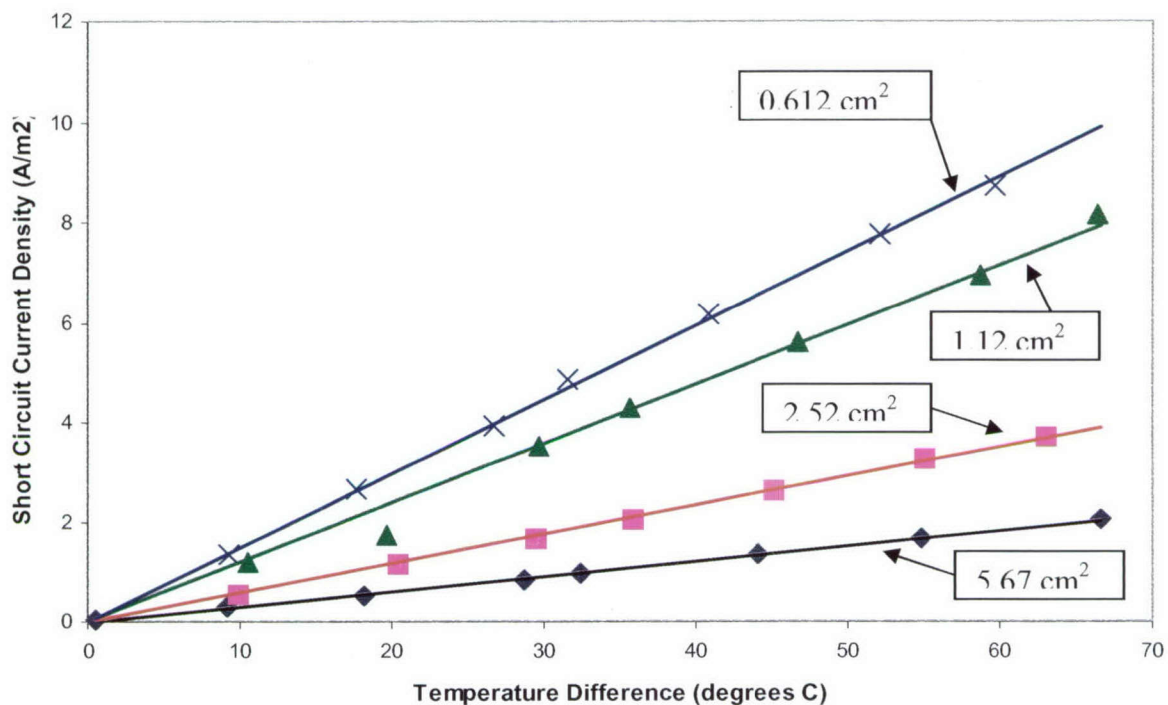
Figure 3.6.26. Comparison of Short Circuit Current Density (A/m^2) obtained from HiPco SWNT Electrodes of Different Geometric Areas (5.67, 2.52, 1.12, 0.612 cm^2).
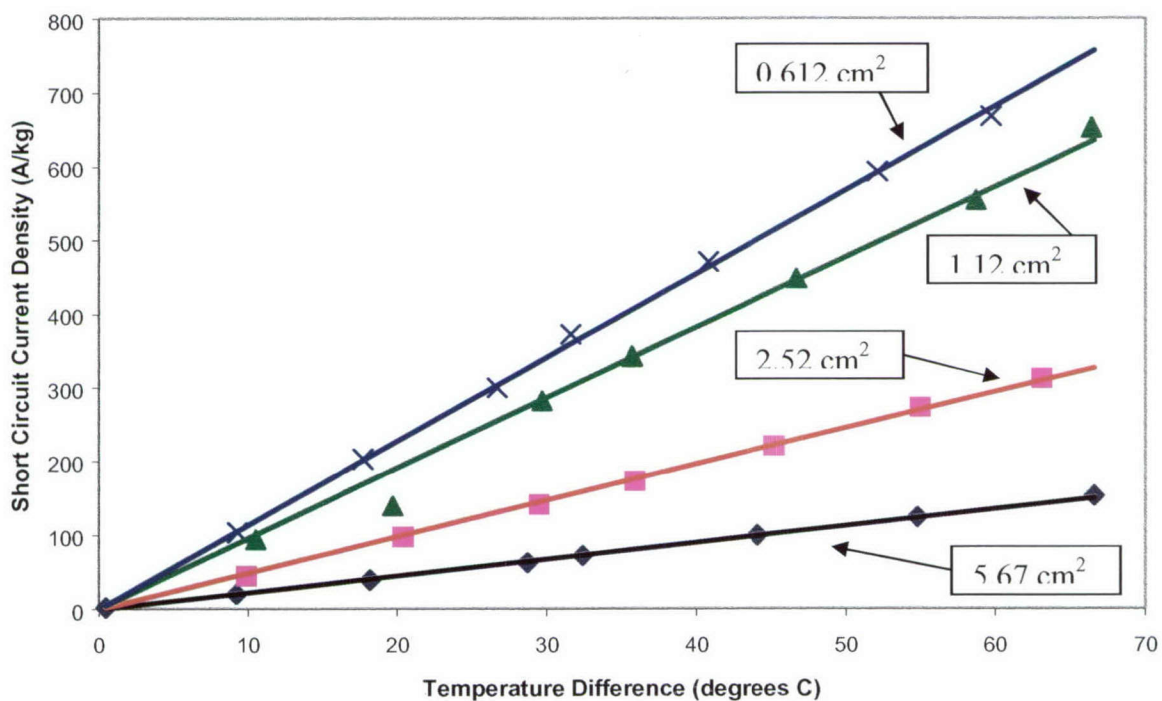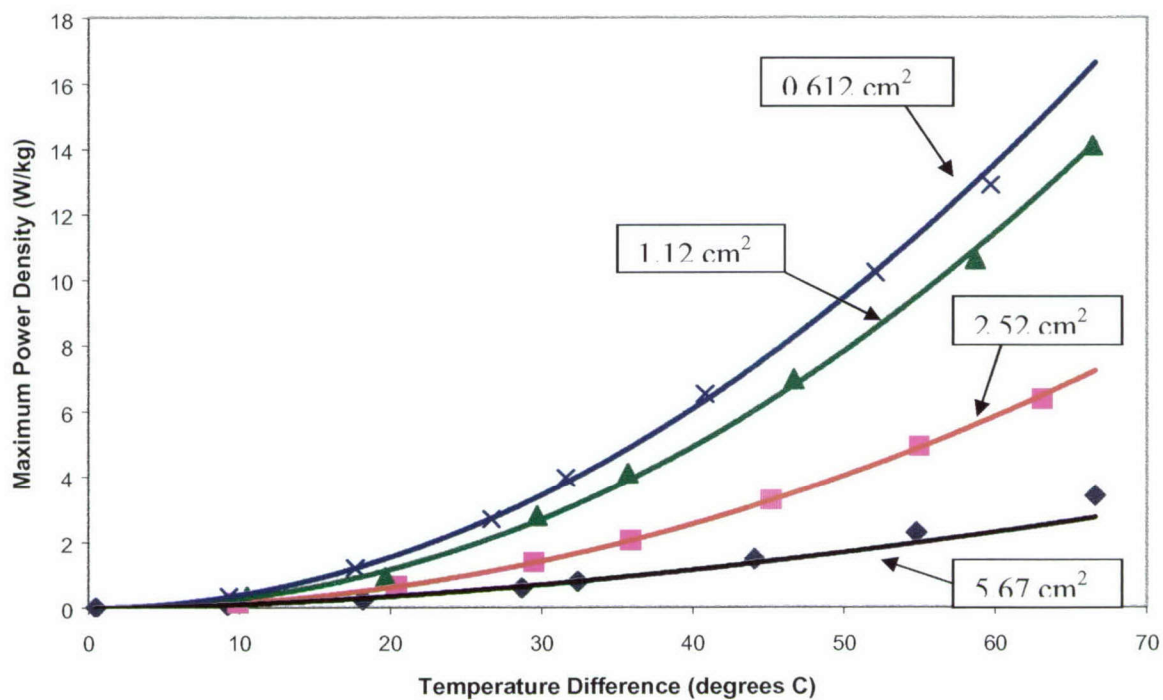

Figure 3.6.27. Comparison of Short Circuit Current Density (A/kg) obtained from HiPco SWNT Electrodes of Different Geometric Areas (5.67, 2.52, 1.12, 0.612 cm^2).
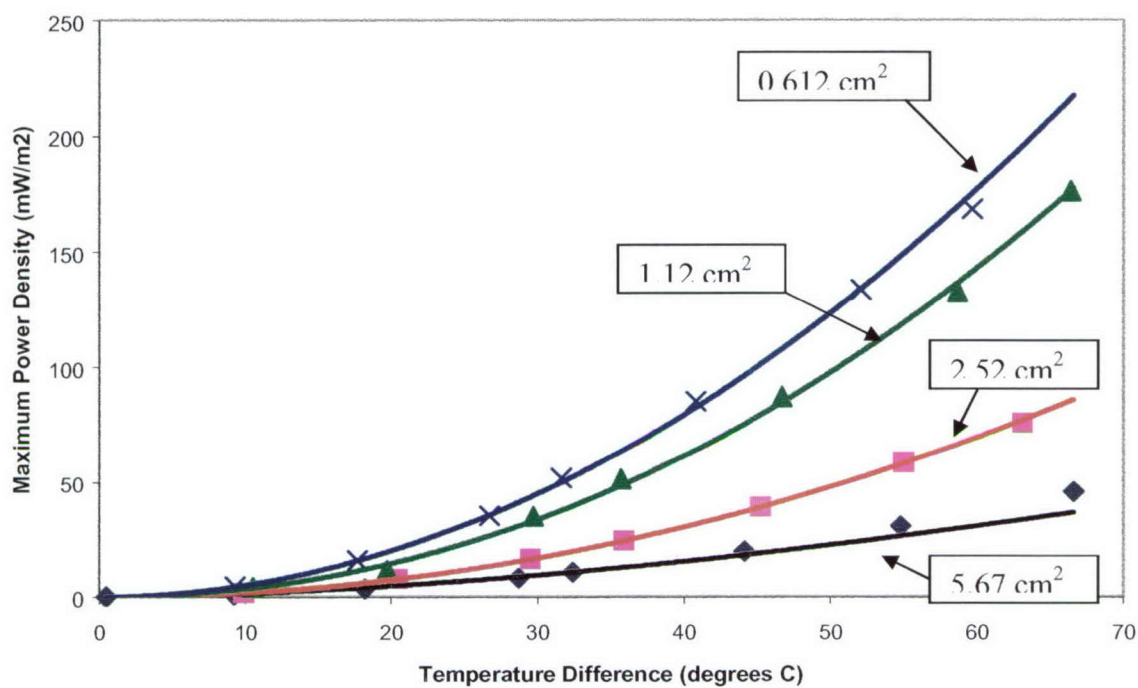
Figure 3.6.28. Comparison of Maximum Power Density (mW/m^2) obtained from HiPco SWNT Electrodes of Different Geometric Areas (5.67, 2.52, 1.12, 0.612 cm^2).

Figure 3.6.29. Comparison of Maximum Power Density (W/kg) obtained from HiPco SWNT Electrodes of Different Geometric Areas (5.67, 2.52, 1.12, 0.612 cm^2).

113

Attention was then turned towards a novel method of obtaining very thin layers of HiPco SWNT on platinized PVDF (polyvinylidene fluoride) membranes (0.22 μm pore size). Platinization of PVDF membranes was achieved by sputter coating a thin (90-100 nm) layer of Pt onto the PVDF. These Pt/PVDF membranes were then used to filter HiPco SWNT dispersions under 400 kPa nitrogen gas pressures. In this way, a thin (19 μm) adherent layer of HiPco SWNT can be obtained on the Pt side of the Pt/PVDF membrane.

Initial tests were done using the Pt/PVDF as electrodes. Different configurations of the Pt/PVDF were investigated while maintaining the total geometric area at 0.54 cm^2. Thus the Pt/PVDF electrodes were configured as a single piece, or the same piece slit into two pieces but facing in the same direction, or the two pieces with the Pt surface facing in opposite directions. The results show that similar Open Circuit Voltages were obtained (100 mV for ΔT of 70 ^{o}C), similar Short Circuit Currents (0.8 mA for ΔT of 70 ^{o}C) and Short Circuit Current Densities (Figure 3.6.30) were obtained. Consequently, the Maximum Power Densities obtained were also similar (Figure 3.6.31). Therefore it can be concluded that these types of electrode configuration in this cell do not alter the performance of the thermocell.
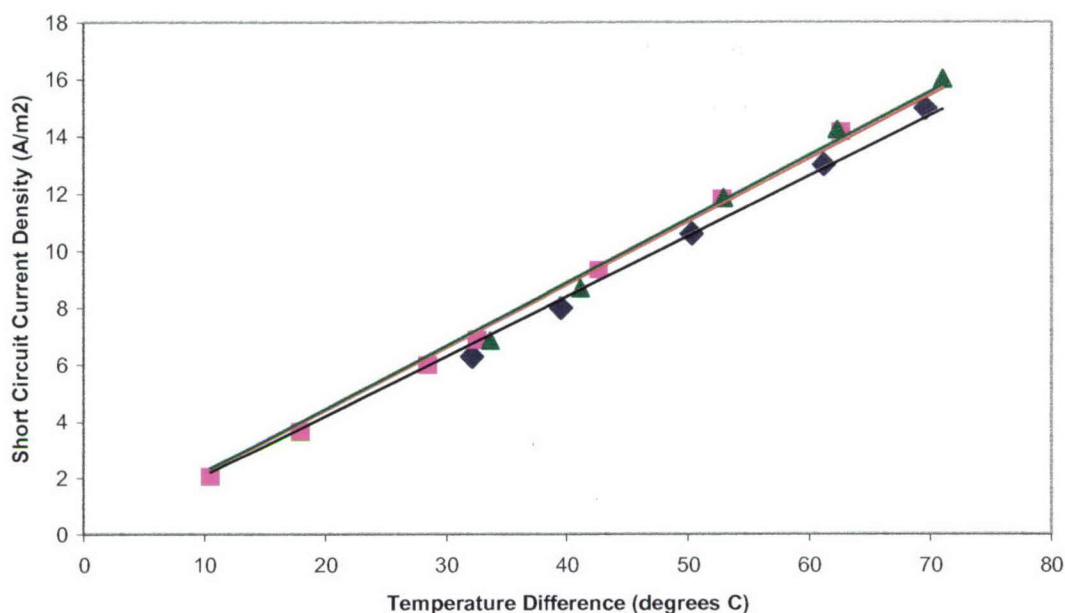
Figure 3.6.30. Comparison of Short Circuit Current Densities obtained from Different Configurations of Pt/PVDF in 0.4M Ferri-/0.4M Ferro-cyanide. The Pt/PVDF electrodes were configured as a single piece, or the same piece slit into two pieces but facing in the same direction, or the two pieces with the Pt surface facing in opposite directions.
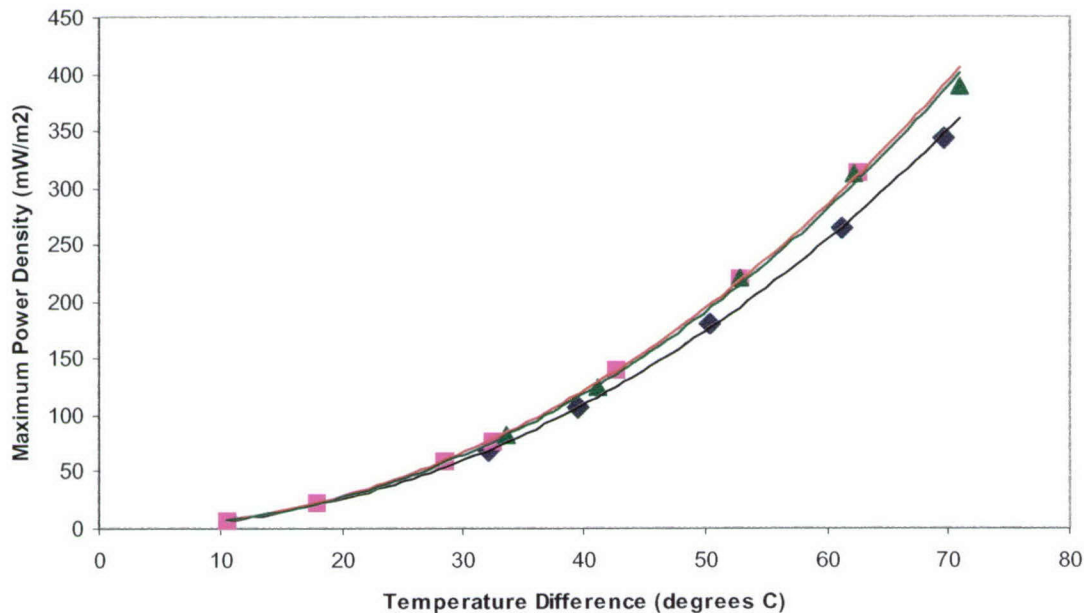
Figure 3.6.31. Comparison of Maximum Power Densities obtained from Different Configurations of Pt/PVDF in 0.4M Ferri-/0.4M Ferro-cyanide. The Pt/PVDF electrodes were configured as a single piece, or the same piece slit into two pieces but facing in the same direction, or the two pieces with the Pt surface facing in opposite directions.

115

Subsequently, HiPco SWNTs on platinized PVDF membranes were investigated for their thermal energy harvesting capabilities. Their performance was compared to bare Pt/PVDF. The geometric area of the two types of electrodes was maintained at 0.34 cm^2. The two types of electrodes were tested individually as well as together. The results show that the Open Circuit Voltages (90 mV for ΔT of 67 ^{o}C) were similar irrespective of the type of electrodes or whether they were combined or individual. Figure 3.6.32 shows that the Pt/PVDF produced higher Short Circuit Currents than the SWNT/Pt/PVDF; although when the two types of electrodes were combined they produced the highest currents (as would be expected from the higher total area of the two electrodes). When normalized to geometric area, however, the Pt/PVDF produced higher Short Circuit Current Densities than the SWNT/Pt/PVDF that, in turn, produced higher Short Circuit Current Densities than the combination of the two types of electrodes (Figure 3.6.33). Maximum Power Density produced by Pt/PVDF was the highest (Figure 3.6.34).

If only the SWNT layer is considered, which had an estimated weight of 0.1124 mg, then the Short Circuit Current Density obtained is 3784 A/kg and the Maximum Power Density obtained is 83 W/kg for a temperature difference of 65 ^{o}C. These results far exceed this year's (Year 2) goal of 800 A/kg by over four fold.
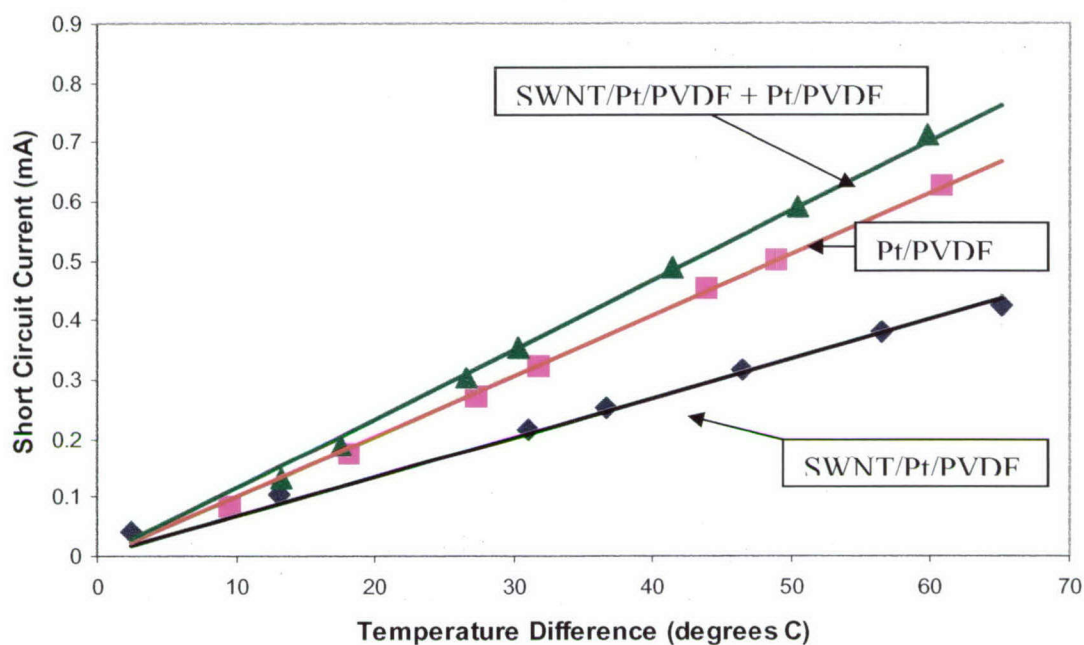
Figure 3.6.32. Comparison of Short Circuit Current obtained from SWNT/Pt/PVDF, Pt/PVDF, and SWNT/Pt/PVDF + Pt/PVDF in 0.4M Ferri-/0.4M Ferro-cyanide/H_2O. Geometric areas: 0.34 cm^2, 0.34 cm^2, 0.34 cm^2 + 0.34 cm^2 respectively.
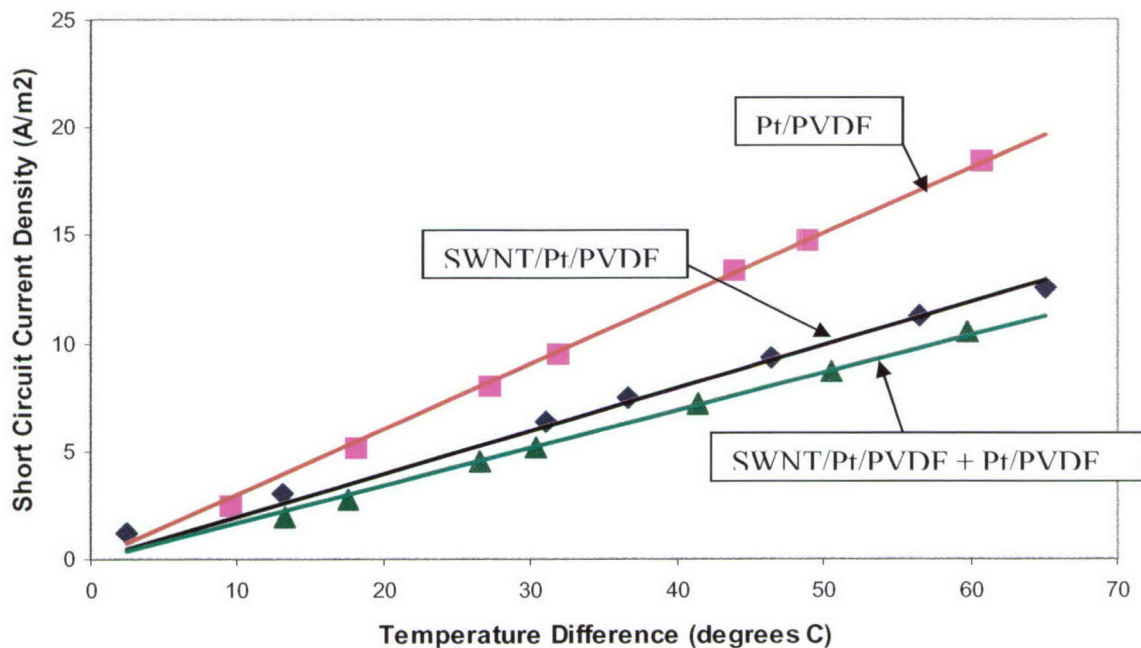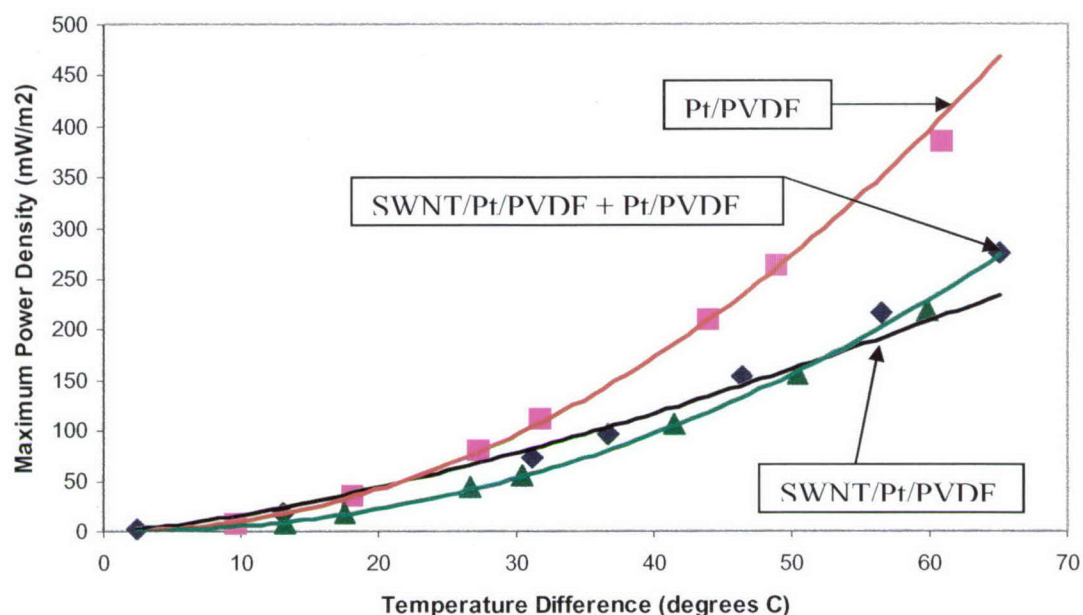

Figure 3.6.33. Comparison of Short Circuit Current Density (A/m^2) obtained from SWNT/Pt/PVDF, Pt/PVDF and SWNT/Pt/PVDF + Pt/PVDF Electrodes in 0.4M Ferri-/0.4M Ferro-cyanide/H_2O. Geometric areas: 0.34 cm^2, 0.34 cm^2, 0.34 cm^2 + 0.34 cm^2 respectively.

Figure 3.6.34. Comparison of Maximum Power Density (mW/m^2) obtained from SWNT/Pt/PVDF, Pt/PVDF and SWNT/Pt/PVDF + Pt/PVDF in 0.4M Ferri-/0.4M Ferro-cyanide/H$_2$O. Geometric areas: 0.34 cm^2, 0.34 cm^2, 0.34 cm^2 + 0.34 cm^2 respectively.

Effect of Inter-Electrode Distance

Inter-electrode distances of 0.5 cm, 1.0 cm, 2.0 cm, 4.0 cm, 6.0 cm, 8.0 cm and 10.0 cm were considered. The aqueous electrolyte used for these tests was 0.4 M ferricyanide/0.4 M ferrocyanide. The difficulties encountered include the difficulty in keeping the cold side cool whilst increasing the temperature of the hot side. Thus, the cold side temperature was as high as nearly 50 ^{o}C when the hot side was 91 ^{o}C.

Figure 3.6.35 shows that the highest Open Circuit Voltage (V$_{oc}$) was obtained when the inter-electrode distance was 6.0 cm and the lowest result was at a distance of 0.5 cm. For example, for a temperature difference of 40 ^{o}C, the V$_{oc}$ was 30 mV when the inter-electrode distance was 6.0 cm compared with 20 mV at a distance of 0.5 cm.
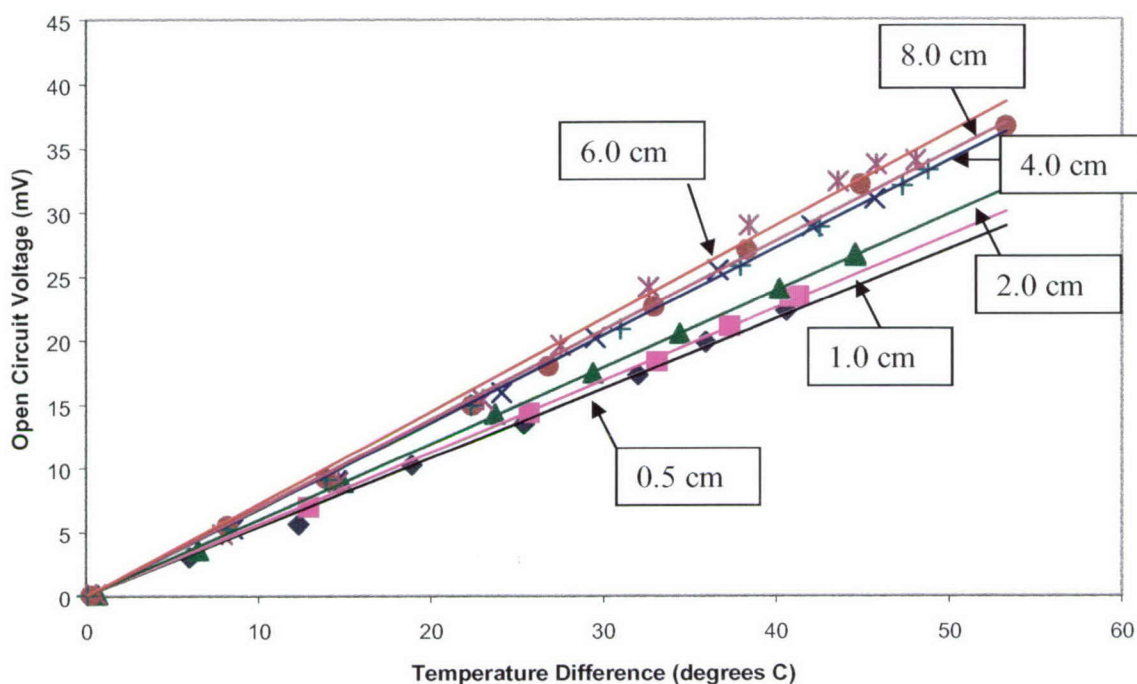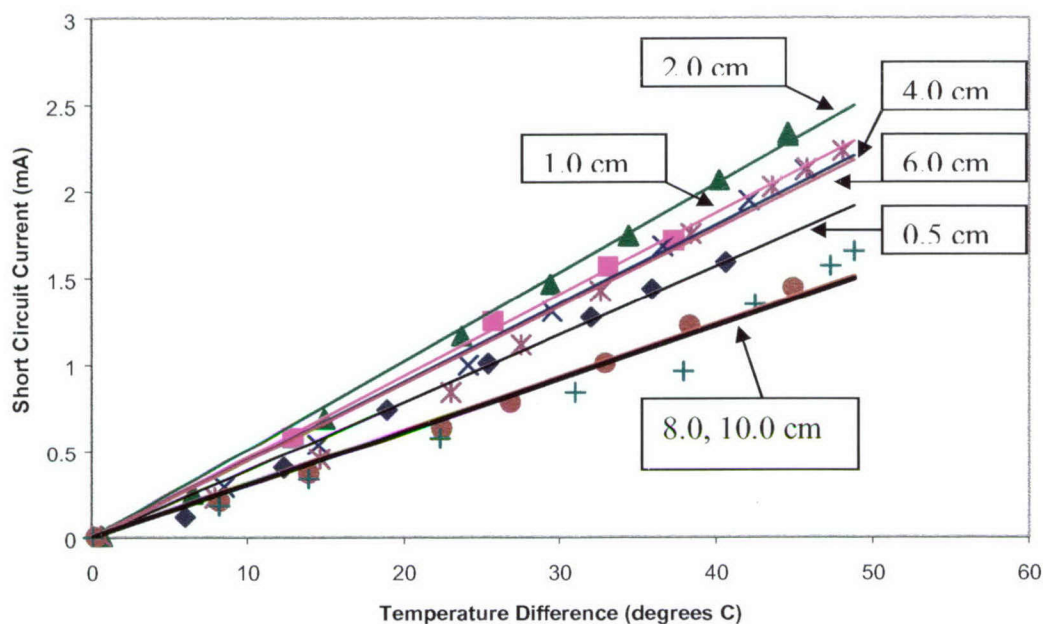
Figure 3.6.35. Comparison of Open Circuit Voltages obtained from HiPco SWNT Electrodes at Different Inter-electrode Distances in 0.4M Ferri-/0.4M Ferro-cyanide/H_2O Electrolyte. Inter-electrode distances were 0.5 cm, 1.0 cm, 2.0 cm, 4.0 cm, 6.0 cm, 8.0 cm and 10.0 cm.
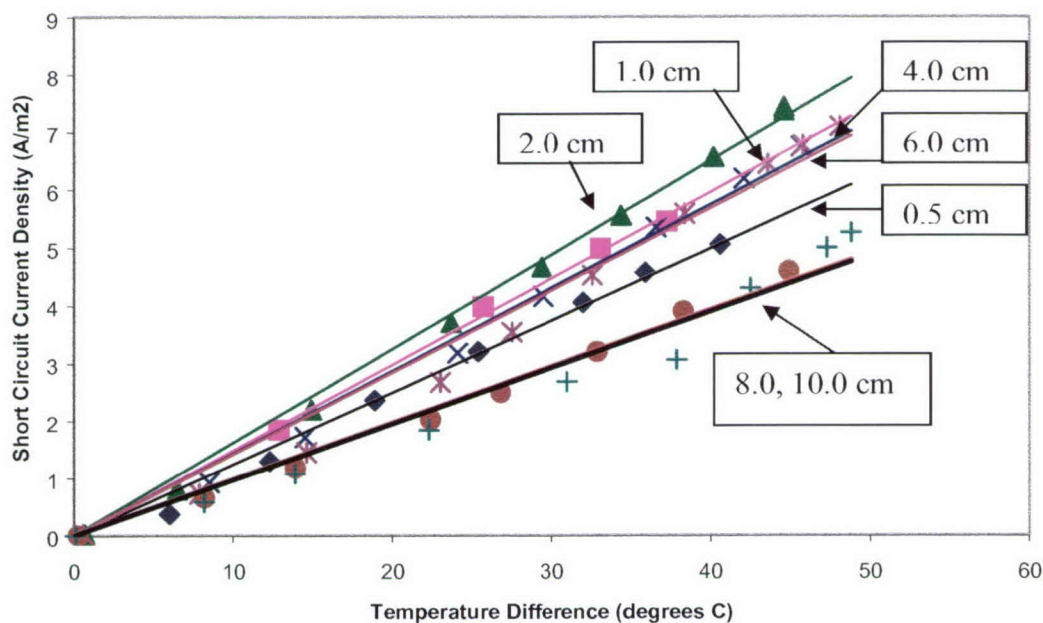
Comparison of Short Circuit Currents (Figure 3.6.36) shows that the highest result was obtained at an inter-electrode distance of 2.0 cm and the lowest at 8.0 to 10.0 cm. For example, for a temperature difference of 40 $^{\circ}$C, Short Circuit Current Density was 6.5 A m^{-2} at a distance of 2.0 cm compared with 4 A m^{-2} at 8.0 to 10.0 cm distance (Figure 3.6.37).

When normalized to unit weight, the results show that at an inter-electrode distance of 2.0 cm the Short Circuit Current Density can be as high as 700 A/kg for a 45 $^{\circ}$C temperature difference (Figure 3.6.38). The results were highest at a distance of 2.0 cm and the lowest at a distance of 8.0 cm.

Figure 3.6.36. Comparison of Short Circuit Currents obtained from HiPco SWNT Electrodes at Different Inter-electrode Distances in 0.4M Ferri-/0.4M Ferro-cyanide/H$_2$O Electrolyte. Inter-electrode distances were 0.5 cm, 1.0 cm, 2.0 cm, 4.0 cm, 6.0 cm, 8.0 cm and 10.0 cm.
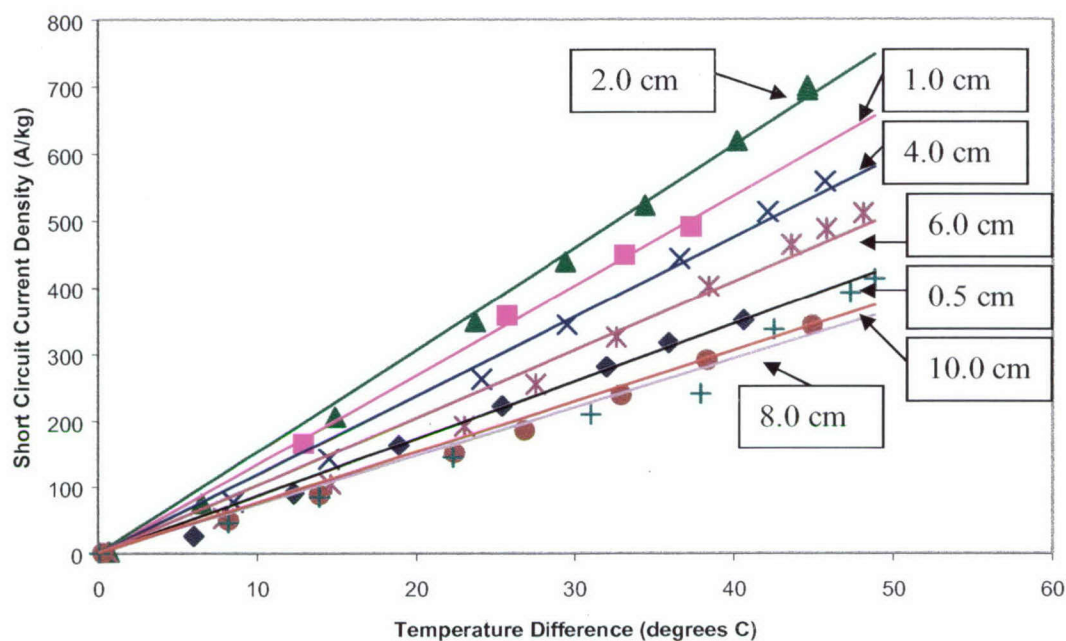

Figure 3.6.37. Comparison of Short Circuit Current Densities (A/m^2) obtained from HiPco SWNT Electrodes at Different Inter-electrode Distances in 0.4M Ferri-/0.4M Ferro-cyanide/H$_2$O Electrolyte. Inter-electrode distances were 0.5 cm, 1.0 cm, 2.0 cm, 4.0 cm, 6.0 cm, 8.0 cm and 10.0 cm.

Figure 3.6.38. Comparison of Short Circuit Current Densities (A/kg) obtained from HiPco SWNT Electrodes at Different Inter-electrode Distances in 0.4M Ferri-/0.4M Ferro-cyanide/H_2O Electrolyte. Inter-electrode distances were 0.5 cm, 1.0 cm, 2.0 cm, 4.0 cm, 6.0 cm, 8.0 cm and 10.0 cm.

The results for Maximum Power Density, expressed as mW/m^2, show that best results were obtained with an inter-electrode distance of 6.0 cm, and the worst results at 8.0-10.0 cm (Figure 3.6.39). However, when Maximum Power Density is expressed as W/kg the best results were obtained at an inter-electrode distance of 2.0 cm and the worst at 8.0-10.0 cm (Figure 3.6.40). For a temperature difference of 40 ^{o}C, the best Maximum Power Density obtained was either 40 mW/m^2 at an inter-electrode distance of 6.0 cm, or 3.5 W/kg at an inter-electrode distance of 2.0 cm.

The general conclusion that can be drawn from these results is that moving the electrodes closer together increases the Short Circuit Current (SCC) because there is less ohmic drop. However, the closer the electrodes are to each other, the harder it is to maintain a high temperature difference because of more efficient heat transfer from the hot side to the cold side, and this affects the Open Circuit Voltage (OCV). Therefore, the results show highest SCC at an inter-electrode distance of 2.0 cm but highest OCV at 6.0 cm.
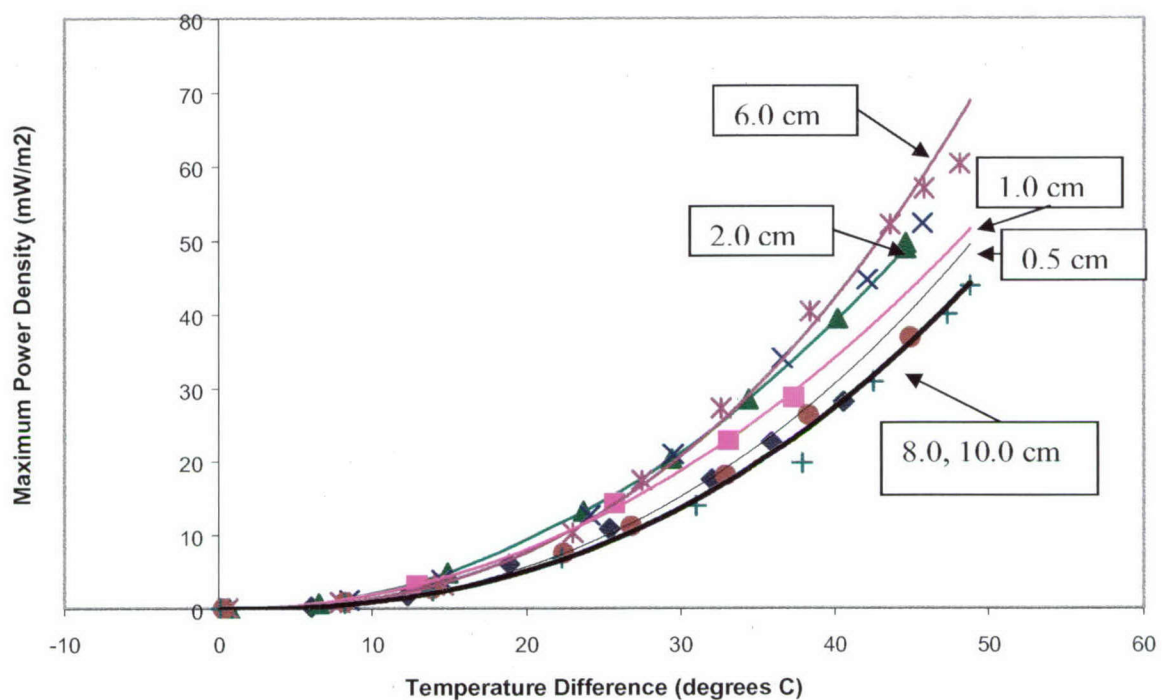
Figure 3.6.39. Comparison of Maximum Power Densities (mW/m²) obtained from HiPco SWNT Electrodes at Different Inter-electrode Distances in 0.4M Ferri-/0.4M Ferro-cyanide/H₂O Electrolyte. Inter-electrode distances were 0.5 cm, 1.0 cm, 2.0 cm, 4.0 cm, 6.0 cm, 8.0 cm and 10.0 cm.
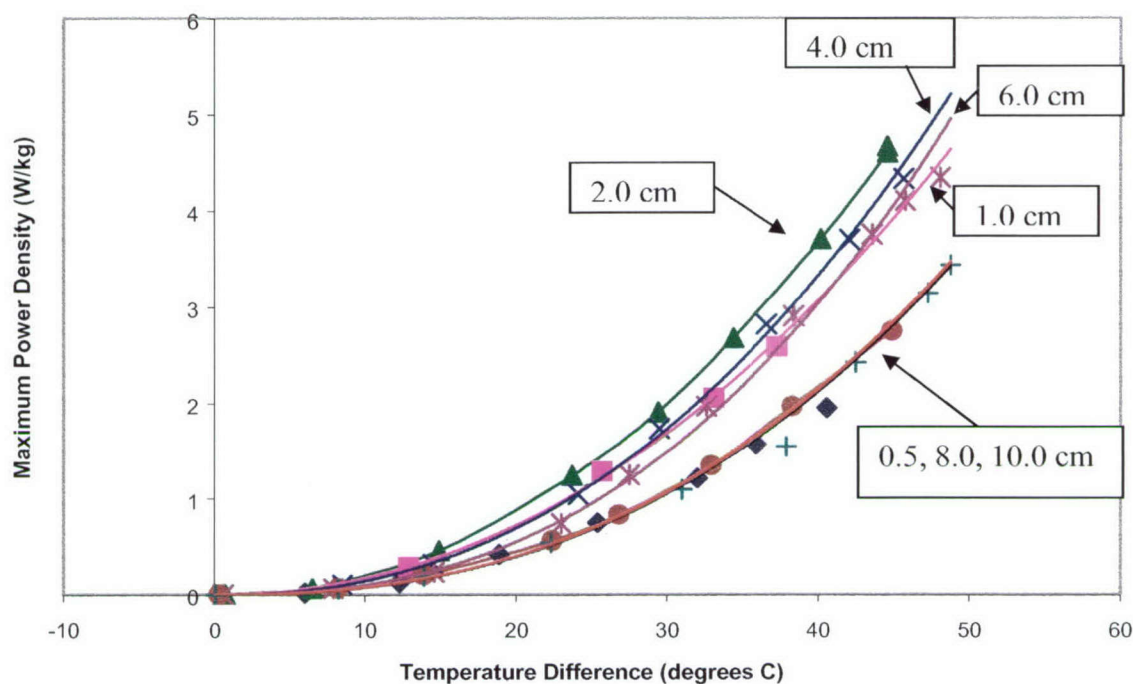
Figure 3.6.40. Comparison of Maximum Power Densities (W/kg) obtained from HiPco SWNT Electrodes at Different Inter-electrode Distances in 0.4M Ferri-/0.4M Ferro-cyanide/H_2O Electrolyte. Inter-electrode distances were 0.5 cm, 1.0 cm, 2.0 cm, 4.0 cm, 6.0 cm, 8.0 cm and 10.0 cm.

Thermal Energy Harvesting Using MWNT Electrodes

The MWNTs were synthesized by thermal chemical vapor deposition (CVD) operated at atmospheric pressure. The thin iron films (10 nm) were evaporated on Si wafer by electron beam evaporation and acted as the catalyst for the growth of carbon nanotubes. By controlling the thickness of iron films, the temperature of CVD, and the growth processes, we obtained the super-aligned MWNTs. The length of the tubes is a few hundreds micrometers, the diameter is nearly monodispersed around 10 nm with very small distribution, the wall of the tubes has 10 highly ordered graphitic layers in most cases, as confirmed by TEM imaging. The SEMs of MWNT mats used for thermoelectrochemistry experiments are shown in Fig. 3.6.41.

The thermal energy harvesting results obtained using MWNT mats at an inter-electrode distance of 10 cm in 0.4 M ferri-/0.4M ferro-cyanide are shown in Fig. 3.6.42. A short

123

circuit current density of 665 A/kg and open circuit voltage of 110 mV were obtained for a temperature difference of 75 °C. This translates to a maximum power density of 19 W/kg.

Figure 3.6.43 shows that the short circuit current density initially increased with thickness of the MWNT electrodes but then reached a plateau at about 140 µm. This drastically affects the results in terms of A/kg (Figure 3.6.44); which decreased with increasing thickness given that the mass of the electrode increased with thickness.
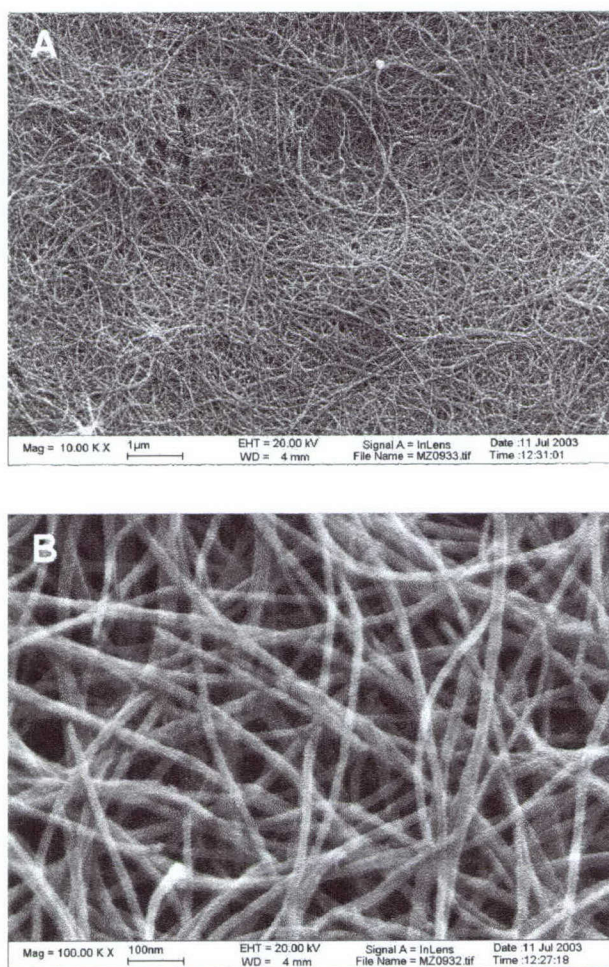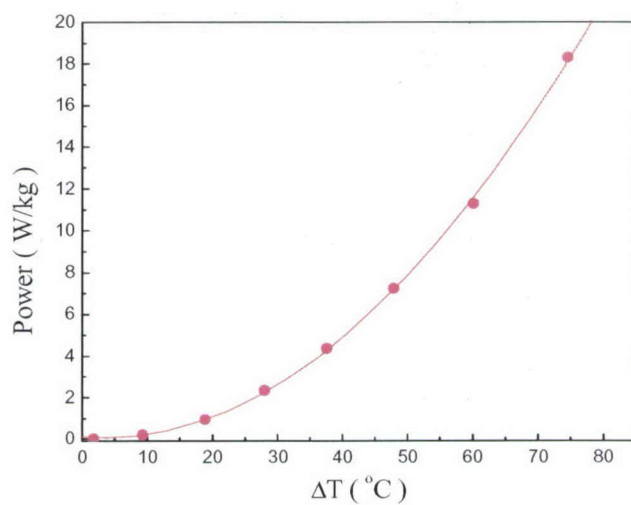

Figure 3.6.41. SEM images of CVD-grown MWNT bucky paper. (A) at 10K magnification and (B) at 100K magnification.
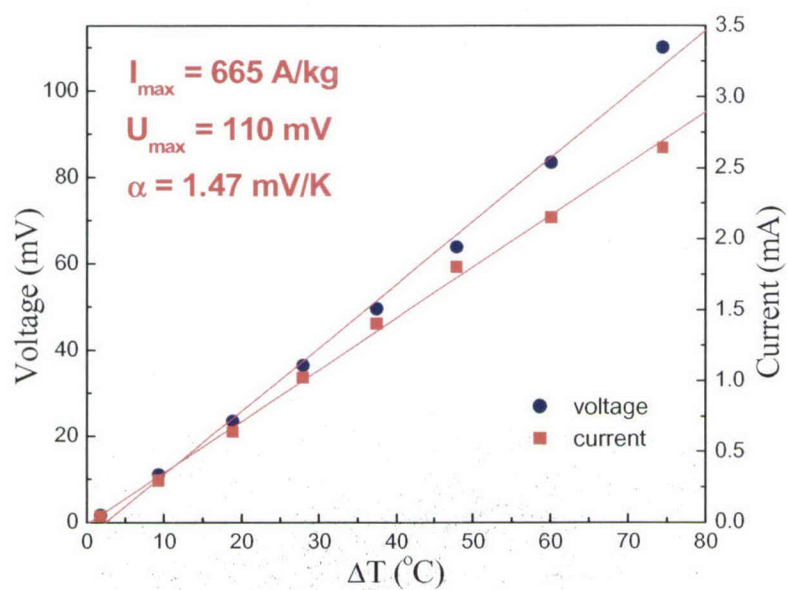
Figure 3.6.42. (a) Short circuit current normalized to electrode weight and open circuit voltage obtained at CVD-grown MWNT sheet electrodes (thickness 35 μm, treated with Triton X surfactant) in 0.4M ferri-/0.4M ferro-cyanide aqueous electrolyte; (b) Maximum power density versus temperature difference.
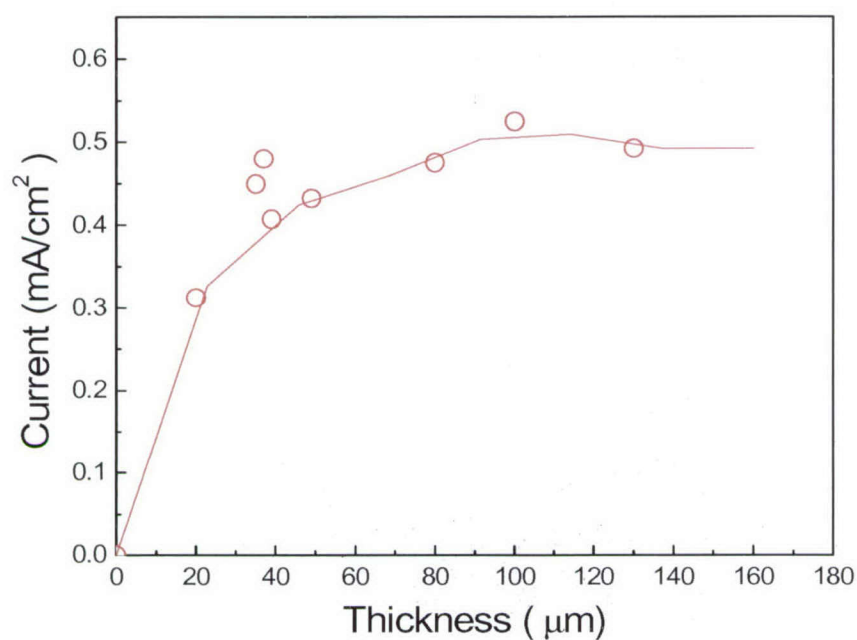
Figure 3.6.43. Effect of MWNT electrode thickness on Short Circuit Current Density (mA/cm^2) in terms of geometric area.
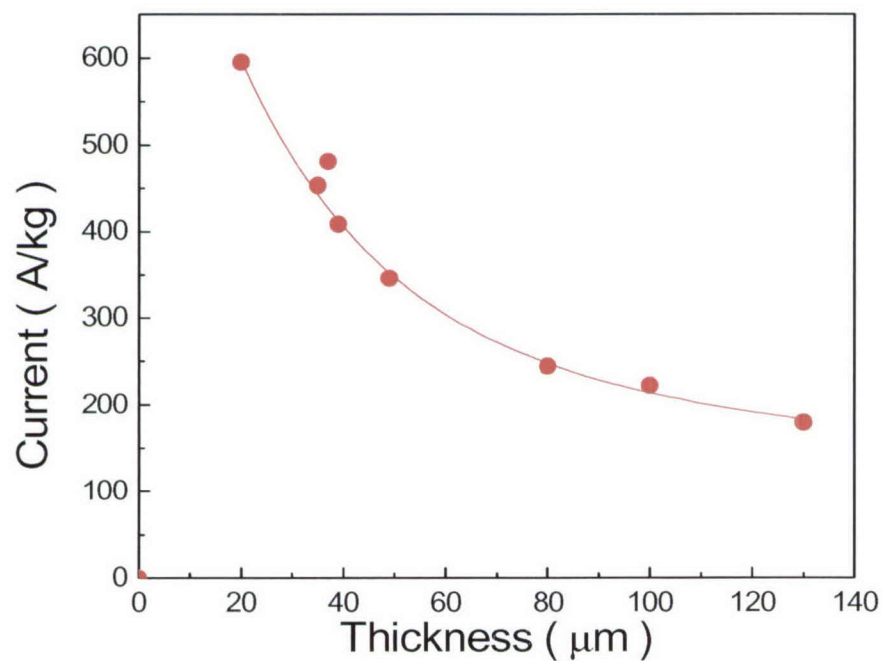

Figure 3.6.44. Effect of MWNT electrode thickness on Short Circuit Current Density (A/kg) in terms of mass.

Thermal Energy Harvesting Using Pre-treated HiPco SWNT

HiPco SWNT were used as electrodes in their untreated 'as received' condition or after ultrasonication in concentrated HCl for 1.5 hours or after heat treatment at 200 °C in air for 24 hours followed by ultrasonication in.HCl for 1.5 hours. The redox system used was 0.4 M ferri-/0.4 M ferro-cyanide in Milli-Q water, and the inter-electrode distance was 10 cm.

The treatments did not alter the Open Circuit Voltages obtainable (95 mV for ΔT of 70 °C). The treatments, however, did affect the Short Circuit Current Densities. When the HiPco SWNT was heated at 200 °C in air for 24 hours and then ultrasonicated in concentrated HCl for 1.5 hours, the electrodes made from this material produced a Short Circuit Current Density of 10.5 A/m^2 (Figure 3.6.45) or 1000 A/kg (Figure 3.6.46) for a temperature difference of 64 °C. These results translate to a Maximum Power Density of 228 mW/m^2 or 21.8 W/kg (Figure 3.6.47). This improvement in performance is probably due to the removal of residual metal catalysts, such as iron, that contribute to the weight of the electrodes but not to their thermoelectrochemical performance.
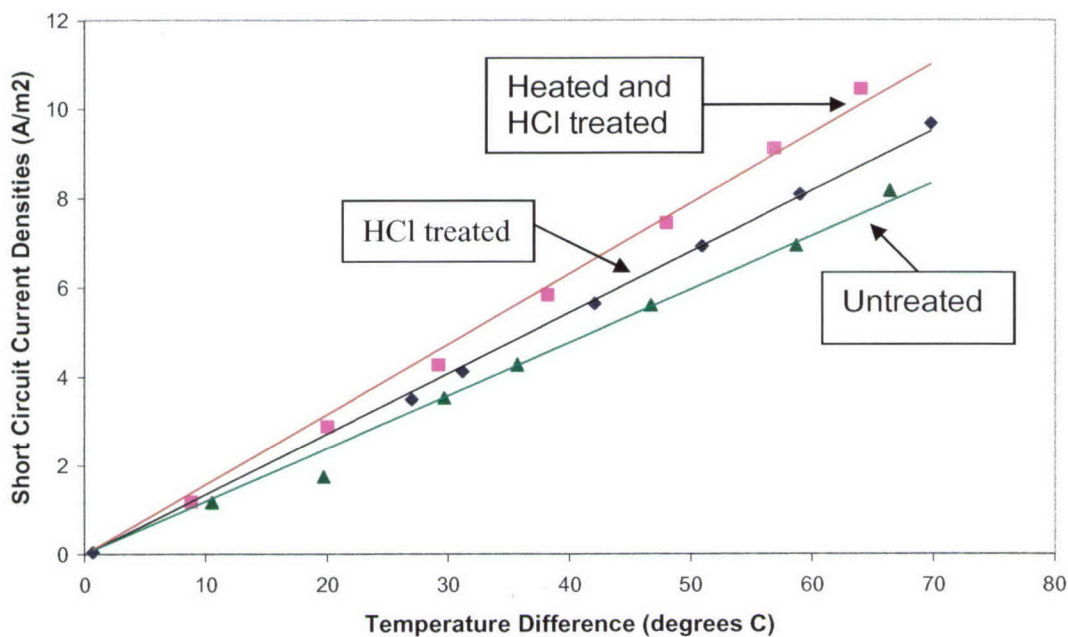

Figure 3.6.45. Comparison of Short Circuit Current Densities (A/m^2, geometric area) for HCl Treated, Heated and HCl Treated, and Untreated HiPco SWNT Electrodes.
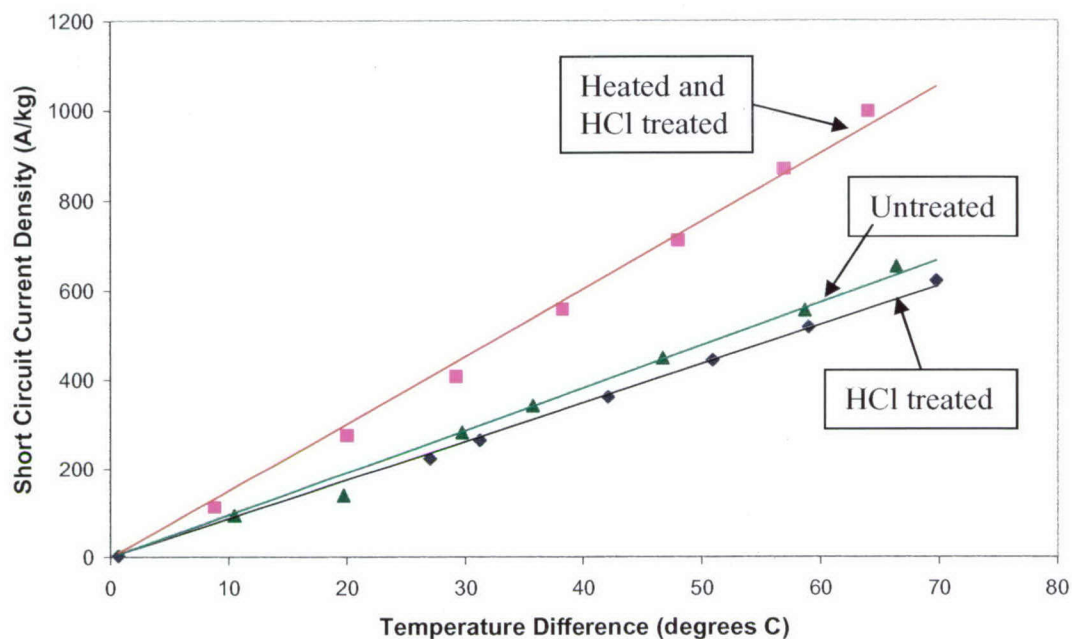
Figure 3.6.46. Comparison of Short Circuit Current Densities (A/kg) for HCl Treated, Heated and HCl Treated, and Untreated HiPco SWNT Electrodes.
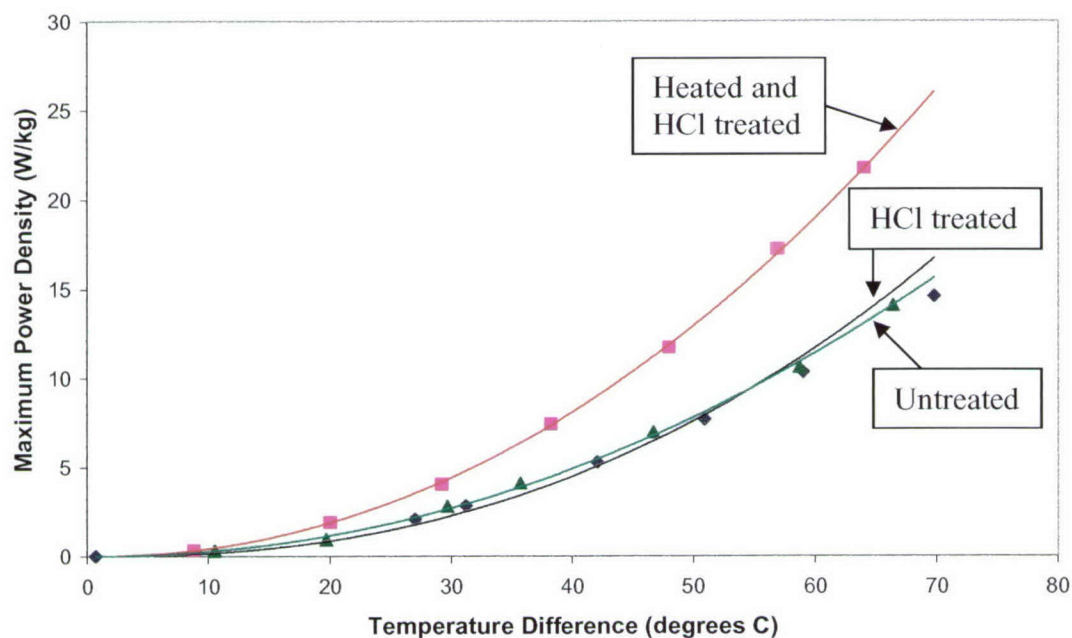

Figure 3.6.47. Comparison of Maximum Power Densities (W/kg) for HCl Treated, Heated and HCl Treated, and Untreated HiPco SWNT Electrodes.

Effect of Different Molar Ratios of ferrocyanide to ferricyanide

Table 3.6.7 summarizes the results obtained from these studies. It is clear from these results that higher ratios of ferrocyanide to ferricyanide produced higher performance; for example on comparison of the results for the molar ratios 0.1/0.4 and 0.4/0.1 (last two rows of Table 3.6.7). This suggests that the main driver of the cell is the hot side where ferrocyanide is oxidized to ferricyanide. However, the 0.4/0.4 ratio still gives the best results but this could be due to the higher total salt content, i.e. 0.8M. It was noted in earlier work that, for this redox system, 0.8M total salt concentration is at the limit of solubility.

Table 3.6.7. Thermoelectrochemistry results obtained at SWNT electrodes in various mixtures of ferrocyanide/ferricyanide for $\Delta T = 59\text{-}64\,^{\circ}C$.

Molar Ratio of Ferro-/Ferri-cyanide	Open Circuit Voltage (mV)	Short Circuit Current Density (A/m^2)	Short Circuit Current Density (A/kg)	Maximum Power Density (W/kg)
0.4/0.4	87	10.5	1000	21.8
0.3/0.4	85	8.6	821	17.4
0.4/0.3	86	9.0	860	18.6
0.2/0.4	85	7.9	751	15.9
0.4/0.2	93	8.4	804	18.6
0.1/0.4	84	6.7	643	13.4
0.4/0.1	97	7.6	727	17.7

Note. Inter-electrode distance = 10 cm.

Effect of Varying the Ratio of the Hot Anode : Cold Cathode Areas

Table 3.6.8 shows that varying the ratio of hot anode: cold cathode area did not significantly affect the thermoelectrochemical results even though the ratio of the areas was varied from 0.28 to 4.5.

Table 3.6.8. Thermoelectrochemical performance when using different ratios of the area of anode : Cathode in 0.4M ferri-/0.4M ferro-cyanide at a temperature difference of 53.5 – 55.6 $^\circ$C.

Anode area (cm^2)	Cathode area (cm^2)	Ratio of anode : cathode area	Open Circuit Voltage (mV)	Short Circuit Current (mA)
0.3	1.08	0.28	75.3	0.94
0.6	1.08	0.56	78.9	0.99
1.08	0.6	1.8	78.1	0.95
1.08	0.24	4.5	78.1	0.95

Effect of Using Carbon Foil Contacts of Pt

Pre-treated HiPco SWNT electrodes were mounted with carbon foil contacts instead of Pt. The results show that similar performance was obtained when compared with Pt contacts; Open Circuit Voltages were 90 mV for ΔT of 65 $^\circ$C. Figure 3.6.48 and Figure 3.6.49 show the Short Circuit Current Density in terms of geometric area and in terms of weight respectively. The Maximum Power Density is shown in Figure 3.6.50.
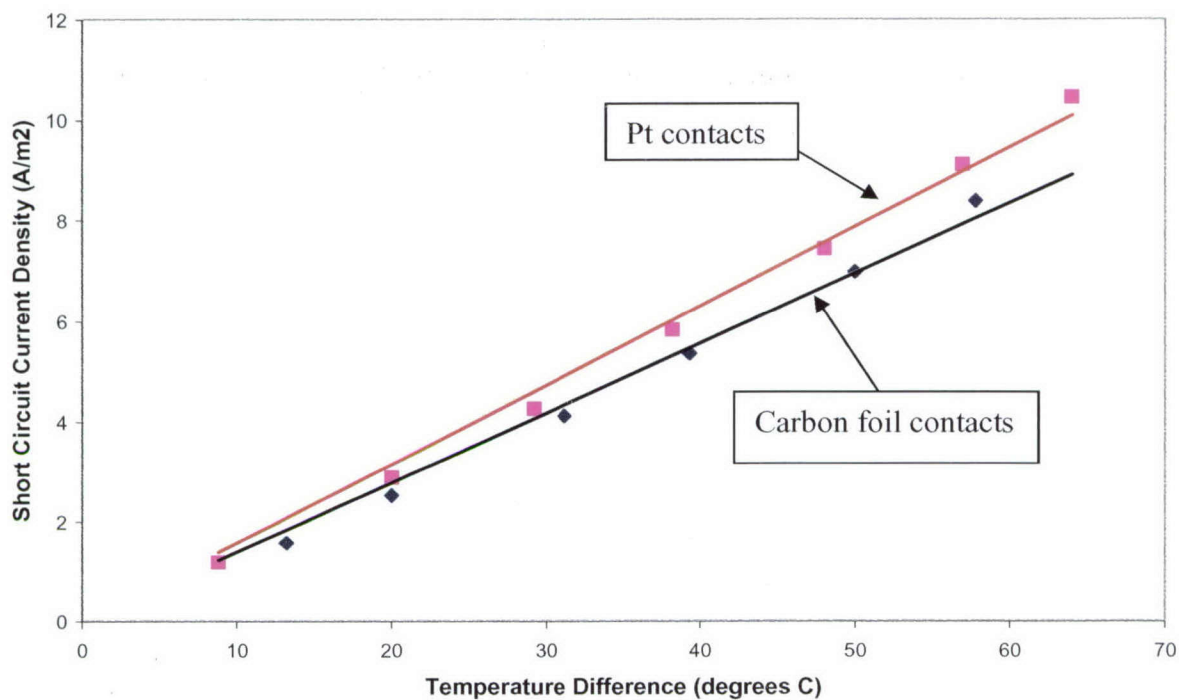
Figure 3.6.48. Comparison of Short Circuit Current Densities (A/m^2) obtained from pre-treated HiPco SWNT electrodes using carbon foil contacts or Pt contacts.
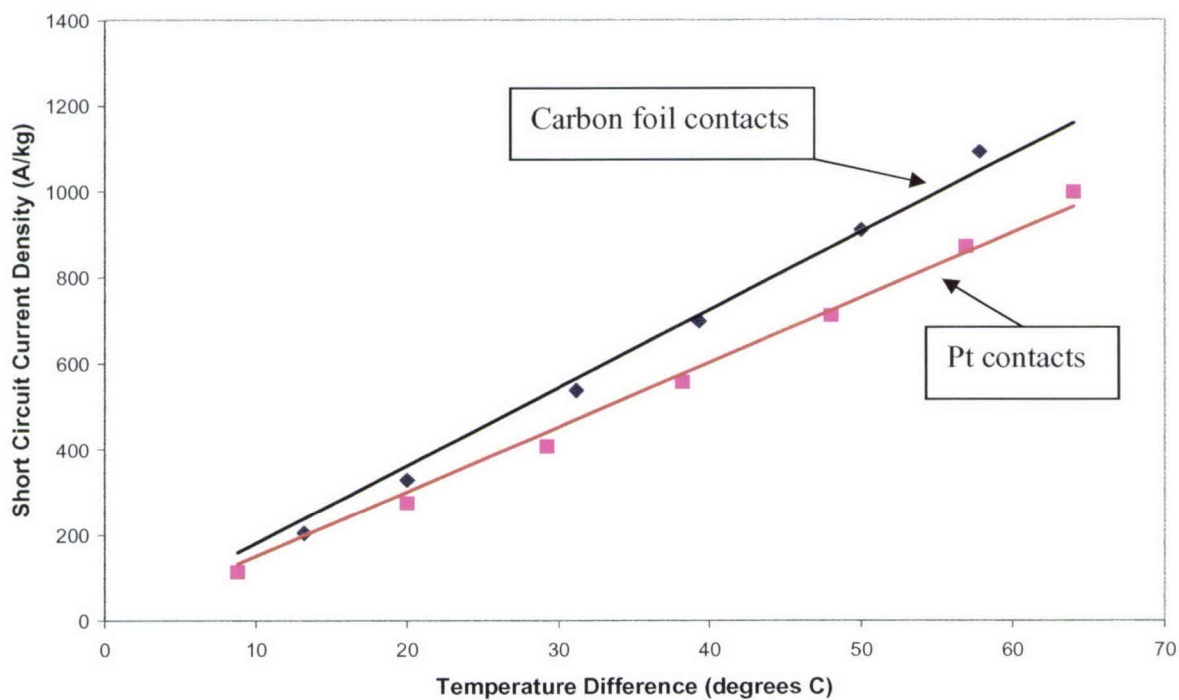

Figure 3.6.49. Comparison of Short Circuit Current Densities (A/kg) obtained from pre-treated HiPco SWNT electrodes using carbon foil contacts or Pt contacts.
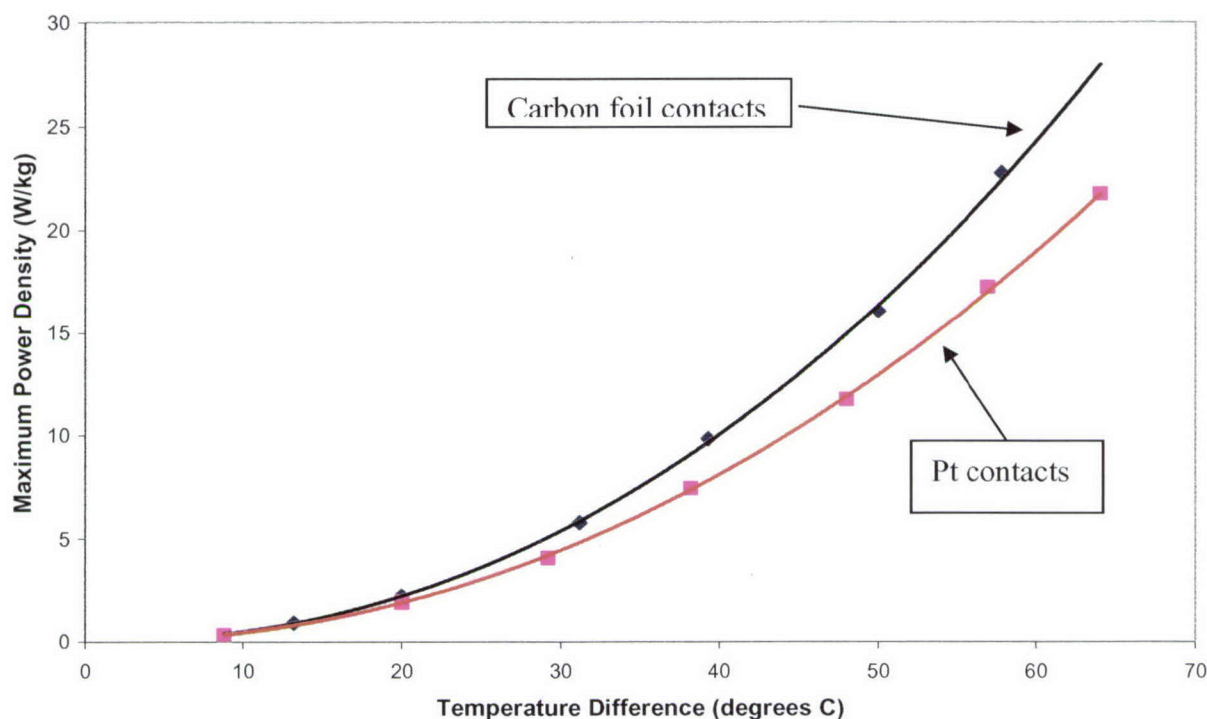
131

Figure 3.6.50. Comparison of Maximum Power Densities obtained from pre-treated HiPco SWNT electrodes using carbon foil contacts or Pt contacts.

Pre-treated HiPco SWNT in the 0.4M FeCl₂/0.4M FeCl₃/H₂O System

Pre-treated HiPco SWNT in the 0.4M FeCl$_2$/0.4M FeCl$_3$/H$_2$O System

The 0.4M FeCl$_2$/0.4M FeCl$_3$/1M HCl system was revisited to test the thermal energy harvesting performance of pre-treated SWNT. The results show that this system produced lower Open Circuit Voltages (Fig. 3.6.51) compared with the 0.4M ferro-/0.4M ferri-cyanide system. The other parameters were also lower: Short Circuit Current Densities (Figs. 3.6.52 and 3.6.53), and Maximum Power Densities (Fig. 3.6.54).
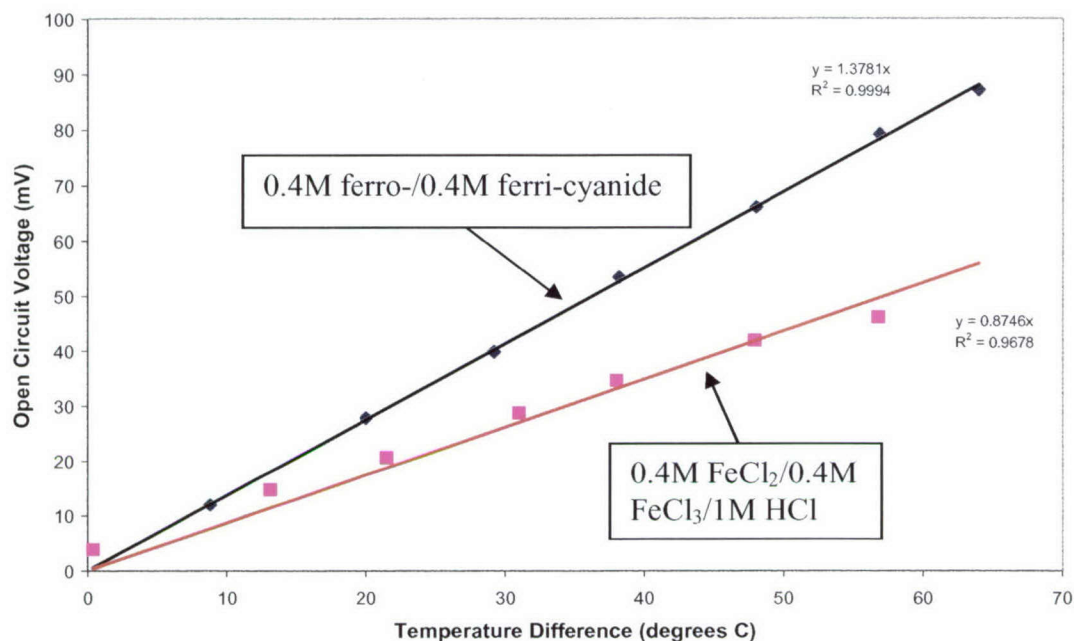
Figure 3.6.51. Comparison of Open Circuit Voltages for HiPco SWNT electrodes. The raw SWNT were heated at 200 °C for 24 hours and then ultrasonicated in concentrated HCl for 1.5 hours.
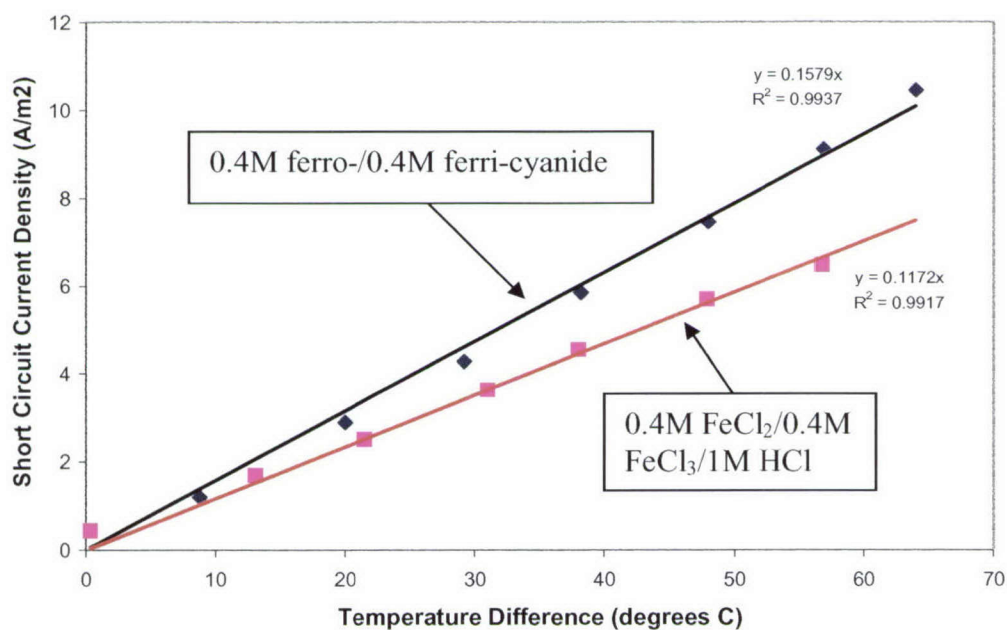

Figure 3.6.52. Comparison of Short Circuit Current Densities (A/m^2) for HiPco SWNT electrodes. The raw SWNT were heated at 200 °C for 24 hours and then ultrasonicated in concentrated HCl for 1.5 hours.
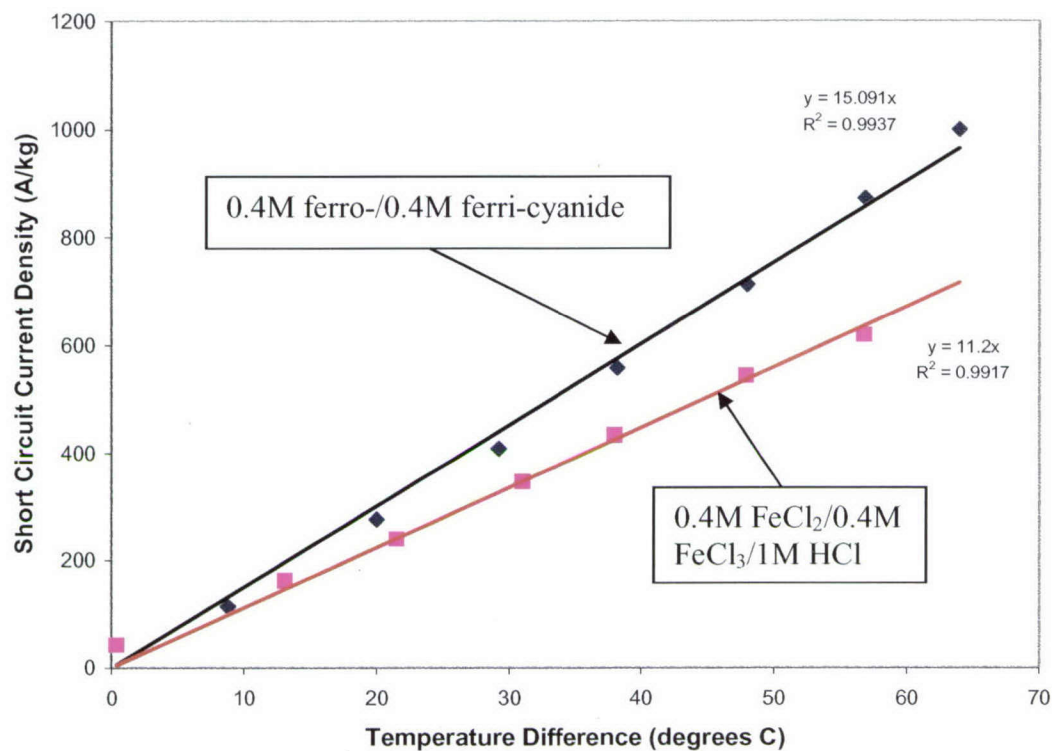
Figure 3.6.53. Comparison of Short Circuit Current Densities (A/kg) for HiPco SWNT electrodes. The raw SWNT were heated at 200 °C for 24 hours and then ultrasonicated in concentrated HCl for 1.5 hours.
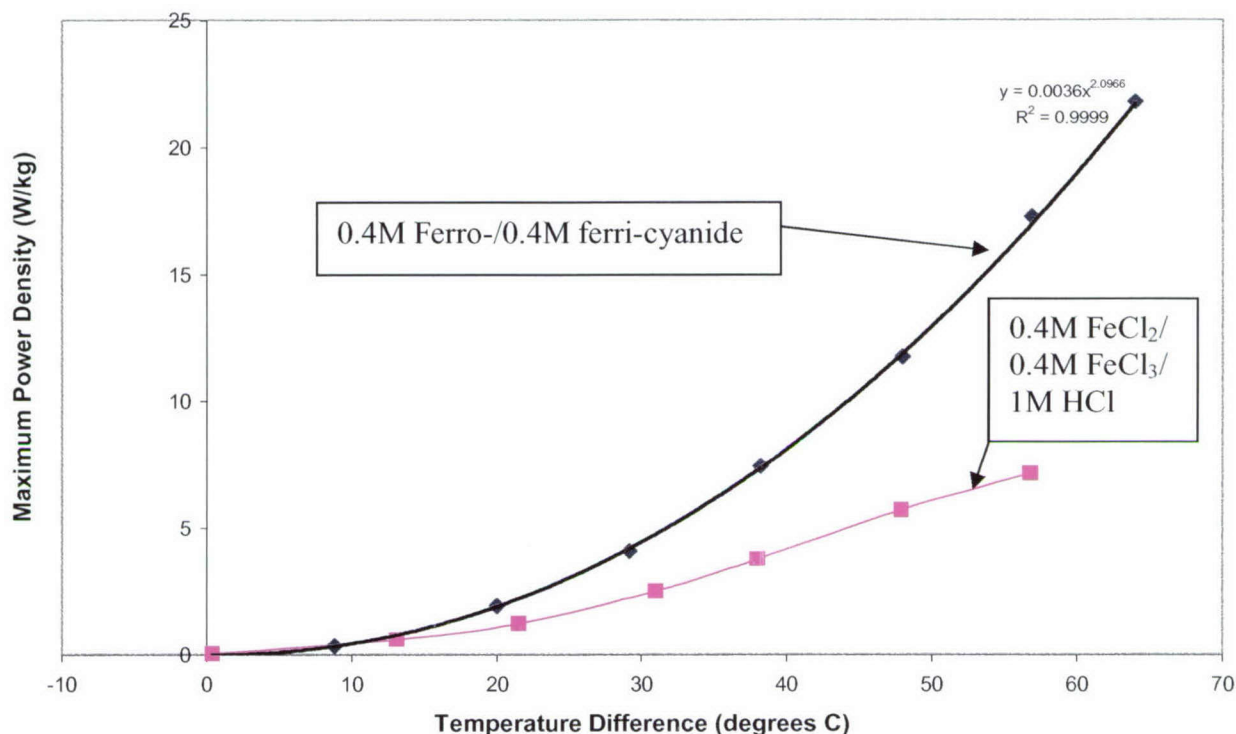
134

Figure 3.6.54. Comparison of Maximum Power Densities (W/kg) for HiPco SWNT electrodes. The raw SWNT were heated at 200 ^{o}C for 24 hours and then ultrasonicated in concentrated HCl for 1.5 hours.

Thermal Energy Harvesting Using Pre-treated MWNT as Electrodes

MWNT powder in concentrated HCl was ultrasonicated for 1.5 hrs. The slurry was carefully rinsed with deionized water until the pH was 6. Then the buckypaper was prepared by the usual method. We did not perform thermal oxidation of the MWNT powder before the acid treatment because MWNT does not contain a significant amount of Fe catalyst particles. The concentration of Fe is <<1%.

The thermoelectrochemical characteristics were measured in a U-type glass cell with an aqueous solution of 0.4M ferro-/0.4M ferri-cyanide. Figure 3.6.55 shows the temperature dependence of short circuit current and open circuit voltage obtained at CVD-grown MWNT sheet electrodes. The maximum short circuit current normalized to the weight of electrode reached 1446 A/kg and power was 28 W/kg. These are the highest results obtained to date. Our previous best results were 1092 A/kg and 22.8 W/kg obtained from

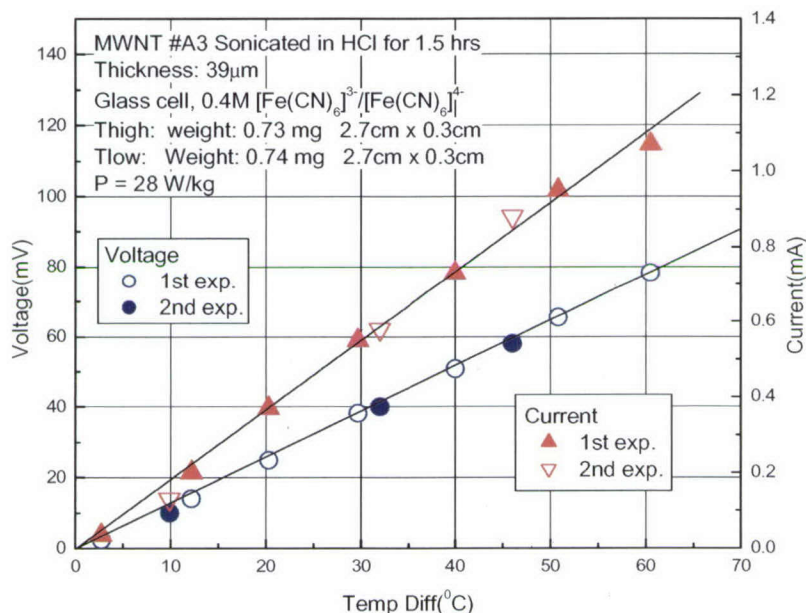HiPco SWNT that was heat treated in air at 200 °C for 24 hours followed by concentrated HCl treatment.

Figure 3.6.55. Temperature dependence of open circuit voltage and short circuit current obtained at CVD-grown MWNT sheet electrodes (thickness 39 μm, treated with HCl) in 0.4M ferri-/0.4M ferro-cyanide aqueous electrolyte.

The time dependence of current and voltage obtained with these electrodes was also considered (Figure 3.6.56). The thermocell showed slow degradation at a hot electrode temperature of T = 70 °C which is close to the decomposition temperature of ferrocyanide. However, when the temperature of the hot electrode was decreased to 60 °C, the current was slightly restored and was stable without any sign of further degradation. Similar effects were also found for the voltage.
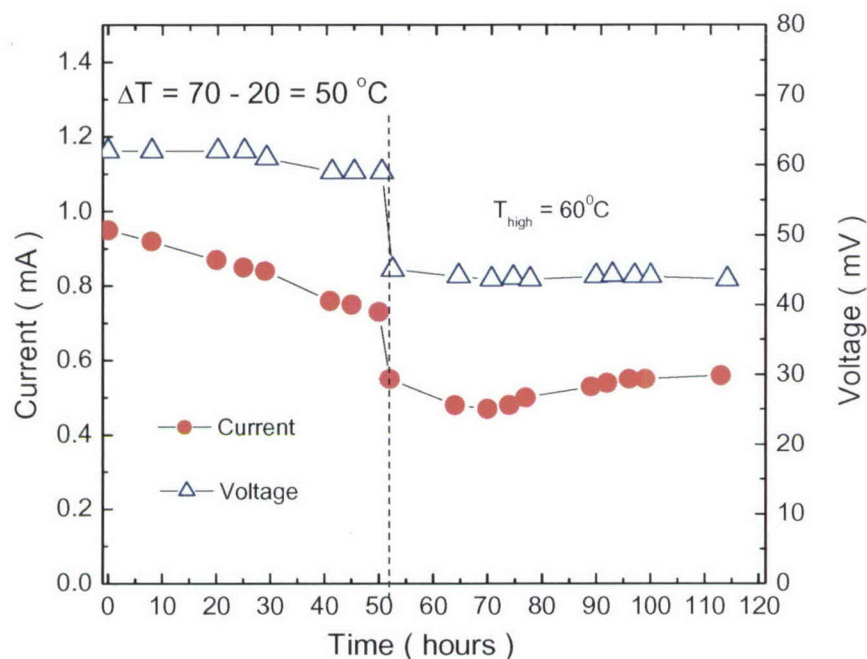
Figure 3.6.56. Dependence of short circuit current and open circuit voltage on time: showing the effect of lowering the hot side temperature from 70 °C to 60 °C.

A second set of experiments was done with MWNT powder sonicated in HSO_4/HNO_3 (3:1) in an ultrasonic bath for 1.5 hrs. The slurry was carefully rinsed with deionised water until the pH attained a value of 6. Then buckypaper was prepared by the usual method. Figure 3.6.57 shows the temperature dependence of short circuit current and open circuit voltage. The maximum short circuit current normalized to the weight of electrode reached 1120 A/kg and power was 15 W/kg.

There are possibly two main reasons for the thermoelectrochemical improvement observed when using carbon nanotubes treated with acids. First, it is known that treatment in a mixture of 3:1 concentrated sulfuric and nitric acid increases surface area and pore sizes. K. Niesz et al. (Catalysis Today 76 (2002) 3-10) have measured an increase in surface area from 193 m^2/g to 263 m^2/g and an increase in pore size of MWNTs after acid treatment. The second reason is well known from electrochemical studies of graphite electrodes; the edges of the graphite plane are electrochemically more active than the basal planes.
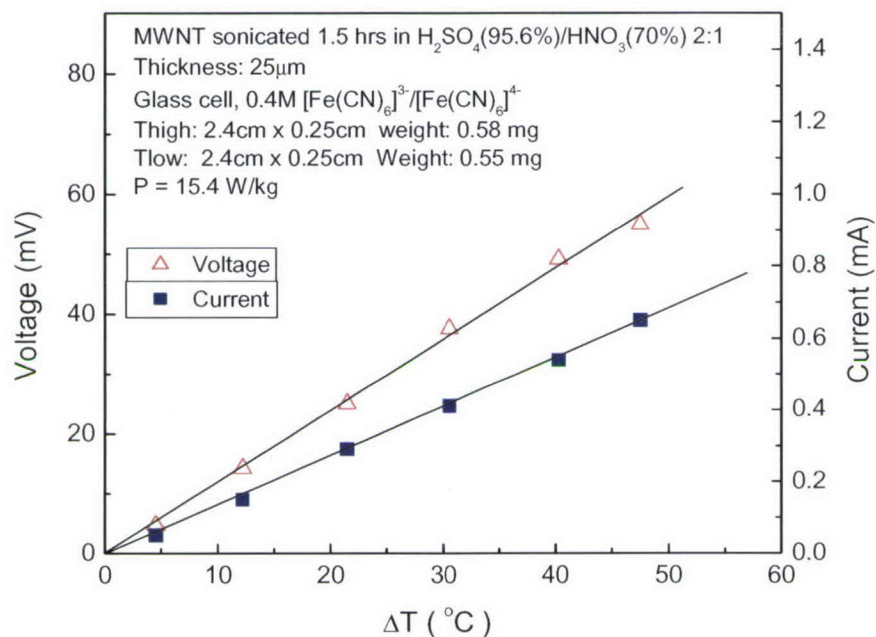
137

Figure 3.6.57. Dependence of Open Circuit Voltage and Short Circuit Current on Temperature Difference. Electrodes were made from H_2SO_4/HNO_3 treated MWNT. Electrolyte: 0.4M ferro-/0.4M ferri-cyanide in demonized water.

Final Comparison of Thermal Energy Harvesting Obtained Using Different Electrode Materials

Comparison of other substrates for thermal energy harvesting in aqueous 0.4M ferro-/0.4M ferri-cyanide was revisited. The results are summarized below in Table 3.6.9. As is evident from the results, SWNT performance is slightly lower than carbon foil (flexible graphite) or Pt when normalized to per unit area. However, SWNT performance far exceeds that of other electrode materials when normalized to per unit weight.

Table 3.6.9. Comparison of Thermoelectrochemical Performance Obtained from Different Electrode Materials

Performance Parameters	SWNT	C Foil	Pt (80 mesh)	Pt Plate
V_{oc} (mV)	83.4	82.4	76.2	82.7
I_{sc} (A/m^2)	8.4	10.8	10.7	14.5
I_{sc} (A/kg)	1092	217	32.5	-
Maximum Power (mW/m^2)	174.9	223.4	204.2	259.1
Maximum Power (W/kg)	22.8	4.5	0.62	-

Temperature difference = 53 to 58 $^{\circ}$C. Inter-electrode distance = 10 cm. Thickness of C foil = 0.1 mm.

High Temperature Thermal Energy Harvesting Using Nonaqueous Electrolyte Systems

For the operation of thermal energy harvesting at temperatures above 100 $^{\circ}$C, the use of nonaqueous electrolyte systems were considered.

Thermal EnergyHarvesting in iodine/iodide Electrolyte

In previous preliminary studies, the iodine/iodide electrolyte based on ethylene carbonate/propylene carbonate solvent was tested for thermal energy harvesting, but the achieved currents were very low. For the current study we have chosen **Iodolyte TG 500** electrolyte (SOLARONIX SA). Iodolyte TG-500 is based on polyethylene oxide solvents and contains 0.5 M iodine and 0.5 M iodide. This electrolyte does not evaporate, even at elevated temperatures (> 180 $^{\circ}$C).

$$I_3^- + 2e \Leftrightarrow 3I^-$$

The results are presented in Fig. 3.6.58 for an inter-electrode distance of 10 cm. We have achieved an open circuit voltage of 260 mV at $\Delta T=150$ $^{\circ}$C, but the short-circuit current was very low (0.075 mA/cm^2). As we understand from this study, the performance of thermocell with Iodolyte TG-500 was limited by high electrolyte resistance, as the diffusion of the ions is impeded by the fairly viscous polyethylene oxide, and by high

interface resistance. The performance of Pt+SWNT and Pt+MWNT in this electrolyte was similar.
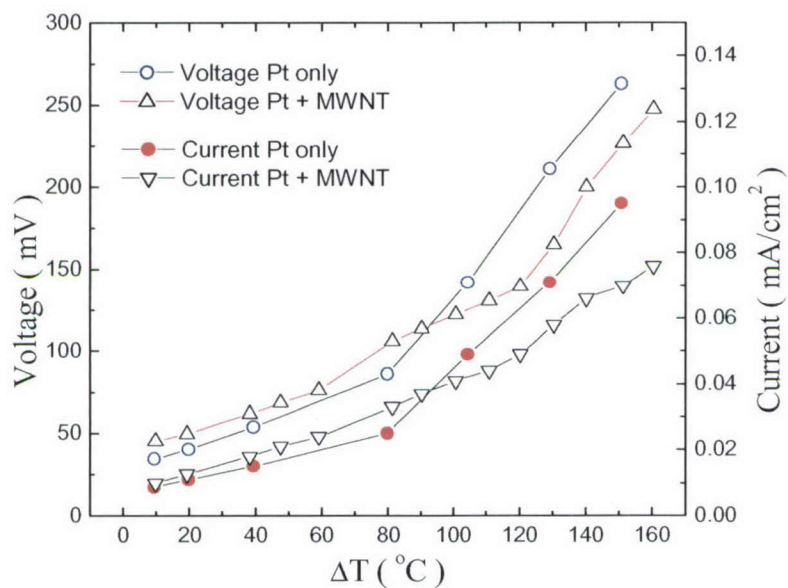

(a)
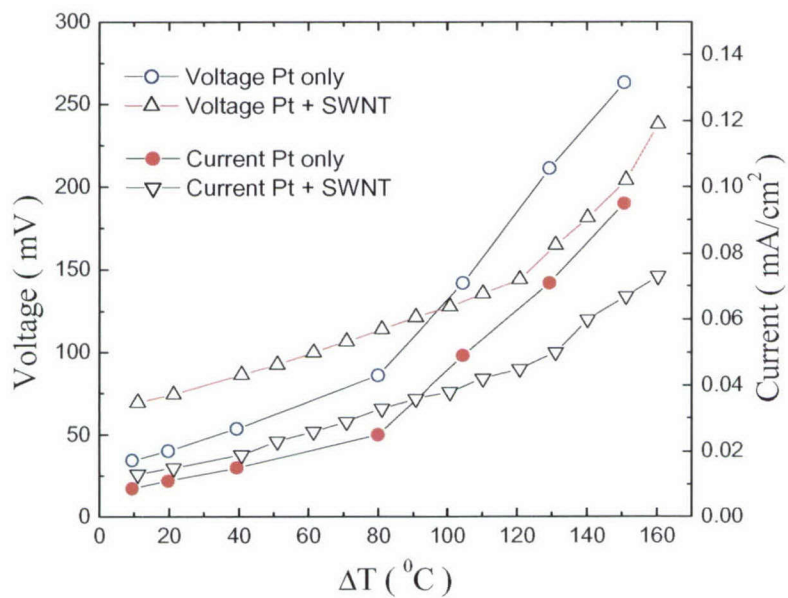
(b)

Figure 3.6.58. (a) Short circuit current and open circuit voltage obtained at SWNT electrodes in Iodolyte TG-500 electrolyte; (b) Short circuit current and open circuit voltage obtained at CVD-grown MWNT electrodes in the same electrolyte.

Ionic Liquids

Attention was focused on the use of ionic liquids for thermal energy harvesting. It was noted previously that the poor performance of HiPco SWNT in a 1:1 mixture of 1-Butyl-3-methylimidazolium $FeCl_3$: 1-Butyl-3-methylimidazolium $FeCl_4$ (**I**) might be due to the high viscosity of this ionic liquid mixture (Electrolyte 1). Therefore, to decrease the viscosity of Electrolyte 1, both sides of the thermocell were heated but one side was heated to a higher temperature than the other.

$[FeCl_4]^-$ or $[FeCl_3]^-$
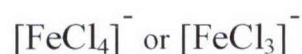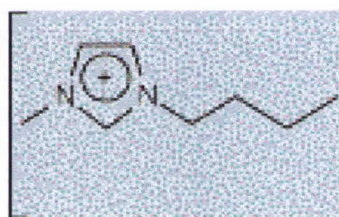
(I)

Table 3.6.10 shows that when both anode and cathode compartments were heated (198.8 ^{o}C and 80.3 ^{o}C respectively), the performance was better even though the temperature difference was lower between the anode and cathode (118.5 ^{o}C compared with 153.4 ^{o}C). These results lend credence to the conclusion previously drawn that it is the viscosity of the ionic liquid that is limiting the thermoelectrochemical performance.

Table 3.6.10. Comparison of thermoelectrochemical performance.

Electrolyte System	Anode Temperature (^{o}C)	Cathode Temperature (^{o}C)	Temperature Difference (^{o}C)	Open Circuit Voltage (mV	Short Circuit Current Density (A/kg)
1	175.6	22.2	153.4	30.1	3.1
1	198.8	80.3	118.5	27.9	8.9
2	150.0	47.1	102.9	34.5	33.8
3	150.0	23.9	126.1	11.5	3.5
3	201.2	80.5	120.7	10.0	7.5

Another method for improving the fluidity of Electrolyte 1 by mixing it with other less viscous ionic liquids was also successful. It was found that Electrolyte 1 was miscible with BMI.BF$_4$, or BMI.TFSA. Therefore the following electrolyte mixtures were prepared: -

Electrolyte 2: 1M of Electrolyte 1 in BMI.BF$_4$.

Electrolyte 3: 1M of Electrolyte 1 in BMI.TFSA.

It was found that the thermoelectrochemical performance in Electrolyte 2 was greatly improved but the performance in Electrolyte 3 was similar to that in Electrolyte 1 (Table 3.6.10).

Investigations of the cyclic voltammetry of Electrolyte 1 at a platinum electrode vs a silver wire pseudo-reference electrode were performed over a temperature range from 24 ^{o}C to 160 ^{o}C. The cyclic voltammogram obtained at 24 ^{o}C is given in Figure 3.6.59.
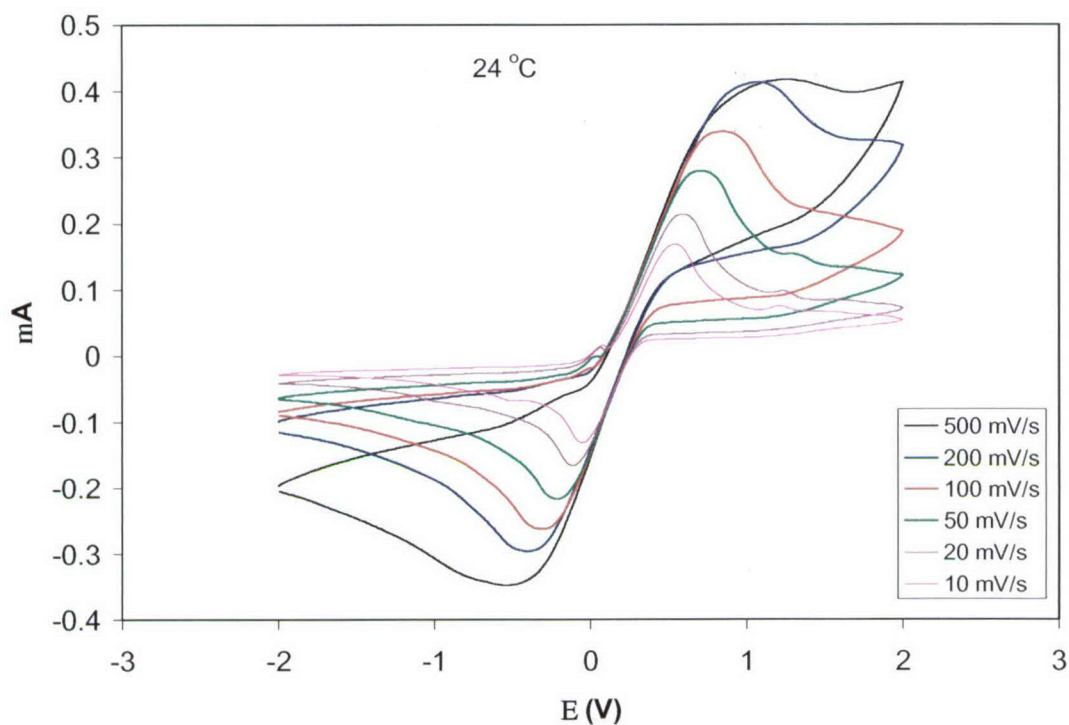
Figure 3.6.59. Cyclic voltammograms obtained at different scan rates for BMI.FeCl$_4$/BMI.FeCl$_3$ (1:1 mixture) at 24 °C.

The difference between the anodic and cathodic peak potentials decreases with increasing temperature because the anodic peak shifts cathodically and the cathodic peak shifts anodically with increasing temperature. This indicates that the electron transfer becomes faster as the temperature is increased. In addition, the peak currents increase with temperature and the ratio of anodic to cathodic peak currents decreases with increasing temperature.

PROGRESS AGAINST GOALS (*See monthly and annual reports for full details.*)

3.1 Modeling and Design Rules

Ab initio methods and tight binding methods were used to predict the optimal choice of single-wall nanotube type for actuation. The origin of the originally observed discrepancies between *ab initio* and analytical calculations of nanotube coulombic expansion coefficients have been determined and eliminated. While an enormous amount of useful experimental data was obtained that enables the choice of solid-state and liquid electrolytes that optimize performance for multifunctional electrochemical applications, theoretical understanding of these results is incomplete.

3.2 Materials Development and Characterization

3.2.1 Carbon Nanotube Purification and Modification

While we have successfully developed methods for dramatically improving the purity of spun nanotubes, these methods are both time consuming and are not noticeably advantageous for improving the properties of coagulation spun nanotubes. Our best results for polymer-coagulation-based spinning of carbon nanotubes are for purified HiPco nanotubes. The initially planned effort on filling carbon nanotubes with metals and semiconductors was changed to the successful effort to enable the spinning of single wall/multiwall nanotube mixtures and double walled nanotubes.

3.2.2 Electrolytes for Nanotube Composites

The performance of the highly-redox-stable molten salt electrolytes (ionic liquids) and the ionic-liquid-based solid state electrolytes for actuator and supercapacitor applications has been thoroughly characterized with respect to redox stability range, charging rate, and cycle life. Advantages were found in cycle lifetimes, compared with those for ordinary organic electrolytes. Charging times as short as 3 ms were obtained. Efforts to demonstrate cantilever-based nanotube actuation at above 350 °C were frustrated by the high viscosity, high density, and corrosive nature of the investigated molten salts at the investigated 800 °C. Ongoing work will solve these problems, in part by going from cantilever actuators to tensile actuators.

144

3.3 Carbon Nanotube Spinning, Debundling, and Welding

The nanotube spinning effort has been exceptionally successful. As a result of program funding, we can make two hundred-meter long reels of continuous nanotube-polymer composite fiber at 70X the prior-art rate and achieve fiber strengths higher than 1.8 GPa. Our drawn nanotube fibers match the energy absorption capability of the highest performance spider silk up to the breaking strain of this silk (30%), and continue absorbing energy until they reach an energy-to-break of 570 J/g, as compared with 160 J/g for the spider silk, 50 J/g for Spectra fiber, 33 J/g for Kevlar fiber, and 1.5 J/g for prior-art solution-spun nanotube fibers. The density-normalized tensile strength of our nanotube composite fiber is presently 2.2X that of high performance steel wire and the density-normalized Young's modulus of the nanotube fiber and steel wire are identical. The achieved modulus is 80 GPa, versus the program end milestone of 100 GPa for unwelded nanotube fibers. Using our program-developed polymer-free coagulation spinning method, we have obtained fiber capacitances of up to 100 F/g, which equals the target value. Using a polyvinyl alcohol as a matrix, we have achieved nanotube fibers having strengths of over 1.8 GPa, which is much higher than the program end milestone of 500 MPa for welded fibers. While welding using the silazane based precursor Polyureamethylvinylsilazane (CerasetTM-SN) has essentially eliminated creep-like deformations up to high temperatures and the temperature dependent modulus, we had difficulty applying this welding method to polymer-coagulant spun fibers that have been been pyrolized (due to the brittleness of these fibers). Moreover, incorporation of Ceraset in these fibers seems to increase brittleness, which means that the pyrolized Ceraset is increasing the ratio of fiber modulus to fiber strength. We have extended the coagulation spinning method to both new coagulation polymers (most noteably polyethylenimine) and to polymer-free coagulation solutions. In the latter program technology (patent pending) aqueous nanotube dispersions are coagulated by spinning into either an acid or a base. Using both of these new spinning technologies (for the polyethylenimine coagulant and the polymer-free coagulants) we have been able to spin hollow nanotube fibers.

3.4 Actuating Multifunctional Structures

Our efforts to improve actuation for coagulation-spun fibers and to use this improved actuation for multifunctional structures has not been very successful. The main problem is that our polyvinyl alcohol spun fibers must be pyrolized prior to use for actuation (to remove the polyvinyl alcohol), and this pyrolysis results in fibers that are very brittle. This brittleness interferes with both post-pyrolysis processing and characterization of actuation. As a result, we have not been able to significantly exceed our previous record isometric stress generation capability of 27 MPa (100X natural muscle). However, using resistance compensation and voltage pulse shaping we have demonstrated an actuator strain rate of 20%/s, which exceeds our program end milestone of 5%/s. In other research, we have succeeded in developing a twist-based route to high performance nanotube fibers that are polymer free. These twist-spun fibers are most promising for nanotube actuator development.

3.5 Energy Storing Multifunctional Structures

Using a variety of different types of spun nanotube fibers, we have made 100 micron or smaller diameter nanotube fiber capacitors and have extensively characterized their performance for multifunctional applications. Our packaged solid-state fiber supercapacitor devices display specific capacitance values ranging from 6 F/g to 12 F/g and energy and power densities reaching 1.34 Wh/kg and 1.0 kW/kg, respectively. Though, the discharge rate needs improvement, the energy density of our 100 micron diameter supercapacitors based on water-containing electrolytes is within a factor of 2-3 of that for large aqueous electrolyte commercial supercapacitors. In order to illustrate a multifunctional application (energy storing textile), we have woven our nanotube fiber supercapacitors into a conventional textile.

3.6 Other Functions for the Multifunctional Structures of Sections 3.4 and 3.5

Using Pt-containing nanotube sheets, we have demonstrated thermoelectrochemical energy harvesting cells providing a Short Circuit Current Density of 3800 A/kg and a Maximum Power Density of 83 W/kg for a temperature difference of 65 °C. This result, based on nanotube electrode content, far exceeds the program end milestone of 700 A/kg.

Results exceeding this milestone were also obtained for Pt-free multi-walled carbon electrodes, where the maximum short circuit current (normalized to the weight of electrode) reached 1446 A/kg and power was 28 W/kg. These results are for the ferri-ferro cyanide redox couple, which we now know does not have long term stability at high electrode temperatures. We have found redox mediators and associated electrolyte systems that have much higher stability than the ferri-ferro cyanide system, but none provide comparable power densities. In other work in this *Other Function* area, we have demonstrated that single walled carbon nanotubes can be switched in infrared reflectivity in the atmosphere-transparent infrared range by double-layer charge injection. Considering that the nanotubes are largely silent in the infrared, this aspect might be of interest for future investment for camouflage applications.